R84-10

FINAL CALIBRATION OF THE COOLING LAKE MODEL FOR NORTH ANNA POWER STATION

by
EDMOND K. HO
and
E. ERIC ADAMS

RALPH M. PARSONS LABORATORY
AQUATIC SCIENCE AND ENVIRONMENTAL ENGINEERING

Report No. 295

Prepared under the Support of
Virginia Electric and Power Company
Richmond, Virginia

AUGUST 1984

MIT

DEPARTMENT
OF
CIVIL
ENGINEERING

SCHOOL OF ENGINEERING
MASSACHUSETTS INSTITUTE OF TECHNOLOGY
Cambridge, Massachusetts 02139

R84-10

FINAL CALIBRATION OF THE COOLING LAKE MODEL FOR NORTH ANNA POWER STATION

by

Edmond K. Ho

and

E. Eric Adams

RALPH M. PARSONS LABORATORY

AQUATIC SCIENCE AND ENVIRONMENTAL ENGINEERING

DEPARTMENT OF CIVIL ENGINEERING

MASSACHUSETTS INSTITUTE OF TECHNOLOGY

Report No. 295

Prepared under the support of

Virginia Electric and Power Company

Richmond, Virginia

AUGUST 1984

ABSTRACT

The North Anna Power Station is a two-unit power plant located on Lake Anna and operated by Virginia Electric and Power Company (VEPCO). A complex cooling lake system, involving a diked-off portion of Lake Anna - known as the Waste Heat Treatment Facility (WHTF) - as well as the main lake, was designed to dissipate the waste heat rejected by the plant. In order to monitor the impacts that the waste heat discharge has on the natural environment and also to assess the efficiency of the cooling lake system, a segmented mathematical model was previously developed (Jirka et al., 1977).

Since Unit 1 of North Anna Power Station came on line in summer of 1978 (followed by Unit 2 in autumn of 1980), an extensive data collection network was established by VEPCO. The model was previously calibrated using data from the first three years of operational data (1978 to 1981, primarily one-unit operation). Since then more measurements were available and an independent validation was conducted by comparing model predictions with data for the following two years (1981 to 1983, with more two-unit operation) using the same model calibrations.

Surface temperature error analysis was made for four representative diagnostic control points over the cooling lake system. It was noticed that the model results for five years were similar to those for the first three years. However, temperature rise across the plant condenser was consistently over-predicted by an average of about 0.7°C over all five years. In addition, results of spectral analysis showed that the raw error at DIKE III was periodic at predominantly the annual frequency whereas the rest of the control points showed mild periodicities over a relatively wide range of frequencies.

Model recalibration aiming at improving the goodness-of-fit of the five years of measurement data at DISCHARGE and DIKE III was motivated by the results of the surface temperature error analysis. Two possible reasons for the transient errors characterized by annual periodicity of the raw error at DIKE III were identified, namely, errors associated with (1) the forcing function (surface heat transfer) and (2) system response of the model. Two candidates for each of the possible reasons were considered: (1a) atmospheric radiation, (1b) evaporation, (2a) spatially-averaged system response, and (2b) longitudinal system response. Regarding the steady state errors at DISCHARGE, a sensitivity analysis of the raw error with respect to changes in the plant operation data was made, and it was noticed that the mean raw error was reduced substantially by a moderate reduction of the waste heat discharged into the WHTF.

In all, two changes of the model were made as a result of recalibration: computation of residence times in the WHTF and adjustment of plant operation data. The recalibrated model was validated by comparing predictions with five years (1978-1983) of

measurement data in terms of both surface temperatures and vertical temperature profiles. Overall mean errors for the four diagnostic control points ranged (in terms of magnitude) from a minimum of 0.01 °C to a maximum of 0.16°C while standard deviations ranged from 0.80 °C to 1.37 °C. In comparision with the large peak-to-peak annual variation in water surface temperature of about 23 °C, the mean errors and standard deviations are both acceptably small. Comparisons between measured and predicted vertical temperature profiles in the main lake indicated that the dynamic nature of the data both in space and time was also modelled satisfactorily.

In addition to overall averages, monthly averages of the surface temperature raw errors were also computed for each of the diagnostic control points. These monthly error statistics can be applied by VEPCO to increase the accuracy of future model predictions.

ACKNOWLEDGEMENTS

This study was funded by Virginia Electric and Power Company, Richmond, Virginia (MIT OSP No. 93576). The report is the last in a series which describes the development, calibration and verification of the North Anna Cooling Lake Model. Earlier technical reports include

Watanabe, M., Harleman, D. and Connor, J., "Finite Element Model for Transient Two-Layer Cooling Pond Behavior", Technical Report No. 202, R.M. Parsons Laboratory, Department of Civil Engineering, MIT, 1975.

Brocard, D., Jirka, G. and Harleman, D., "A Model for the Convective Circulation in Side Arms of Cooling Lakes", Technical Report No. 223, R.M. Parsons Laboratory, Department of Civil Engineering, MIT, 1977.

Octavio, K., Jirka, G. and Harleman, D., "Vertical Heat Transport Mechanisms in Lakes and Reservoirs", Technical Report No. 227, R.M. Parsons Laboratory, Department of Civil Engineering, MIT, 1977.

Jirka, G., Brocard, D., Octavio, K., Watanabe, M. and Harleman, D., "Analysis of Cooling Effectiveness and Transient Long-Term Simulations of a Cooling Lake with Application to the North Anna Power Station", Technical Report No. 232, R.M. Parsons Laboratory, Department of Civil Engineering, MIT, 1977.

Wells, S., Adams, E. and Harleman, D., "Calibration and Verification of the Cooling Lake Model for North Anna Power Station during the Period July 1978 - September 1981", Technical Report No. 272, R.M. Parsons Laboratory, Department of Civil Engineering, MIT, 1982.

The authors wish to express their gratitude to VEPCO for their generous support and to Drs. Morris Brehmer and Jack Taylor, Messrs. John White, Judson White and Nat Wooding and Ms. Joyce Barton for their personal help and cooperation.

The authors also acknowledge the efforts of Drs. Masataka Watanabe, Dominique Brocard, Gerhard Jirka and Ms. Kathleen Octavio who were involved in the original model development; Drs. Peter Shanahan and Kevin Farley and Mr. Scott Wells who participated in early stages of model calibration; and Prof. Donald Harleman who provided helpful comments throughout both phases.

This report represents the Master's thesis of Mr. Edmond Ho submitted to the Department of Civil Engineering at Massachusetts Institute of Technology. Thesis supervision was provided by Dr. E. Eric Adams, Principal Research Engineer in the MIT Energy Laboratory and Lecturer in the Department of Civil Engineering.

The manuscript was typed by Mrs. Diane Westerink and some of the figures were drafted by Mrs. Izildinha Baptista. The authors express their sincere appreciation to both.

CONTENTS

1. INTRODUCTION

1.1 Electric Power Plant and Waste Heat Disposal Problem

The typical conversion efficiencies of present steam-electric power plants are about 38% for fossil fuel plants and 32% for nuclear plants, with internal plant losses of about 15% and 5%, respectively. The remaining bulk of energy is dissipated in the form of heat through a condenser cooling system, the ultimate heat sink of which is, not surprisingly, the atmosphere.

Since all steam power plants reject a significant amount of waste heat to the environment, the choice and design of a condenser cooling system is crucial in assessing the environmental impacts that an individual power plant has upon the neighboring area. An effective condenser cooling system is one which can transfer economically the waste heat from the condenser water to the atmosphere.

Three main categories of condenser cooling systems are commonly used in the electric power industry:

a. Once-through cooling

The cooling water is withdrawn from a large, nearby water body and the heat-loaded water from the condenser is discharged back into the water body. The waste heat is transferred from the water surface to the atmosphere by evaporation, conduction and back radiation. The "thermal inertia" (i.e., the ability of a cooling system to damp out meteorological transients and fluctuations in the power plant operation) of a once-through cooling system is usually high. Once-through systems have been very popular among the coastal cities.

b. Cooling lakes

A cooling lake is basically the same as once-through cooling except that the former is an enclosed water body with a limited volume. It is a closed system in the sense that condenser water is recirculated. The steady state performance of a cooling lake is dependent primarily on the lake area, geometry and inlet and outlet structures while their thermal inertia, dependent on lake depth, is comparable with once-through system. Cooling lake offers an attractive alternative of waste heat disposal for many inland power plants where land is readily available adjacent to a source of make-up water or where artificial impoundments can be (or have already been) constructed by damming a nearby river.

c. Cooling towers

Wet cooling towers emit heat directly to the atmosphere primarily through evaporation of the heated water and the process is enhanced by means of a moving air stream. In regions of scarce water supply dry and wet/dry towers are being considered. The principal heat transfer mechanism of a dry cooling tower is conduction between ambient air and the cooling water through the heat exchanger surface. In addition to the construction costs and the disadvantages of requiring regular maintenance, the "thermal inertia" of a cooling tower is relatively small, rendering it less desirable when compared with the other two cooling systems, despite the fact that modular design of cooling towers presents definite merits.

Overall, the availability of land and water, economic factors and social values, and the characteristics of the proposed plant combine together to determine the choice of a waste heat disposal facility.

1.2 North Anna Power Station

The North Anna Power Station is a nuclear power plant operated by Virginia Electric and Power Company, Richmond, Virginia (VEPCO). It is located in Louisa County in central Virginia, 66 km northwest of Richmond and 64 km east of Charlottsville (Figure 1.1). The Station is situated on the south bank of a lake formed by impounding the North Anna River (Figure 1.2) in January of 1972.

The power plant consists of two nuclear units; previous plans which called for third and fourth units have been cancelled. The two nuclear units generate 947 MW and 925 MW respectively with an average thermal efficiency of about 34% which translates into a waste heat load rejected in the condenser cooling system of about 1839 MW per unit.

The condenser cooling water flow rate is about 60 $m^3 s^{-1}$ per unit (4 pumps per unit at 15 $m^3 s^{-1}$ per pump), and the attendant temperature rise while passing through the condenser is about 8°C.

1.3 The Cooling Lake System

A cooling lake system was designed to dissipate the waste heat rejected by the nuclear power plant. Lake Anna was formed by impounding the North Anna River through construction of a dam (see Figure 1.2). Additional dikes were constructed and main channels dredged to form a separate chain of ponds known as the Waste Heat Treatment Facility (WHTF). Both the WHTF and Lake Anna share the burden of dissipating the waste heat load to the atmosphere, though the major portion is dissipated through the WHTF.

At a design elevation of 76 m above mean sea level (MSL), Lake Anna has a surface area of 39 km^2, a volume of 3.0×10^8 m^3, and an

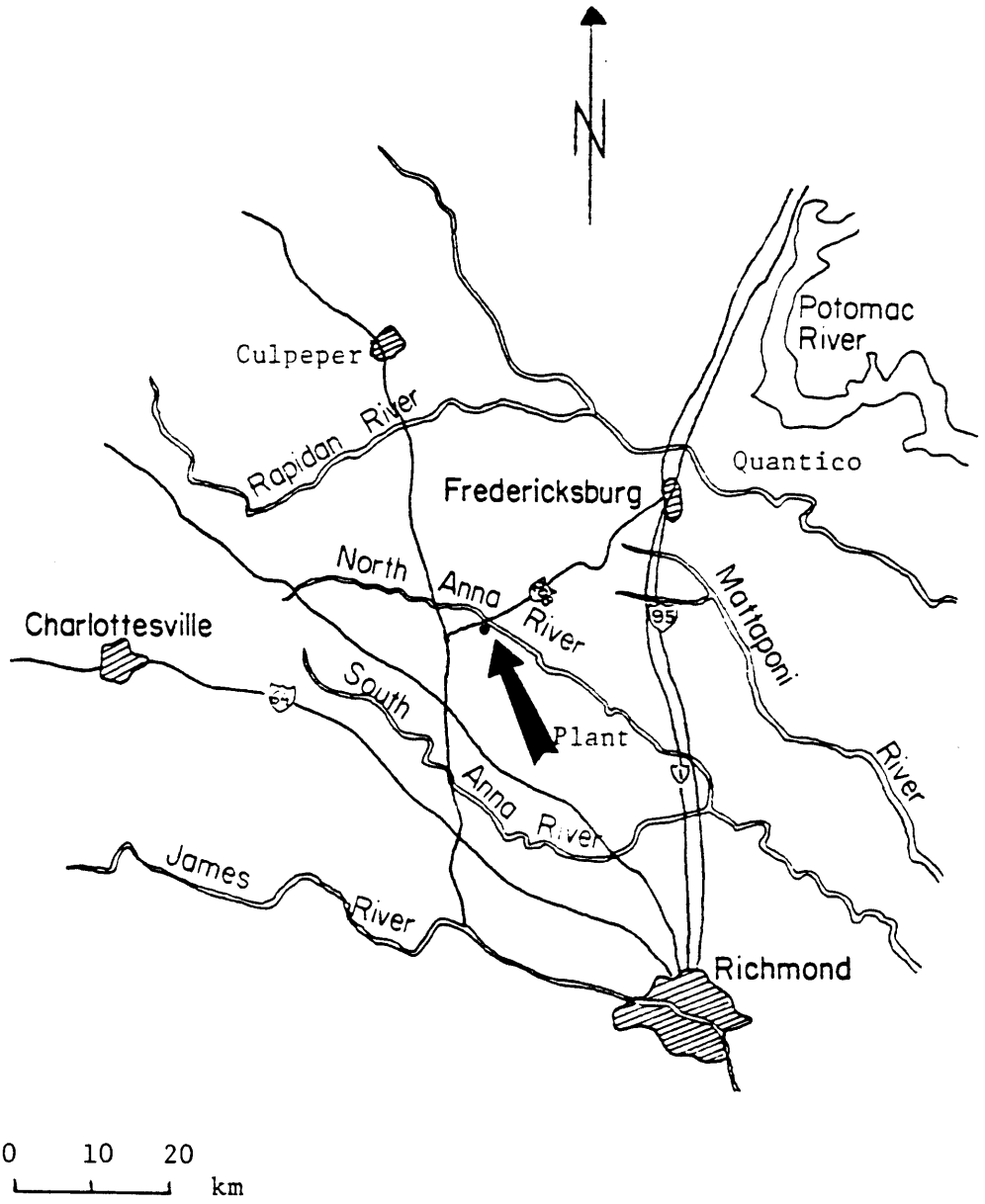

Figure 1.1 Geographical Location of North Anna Power Station, Virginia

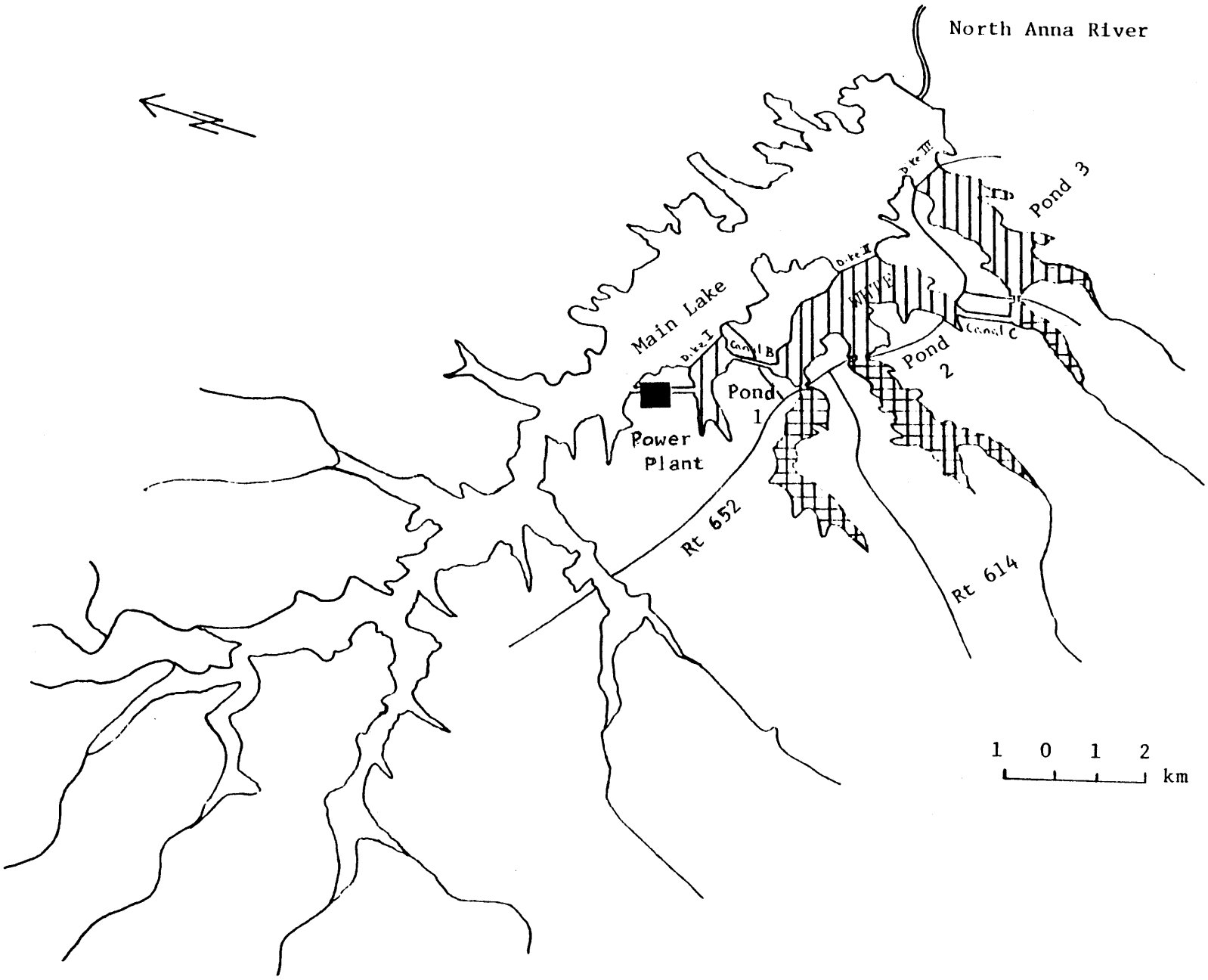

Figure 1.2 North Anna Cooling Lake System

average depth of 7.6 m *. The maximum depth at the dam is 24 m. The lake receives an average annual inflow of about 7.6 $m^3 s^{-1}$. The lake elevation is maintained by three radial gates at the dam and two near-surface skimmers. The outflow rate equals the inflow rate minus the rate of evaporation from the lake surface which is estimated at about 1.7 $m^3 s^{-1}$ for average conditions. Net groundwater seepage is negliglble.

The WHTF has a surface area of 14 km^2, a volume of 7.5×10^7 m^3, and an average depth of 5.5 m. The maximum depth is about 15 m in the vicinity of the dikes. Three dikes have been built to separate the WHTF from Lake Anna (see Figure 1.2). Dike 1 forms Pond 1 of the WHTF which receives the heated water via the discharge canal from the power plant (Figure 1.3). Connecting channels have been dredged between Pond 1 and Pond 2 (formed by Dike 2) and between Pond 2 and Pond 3 (formed by Dike 3). These channels have a constant trapezoidal cross-section of 7.6 m depth and 48.8 m width. After passing through Ponds 2 and 3, the cooling water is discharged into the main lake through a submerged discharge structure at Dike 3. After residence in the main lake, cooling water is withdrawn through intakes over the upper 9 m in the upstream vicinity of the station.

In summary, the cooling lake system of the North Anna Power Station is essentially a closed system which consists of a series of ponds (the WHTF) and a main lake (Lake Anna). A major characteristic of the system is the existence of long narrow side arms in the WHTF.

---

*all figures related to lake dimension, etc. in Section 1.3 are adopted from Wells et al (1982).

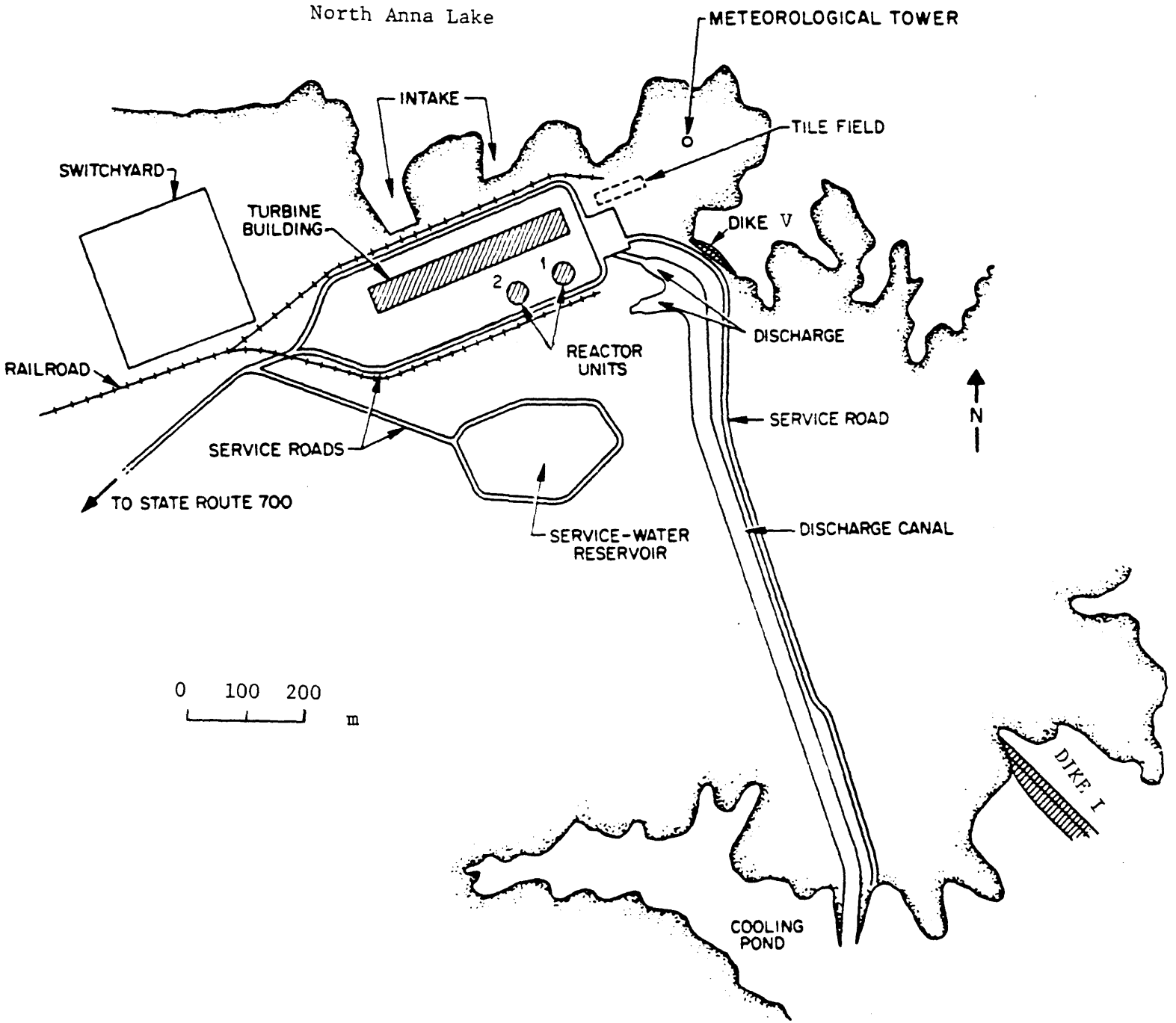

Figure 1.3 Discharge Canal from the Power Plant

These side arms comprise about 6.2 km^2 or 45% of the total surface area of the WHTF.

2. REVIEW OF PREVIOUS INVESTIGATIONS

2.1 Introduction

Proper understanding of the thermal structure of an artificially heated water body such as the cooling lake system of the North Anna Powr Station is fundamental in assessing the impacts that the waste heat discharge has on the natural environment. This should be apparent since most of the physical, chemical and biological processes which take place in an aquatic ecosystem are closely tied to the temperature regime. From the standpoint of the electric power generation industry, assessment of the efficiency of a cooling lake system also necessitates the study of the thermal structure of the cooling lakes through which waste heat is dissipated.

Mathematical models were developed to simulate the temperature regime of the cooling lake system at North Anna Power Station. This represents a continuous effort which commenced before the power plant first started its one-unit operation in July, 1978. Technical reports which resulted from the earlier development stage, and upon which the present research is based, include Watanabe et al. (1975), Brocard et al. (1977), Octavio et al. (1977), Jirka et al. (1977) and Wells et al. (1982). Since this research effort is coming to a natural conclusion, it is appropriate for the author to give a brief review of the previous investigations so that one may see the line along which the mathematical model has been developed.

2.2 Initial Model Development Stage

Watanabe et al. (1975) indicated the limitations of the then existing model for predicting cooling lake behavior. He rightly

assessed that steady-state models are of limited value in design and prediction owing to the inherently unsteady meteorology and plant heat loading. He developed a transient stratified cooling lake model which included a two-dimensional horizontal temperature prediction on the surface layer by improving Ryan and Harleman's model (1973).

Before Brocard et al. (1977), very little research effort had been made to determine the effects of side arms on the overall performance of a cooling lake, although it had been known for a long time that side arms are a common feature of cooling lakes with natural shorelines and that they may constitute a large portion of the cooling lake's total surface area. Brocard et al. (1977) developed a model for the side arm circulation applicable to both laminar and turbulent flows involving the division of the side arm in a "two layer flow region" and a "downflow region". Since then the side arm model has become an integral part of our present cooling lake model.

Octavio et al. (1977) dealt with basic research into the physical processes affecting the temperature structure of lakes and reservoirs. The M.I.T. Reservoir Model was modified to include the influence of wind via an iterative heating-wind mixing procedure. The natural (ambient) temperature regime of Lake Anna was predicted using the modified model and good agreement between predictions and measurements were reported.

The North Anna Cooling Lake Model began to assume its present form with the effort contributed by Jirka et al. (1977). A transient segmented cooling lake model was developed which links the mathematical models applicable to the main lake and those to the components of the WHTF. The model was then utilized in ten-year simulations (with

synthetic meteorological data series) to evaluate the thermal impacts of the power plant upon the lake system under one, two, three and four-unit operations.

2.3 Late Model Development Stage

While initial development of the North Anna Cooling Lake Model, calibration based on pre-operational data, and predictions under various levels of station operation for the historical period of 1957 - 1966 were documented in Jirka et al. (1977), no validation of the model was presented with operational data until Wells et al. (1982).

Since Unit 1 of the nuclear power plant came on line in summer of 1978 (followed by Unit 2 in autumn of 1980), an extensive data collection effort was undertaken to calibrate the model to operational data. Continuous measurements were made of meteorological variables, plant load, water temperature at various points in the system and current speeds in one of the WHTF side arms. Supplemental data, with greater spatial resolution, were collected at weekly or monthly intervals. Calibration of both the hydraulic and hydrologic components of the model were made in the following areas: (1) surface heat transfer processes, (2) temperatures in the main lake and (3) temperatures in the WHTF. (A review of the calibrations and changes in the model is given in Section 3.6.) Predictions given by the calibrated model were then compared against a three-year record of operational data (1978-1981).

3. NORTH ANNA COOLING LAKE MODEL

3.1 Introduction

A detailed description of the modelling approach as well as the development and interfacing of the various components of the North Anna Cooling Lake Model was given by Jirka et al. (1977). A summary of the basic structure, as originally developed, was included in Chapter 2 of Wells et al. (1982). Much of the material in the following sections of this chapter is summarized from their work.

The North Anna Cooling Lake Model is a segmented mathematical model which consists of different models for different parts of the North Anna lake system. A schematization of the geometry used in the modelling approach is illustrated in Figure 3.1. Specifically, three distinct features are significant:

(1) the three cooling ponds of the WHTF,

(2) the dead-end side arms of the WHTF and that of the main lake, and

(3) the main lake.

In the following sections a summary of the basic structure of the sub-models applied to each part is presented.

3.2 Model for Waste Heat Treatment Facility

3.2.1 Outline of Model

Three geometrically and structurally different components within the WHTF are recognized: (1) the three WHTF ponds, (2) the long dead-end side arms of the WHTF ponds, and (3) the interconnecting

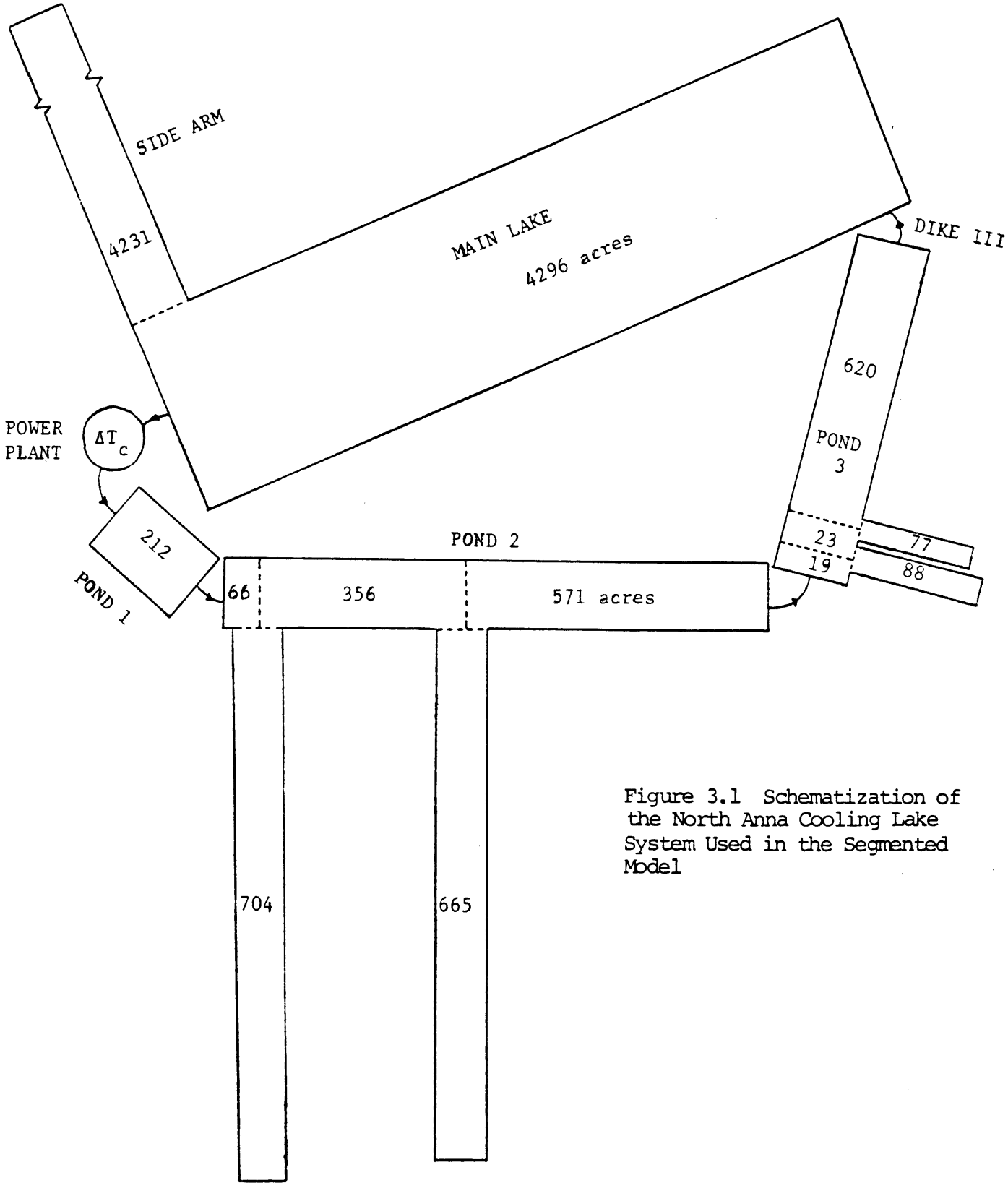

Figure 3.1 Schematization of the North Anna Cooling Lake System Used in the Segmented Model

channels. Side arm modelling is discussed in Section 3.2.2. Two different models are postulated for the vertical thermal structures of the WHTF ponds and the interconnecting channels based on their densimetric Froude numbers:

$$Fr = \frac{u}{\sqrt{\frac{\Delta\rho}{\rho} gh}} \qquad (3.1)$$

where u = characteristic velocity, g = gravitational acceleration, h = characteristic water depth, $\Delta\rho$ = characteristic density difference between upper and lower layers, and ρ = reference water density.

Because of the relatively large dimensions of the three WHTF ponds (refer to Section 1.3), the average velocities are low, and therefore $Fr < 1$. The WHTF ponds are thus expected to stratify; consequently, a two-layer model is used in which each layer is assumed to be vertically well mixed, with neither heat nor mass flux allowed to pass through the interface between the layers, except at the ends. (Modelling of the WHTF ponds is discussed in Section 3.2.3.)

Conversely, because of the small dimensions of the interconnecting channels, velocity is high, rendering $Fr > 1$, and thus the channels are modelled as a fully mixed system.

A significant parameter in modelling the WHTF system is the quantity of mixing between an interconnecting channel and the downstream pond. Ideally, mixing should be minimized to promote

maximum heat dissipation. The following empirical formula is utilized to calculate the dilution, D_s (Jirka, Abraham and Harleman, 1975):

$$D_s = 1.4 \sqrt{1 + Fr^2 \left(\frac{h}{b}\right)^{1/2}} \left[\frac{0.75}{h_{max}/H}\right]^{0.75} \qquad (3.2)$$

where D_s = dilution ratio, $(Q_o + Q_e)/Q_o$, Q_o = discharge flow rate, Q_e = entrained flow rate, h = depth of discharge channel, b = half-width of discharge channel, h_{max} = maximum jet penetration of deep-water jet, H = water depth, Fr = densimetric Froude number within the interconnecting channel.

The value of h_{max} is calculated from the buoyant surface jet model of Stolzenbach and Harleman (1971):

$$\frac{h_{max}}{H} = 0.42 \, F_r \left[\frac{h}{b}\right]^{1/4} \sqrt{hb} \qquad (3.3)$$

Data supporting Eqs. 3.2 and 3.3 can be found in Jirka et al. (1981).

3.2.2 Model for Side Arm

The convective circulation in a dead-end side arm (schematized in Figure 3.2) is a phenomenon whereby warm surface water from the main pond spreads into the side arm, gradually losing its heat to the atmosphere. The gradual decrease in density difference causes the inflowing water to sink and be replaced by new warm water. In the context of the North Anna Model, the entrance temperature distribution

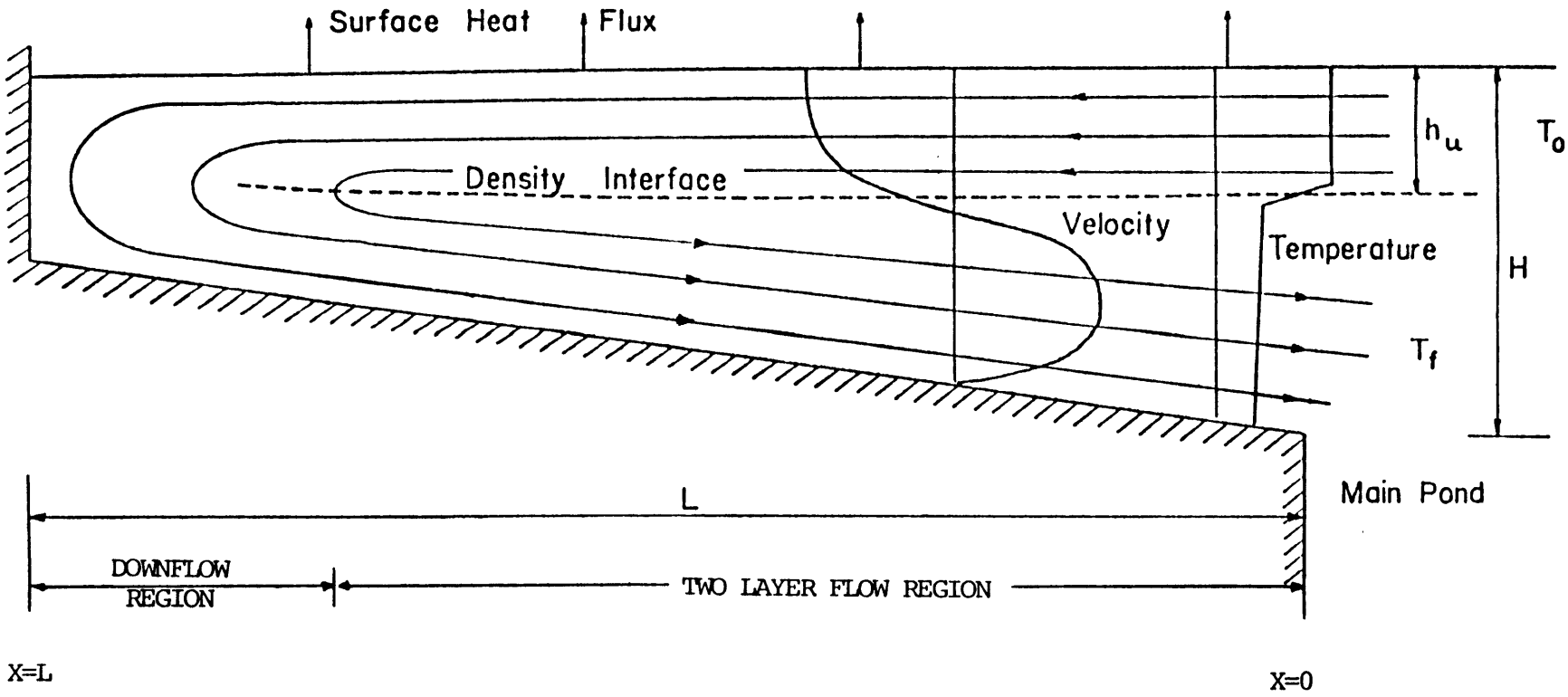

Figure 3.2 Schematization of Convective Circulation in a Dead-End Side Arm

and the surface heat fluxes are the independent variables, while the flow rate and the temperature of the return flow are to be determined.

This phenomena was studied by Brocard et al. (1977) who presented a model for solving the problem. The following assumptions were made to simplify the analysis:

(1) horizontal bottom, i.e., $dH/dx = 0$

where H = depth of the side arm,

x = longitudinal distance up the side arm;

(2) downflow occurs only at the end of the side arm;

(3) small values of $KL/\rho C_p q_o$,

where L = length of side arm,

q_o = side arm flow per unit width,

ρ = density of water,

C_p = specific heat of water,

K = surface heat exchange coefficient;

(4) negligible effect of the lateral bridge constriction on side arm flow.

Their equation derived for the side arm flow is:

$$\frac{q_o}{KL} = \left\{B \frac{f_o L}{H} \frac{1}{4h_o} \left[\alpha\left(\frac{1}{h_o} - \frac{\Delta q-1}{1-h_o}\right)^2 \left(\frac{1}{h_o} + \frac{1}{1-h_o}\right) + \frac{(\Delta q-1)^2}{(1-h_o)^3}\right]\right\}^{-1/3} \qquad (3.4)$$

where B = buoyancy term = $\dfrac{k^2 L^2}{\beta(T_o - T_E)gH^3}$

h_o = initial upper layer depth

β = coefficient of thermal expansion of water = $-\frac{1}{\rho}\frac{\partial \rho}{\partial T}$

$\Delta q = \frac{q_1 - q_2}{q_o} \simeq 0$

$\alpha = \frac{f_i}{f_o} \simeq 0.5$

T_o = initial temperature at side arm entrance

T_E = equilibrium temperature

f_o = bottom friction factor

f_i = interfacial friction factor

q_1 = upper layer flow

q_2 = lower layer flow

k = kinematic surface heat exchange coefficient = $\frac{K}{\rho C_p}$

The temperature distribution along the side arm can be determined once q_o is known. In the North Anna Model, the equation used for the return temperature has been

$$\frac{T_f - T_E}{T_o - T_E} = \exp(-0.8 \frac{kL}{q_o}) \qquad (3.5)$$

where T_f = final or return temperature. The 0.8 factor in Eq. 3.5 can be thought of a dispersion effect, reducing the "effective" length of the side arm by 20%.

In order to solve for the side arm flow rate and the return temperature, the mixed layer depth and the temperature of the mixed layer in the WHTF pond are inputs to the side arm model together with the side arm geometry and meteorological conditions.

3.2.3 Model for WHTF Ponds

Two situations exist with regard to the mathematical modelling of the temperature distribution in the three WHTF ponds:

(1) one pond with no side arms (Figure 3.3) and

(2) two ponds each with two side arms (Figure 3.4).

For the pond with no side arms, the temperature of the entrained water is equal to T_2, the temperature at the end of the pond, since no heat flux is allowed through the interface. By means of a heat balance, the temperature of the upper layer waters at the end of the mixing zone can be given by

$$T_1 = \frac{T_o + (D_s - 1)T_2}{D_s}$$

$$\text{or} \quad T_1 - T_E = \frac{(T_o - T_E) + (D_s - 1)(T_2 - T_E)}{D_s} \tag{3.6}$$

If the pond is treated as a one-dimensional steady state system, the governing differential equation along it becomes

$$\frac{dT}{dA} = \frac{\phi_n}{\rho C_p Q} = \frac{-K(T - T_E)}{\rho C_p Q} \tag{3.7}$$

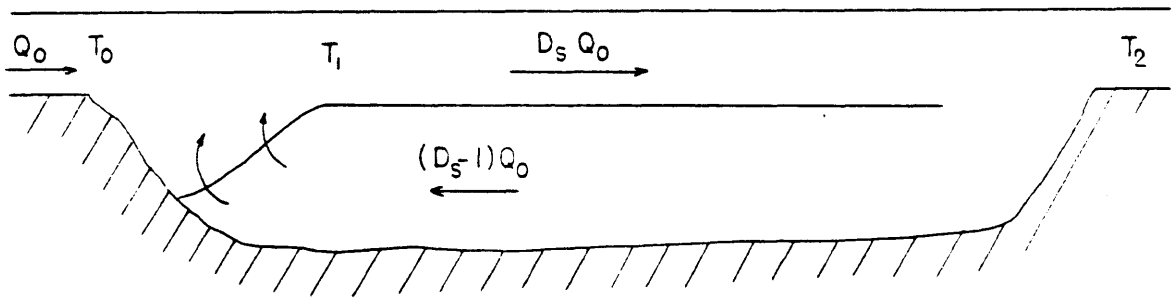

Figure 3.3 Flow Configuration of a Pond without Side Arm

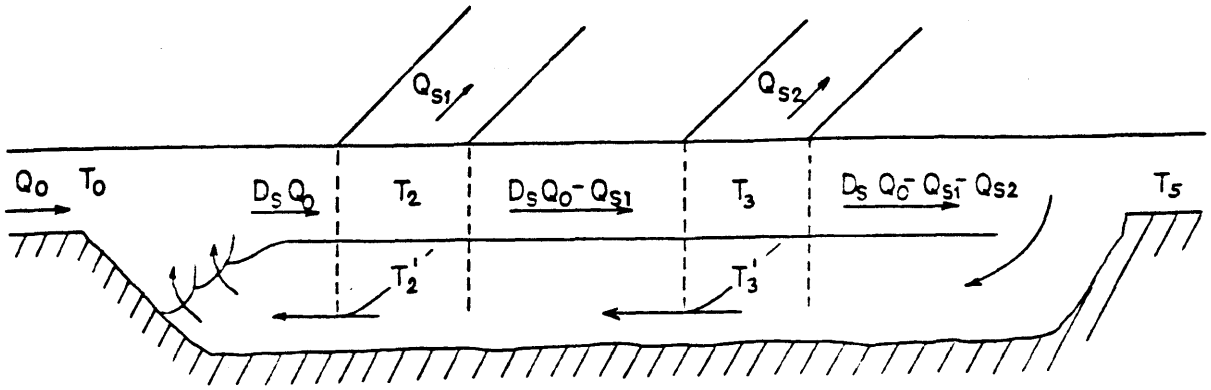

A. Flow Configuration in a Reach with Two Side Arms for $(D_s-1)\ Q_o > Q_{s1} + Q_{s2}$

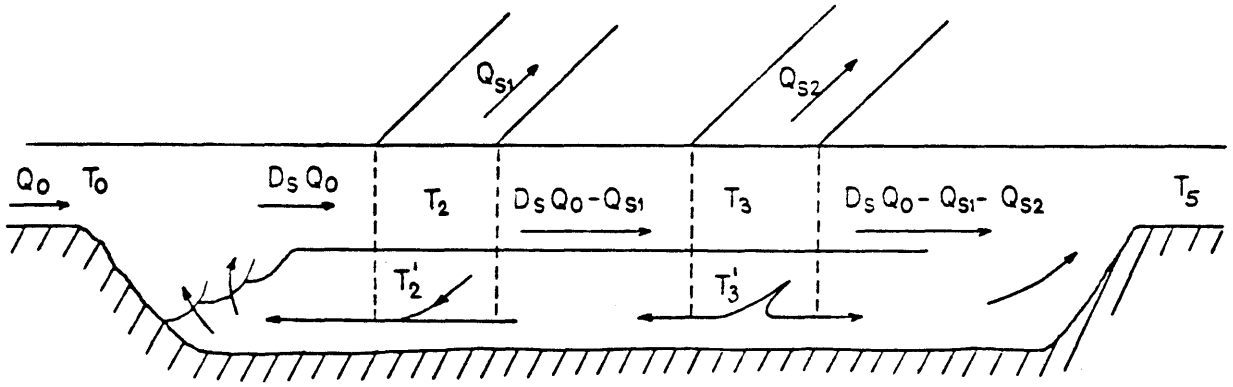

B. Flow Configuration in a Reach with Two Side Arms for $Q_{s1} < (D_s - 1)\ Q_o < Q_{s1} + Q_{s2}$

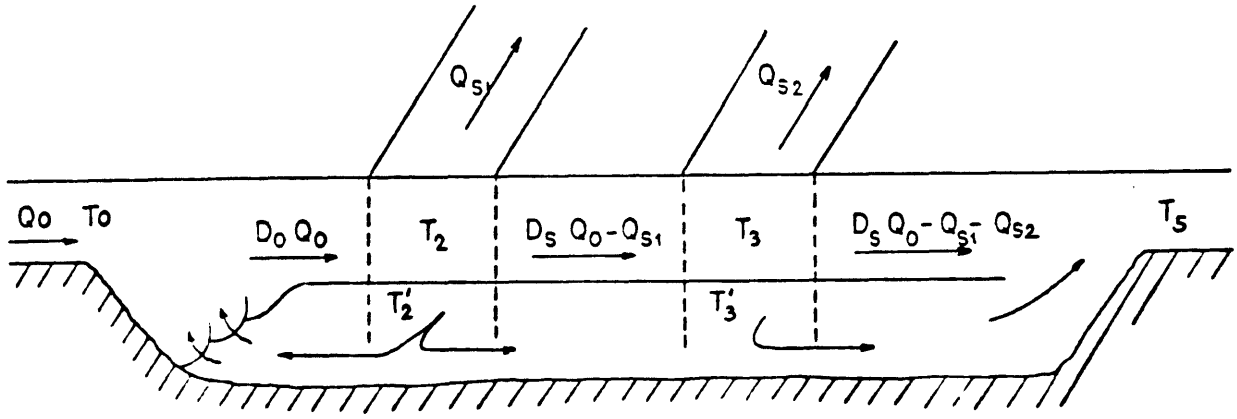

C. Flow Configuration in a Reach with Two Side Arms for $(D_s - 1)\ Q_o < Q_{s1}$

Figure 3.4 Flow Configurations of a Pond with Two Side Arms

where A = incremental area,

Q = flow rate in upper layer,

ϕ_n = net heat flux.

By integrating Eq. 3.7 across the pond, the steady state equation for the temperature distribution in the first WHTF pond (Pond 1) is

$$\frac{T_2 - T_E}{T_1 - T_E} = \exp\left(- \frac{KA}{\rho C_p D_s Q_o} \right) = e^{-r} \qquad (3.8)$$

From Eqs. 3.6 and 3.8 one obtains the following equation for Pond 1:

$$\frac{T_2 - T_E}{T_o - T_E} = \frac{e^{-r}}{D_s - (D_s - 1)e^{-r}} \qquad (3.9)$$

As shown in Figure 3.4, the flow in a pond with two side arms can take on three different possible configurations:

(1) the jet entrainment flow is greater than the sum of the side arm flows, i.e., $(D_s-1)Q_o > Q_{s1} + Q_{s2}$,

(2) the jet entrainment flow is greater than the first side arm flow but smaller than the sum of the side arm flows, i.e., $Q_{s1} < (D_s-1)Q_o < Q_{s1} + Q_{s2}$, and

(3) the jet entrainment flow is smaller than the first side arm flow, i.e., $(D_s-1)Q_o < Q_{s1}$.

Analysis of the thermal structure in the case of a pond with two side arms is simliar to that of a pond without side arm: the same governing equation (Eq. 3.7) is integrated over sections of the pond

between side arm locations and then simplified by a heat balance describing mixing of the flow within the pond and at the side arms' entrance or exit. Since the results are quite lengthy, they are not reproduced here; the reader is referred to pages 64-80 of Jirka et al. (1977). Also since the solution for the pond temperature in this case is complicated by the different possible configurations of the flow structure, an iterative process must be used in the computation.

3.3 Model for Dike III Mixing

A plan view of the submerged jet discharge at Dike 3 is given in Figure 3.5. The jet model of Stolzenbach and Harleman (see Eqs. 3.2 and 3.3) is invoked to evaluate entrance mixing. However, a condition of critical flow at the triangular constriction (Figure 3.6) dictates the maximum exchange flow:

$$\frac{(Q_o + Q_e)^2/A_T^2}{\frac{\Delta\rho}{\rho} g\, h_T} + \frac{Q_e^2/A_B^2}{\frac{\Delta\rho}{\rho} g h_B} = 1 \qquad (3.10)$$

where A_T = area of top section,

h_T = depth of top section,

A_B = area of bottom section,

h_B = depth of bottom section,

Q_e = entrained flow,

Q_o = jet discharge.

One can notice that the computed entrainment flow may exceed the flow which could be exchanged across the section. An analysis of critical

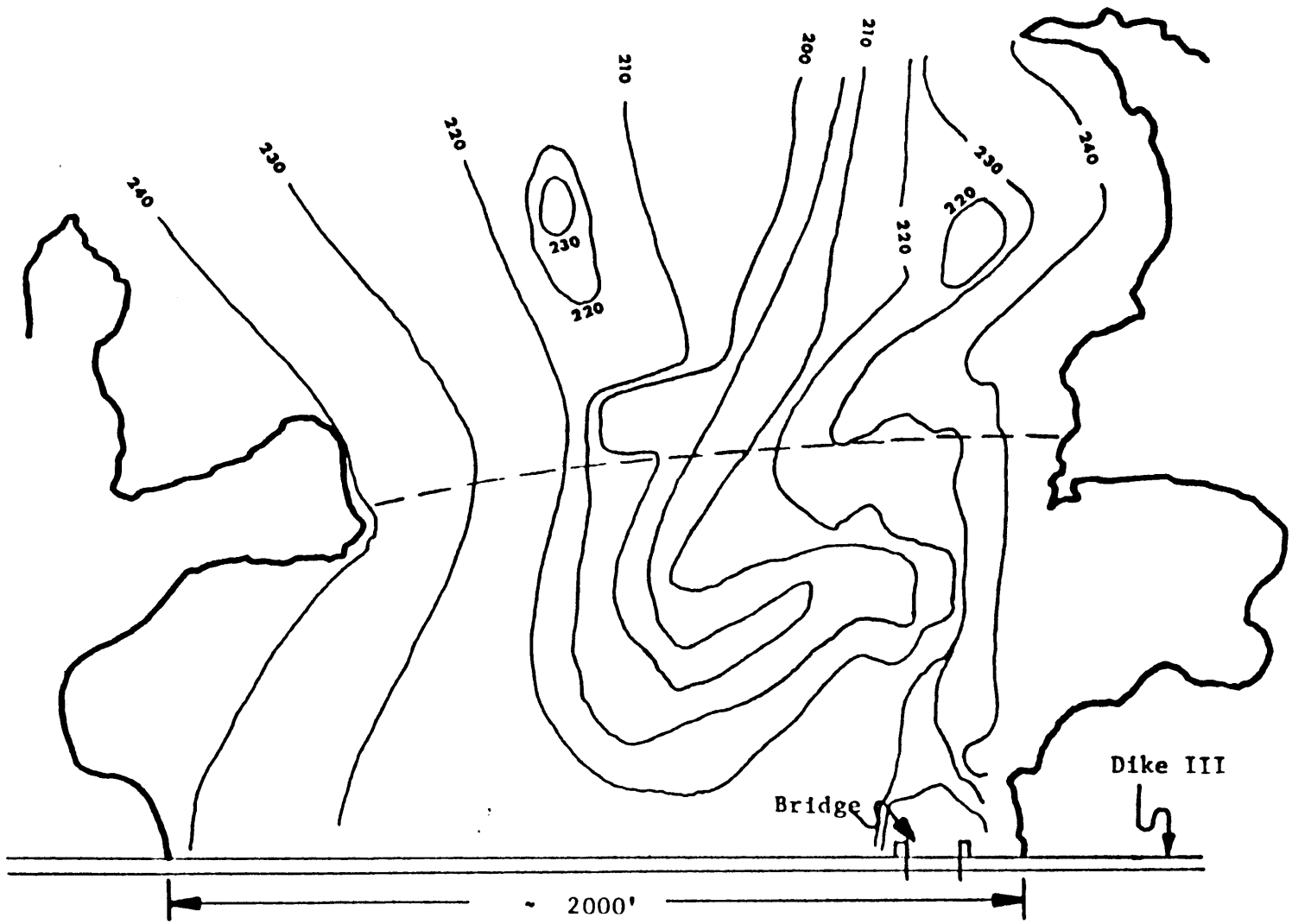

Figure 3.5 Plan View of Submerged Jet Discharge at DIKE III
(Contour Lines are in Feet above MSL)

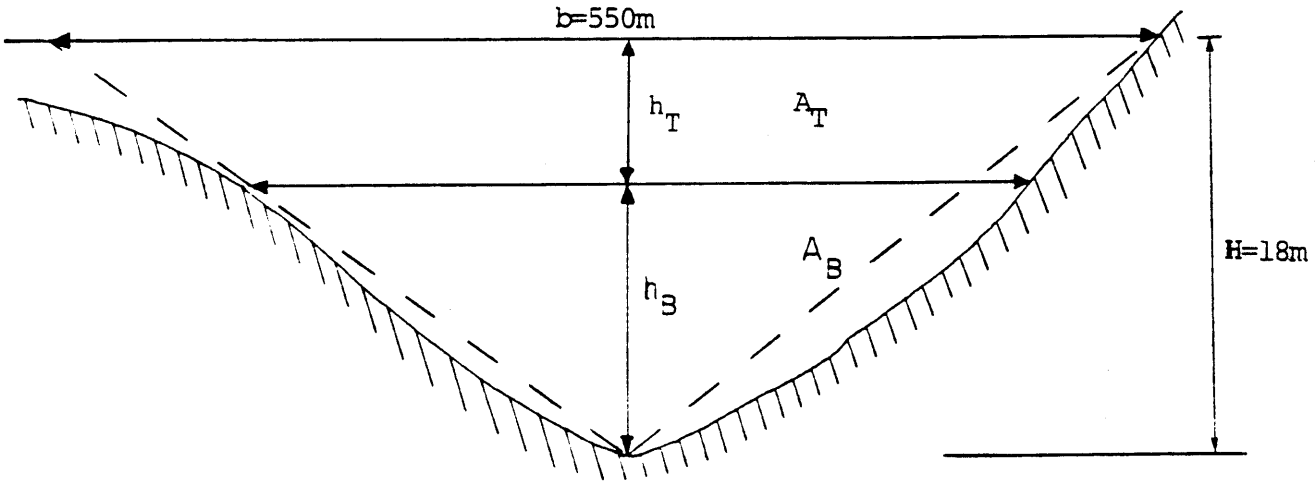

Figure 3.6 Cross Section of Dike III Constriction

flow provides an equation in dimensionless form to compute the entrance dilution based on the geometry of the constriction:

$$\frac{(1 + \frac{Q_e}{Q_o})^3 \; (\frac{Q_e}{Q_o})^2 \; (1 + \frac{Q_e}{Q_o})}{(\frac{h_T}{H})^3 \; (2 - \frac{h_T}{H})^2 \; (1 - \frac{h_T}{H})^5} = \frac{b^2 H^2}{4 Q_o^2} \; g \; (\frac{\Delta\rho}{\rho})_o \qquad (3.11)$$

where $H = h_T = h_B$ = total depth,

b = top width,

$(\frac{\Delta\rho}{\rho})_o$ = value of $\Delta\rho/\rho$ between jet water and entrained cold water.

Eq. 3.11 is solved by trial and error for the maximum value of Q_e/Q_o which obeyed the stipulation that $0 < h_T/H < 1$.

3.4 Main Lake Model

3.4.1 Outline of Model

The main lake (Lake Anna) is modelled according to its three different sections:

(1) a vertically well-mixed surface layer of constant thickness and horizontally-varying temperture distribution $T(x,t)$,

(2) a vertically stratified subsurface pool of uniform horizontal temperature distribution $T(z,t)$, and

(3) a side arm attached to the end of the main lake that has a return flow into the subsurface pool.

The combined surface and subsurface models are essentially modified from Ryan and Harleman (1973), while the analysis of the side arm flow

follows that discussed in Section 3.2.2.

3.4.2 Finite Difference Model for Surface Layer

A one-dimensional, transient model is used based on the following governing equation:

$$\frac{\partial T}{\partial t} = -\frac{Q}{H_s}\frac{\partial T}{\partial A} - \frac{\phi_n}{\rho C_p H_s} \tag{3.12}$$

where H_s = depth of surface layer,

ϕ_n = net surface heat flux.

Eq. 3.12 is put into finite difference form, and the surface temperature along the lake, in 40 areal increments, is predicted as a function of time. Using a steady-state momentum equation for the heated surface layer, Watanabe et al. (1975) developed the following expression for the value of H_s:

$$H_s = \left(\frac{f_i Q_o^2 D_{sv}^3 L^3}{4\beta \Delta T_L g A_p^2}\right)^{1/4} \tag{3.13}$$

where f_i = interfacial friction factor

Q_o = discharge flow rate

D_{sv} = vertical entrance dilution factor

A_p = total pond area

L = longitudinal pond dimension

β = thermal expansion coefficient

ΔT_L = surface temperature difference between dam and intake

g = gravitational acceleration

3.4.3 Finite Difference Model for Subsurface Layer

The hypolimnion of Lake Anna is modelled by a series of horizontally uniform layers which are vertically stratified. Heat transfer occurs by diffusion, advection, convective mixing and radiation absorption. The governing equations for this one-dimensional vertical model are as follows:

(1) Heat Transport Equation

$$\frac{\partial T}{\partial t} + \frac{1}{A}\frac{\partial}{\partial z}(Q_v T) = \frac{D_z}{A}\frac{\partial}{\partial z}\left(A\frac{\partial T}{\partial z}\right) + \frac{Bu_i T_i}{A} - \frac{Bu_o T}{A} - \frac{1}{\rho C_p A}\frac{\partial (A\phi_z)}{\partial z} \qquad (3.14)$$

(2) Surface Boundary Condition

$$D_z \frac{\partial T}{\partial z} = \phi_n \quad \text{at } z = z_s \qquad (3.15)$$

(3) Bottom/Side Boundary Condition

$$\frac{\partial T}{\partial z} = 0 \quad \text{at } z = 0 \qquad (3.16)$$

(4) Continuity Equation

$$Q_v = B\int_0^z u_i(z,t)dz - B\int_0^z u_o(z,t)dz \qquad (3.17)$$

where $\phi_z = \phi_o(1-\beta)e^{-\eta(z_s-z)}$

ϕ_o = net incident solar radiation

ϕ_n = net heat flux

β = fraction of short wave radiation absorbed at water surface (= 0.5)

η = extinction coefficient (= 0.75 m^{-1})

z_s = water surface elevation

B = width of main lake

u_i, u_o = velocity of inflow, outflow, respectively

Q_v = vertical flow (advection)

D_z = vertical diffusion coefficient

A = area of main lake

T_i = inflow temperature

These governing equations are put in finite difference form and solved along with the surface layer model using an explicit time scheme. At the end of each time step the vertical stability of the water column is checked and, if necessary, convective overturning is performed.

3.5 Summary of Model

In the North Anna Cooling Lake Model, the WHTF ponds and side arms were formulated as basically steady state models, while the main lake formulation was transient. In order to account for the transients in the WHTF, a lagging criterion was used, based on the residence time of each pond. For example, the predicted temperature at day j, at the end of a pond with a residence time of n days, was calculated from the flow rate and initial temperatures for day j-n. In this manner temperatures were lagged throughout the WHTF. The flow rate and temperature computed for the end of Pond 3 became the inflow rate and inflow

temperature for the Dike 3 jet mixing formulation of the main lake.

The diluted flow in the upper layer of the main lake exceeds the condenser flow rate withdrawn at the intake by the entrainment associated with Dike 3 mixing (Figure 3.7). This extra flow is down-welled to the sub-surface model. This down-welling takes place from the last longitudinal segment in the finite difference representation of the surface layer model into the top segment of the finite difference representation of the sub-surface model. To summarize, the inputs to and from the stratified sub-surface model are the Dike 3 entrainment, the main lake side arm return flow, the intake withdrawal and down-welled surface flow. The North Anna River inflow and outflow were neglected because of their generally small magnitudes in comparison to the condenser flow rate.

A time step of one day along with daily-averged input data was used for all simulations.

3.6 Previous Calibrations of Model

Wells et al. (1982) calibrated the model using the first three years of operational data. Compared with the original model used by Jirka et al. (1977) which was outlined in the previous five sections of this chapter, Wells et al. introduced the following basic changes:

(1) a formula by Idso and Jackson (1969) for calculating the net long-wave atmospheric radiation was used to replace the one by Swinbank (1963) in order to increase predicted temperatures during the winter,

(2) a periodic function was applied to adjust the evaporation formula used in the WHTF to account for the non-uniformity of

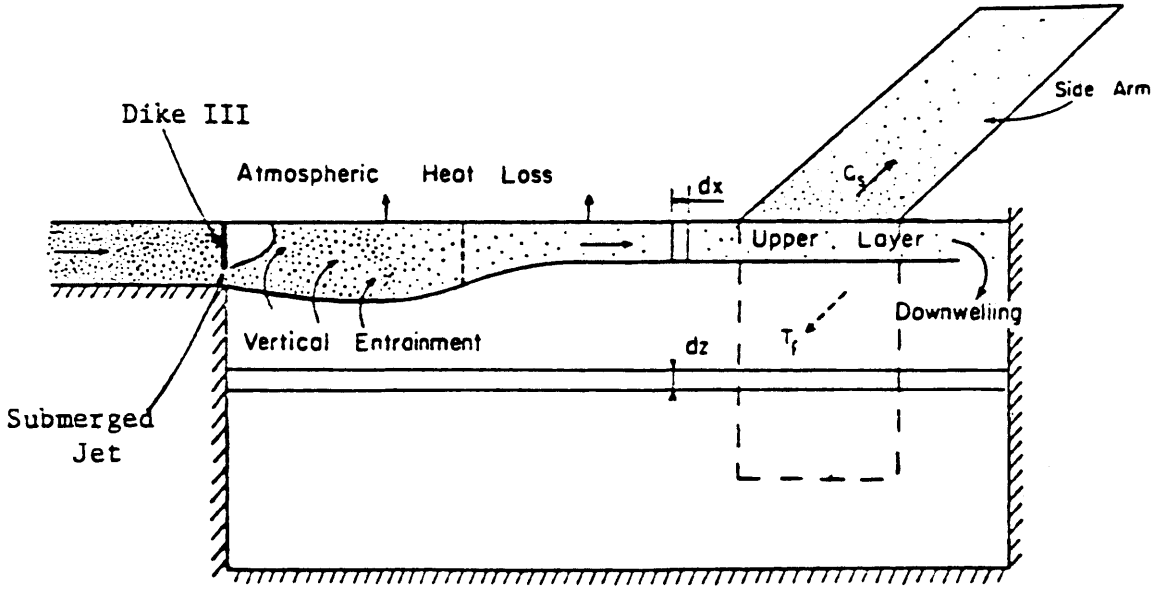

Figure 3.7 Schematization of Main Lake Model

air temperature, relative humidity and wind speed over the lake which were found to be seasonally dependent (see p. 74, Wells et al.),

(3) the condenser intake was allowed to withdraw water equally over the upper 9 m of the main lake to account for the two-dimensional characteristics of the thermal structure near the intake,

(4) a time-varying vertical diffusion coefficient, D_z, dependent on wind speed, condenser flow rate and vertical density gradient was used to replace the constant molecular diffusivity,

(5) an exponential filter was implemented for filtering both the equilibrium temperature and surface heat transfer coefficient to better account for the transients in the WHTF, and

(6) the side arm flow rates were adjusted based on the constrictions due to bridge piers (see also Adams and Wells, 1984).

In general, these modifications improved the predictive power of the model over the original version. A discussion of the performance of the calibrated model in a five-year simulation is given in the next chapter.

4. SURFACE TEMPERATURE ERROR ANALYSIS

4.1 Introduction

Since Unit 1 of North Anna Power Station came on line in summer of 1978 (followed by Unit 2 in autumn of 1980), an extensive data collection network was established by VEPCO. This program has continued, with minor modifications, through the autumn of 1983.

Input to North Anna Cooling Lake Model requires daily-averaged meteorological data (air temperature, wind speed, relative humidity, cloud cover and short wave solar radiation), plant flow rate, temperature rise across condenser, and an initial thermal structure of the main lake. These data are obtained along with information used for calibration purposes, such as water temperature at various points in the cooling lake system and current speeds in one of the WHTF side arms, and data used to evaluate downstream thermal impact and compliance measurements, such as flow data from the North Anna Dam. A detailed description of the data collection effort made by VEPCO is given in Chapter 3 of Wells et al. (1982) and thus will not be reproduced here.

Wells et al. (1982) calibrated the model using data segments from the first three years of operational data (1978-1981) and then validated the model by comparing the continuous model predictions with measurements over the same period. Since then more measurement data were available and a completely independent validation would be to compare model predictions with data for the following two years (1981-1983) using the same model calibrations.

Comparisons between model predictions and measurements are made for the surface temperatures at four diagnostic control points. For the sake of comparison, results of all five years of simulation (26 July 1978 to 30 September 1983 inclusive; a total of 1893 days) are presented in the plots (Figures 4.2 to 4.4). The first 1162 days are mere duplicates of what were presented in Wells et al. (1982).

4.2 Raw Error

Surface temperature error analysis is made for the four representative diagnostic control points over the cooling lake system (Figure 4.1). They are (1) at the discharge of Channel 1 into Pond 1 of the WHTF (hereafter referred to as DISCHARGE), (2) just upstream of Dike III in the WHTF (DIKE III), (3) in the main lake outside the Dike III jet mixing zone near Burrus Point (BR.PT.), and (4) in the main lake near the plant intake (INTAKE).

Figures 4.2a to 4.2d compare the observed surface temperatures with corresponding predictions for 1893 days since July 26, 1978. (Small gaps of missing measurement data of up to a continuous period of 15 days were filled in by curve-fitting.) While these plots show that the model simulates the surface temperatures with reasonable accuracy, a more rigorous error analysis necessitates plotting raw errors (henceforth defined as prediction - measurement) with time.

Figures 4.3a to 4.3d show the raw errors at the four diagnostic control points. (A positive error means that the model was over-predicting, and 15°C indicates missing data.) The raw errors seem to be occuring quite randomly at BR.PT. and INTAKE with mild amplitudes at the annual period; however, a conspicuous periodicity at the annual

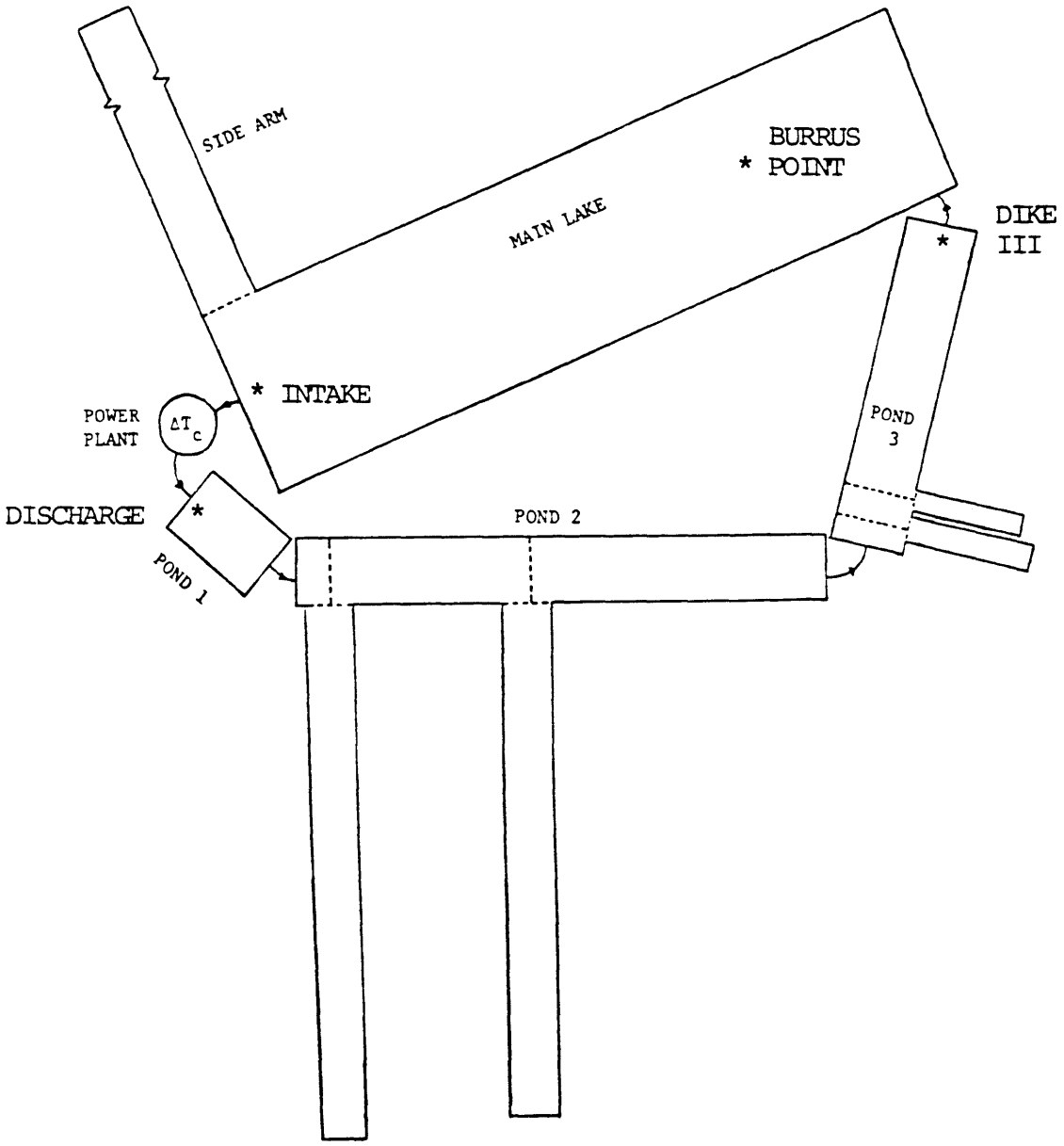

Figure 4.1 Schematization of the Locations of the Four Diagnostic Control Points

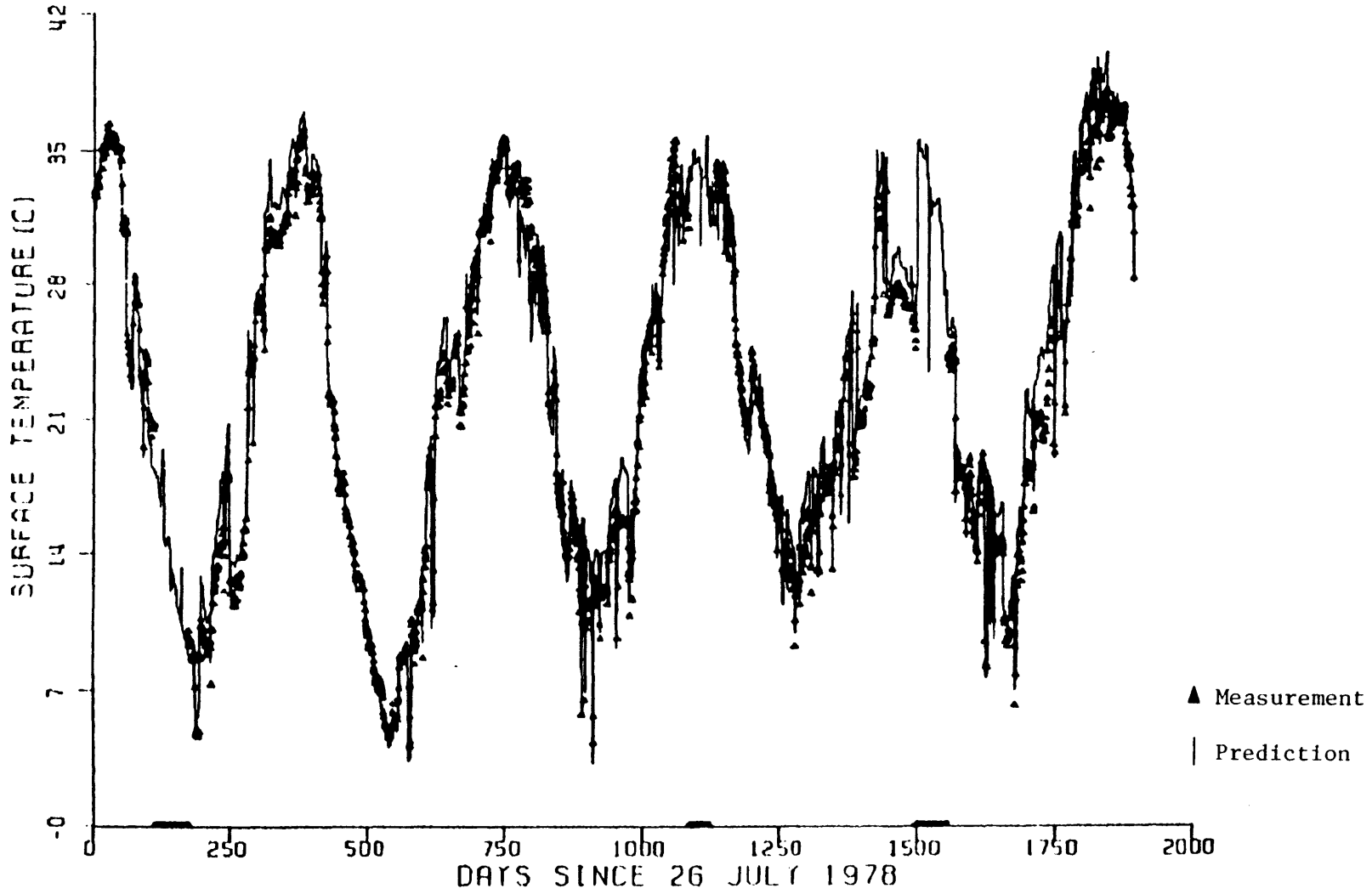

Figure 4.2a Measured vs. Predicted Surface Temperature at DISCHARGE

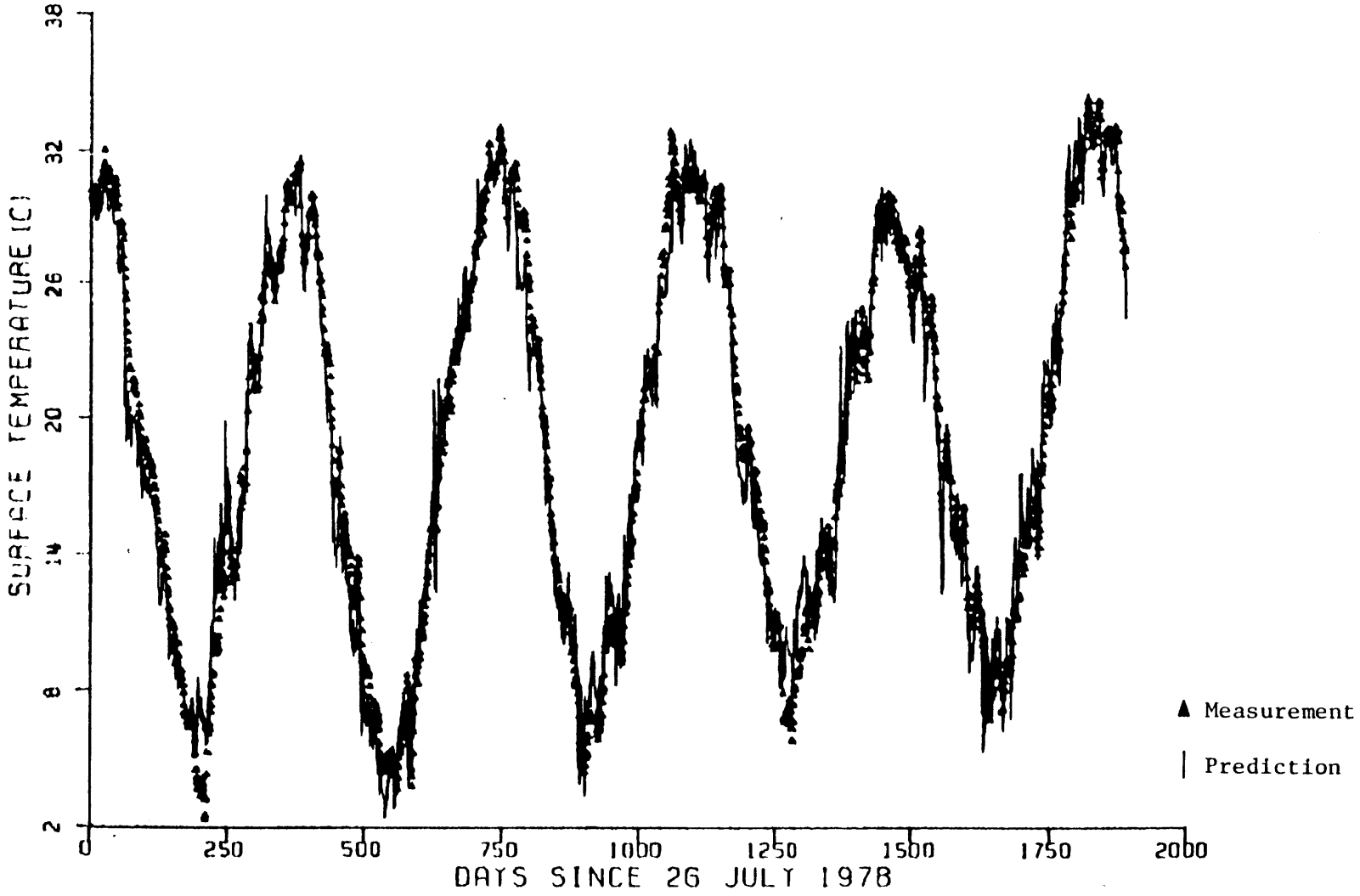

Figure 4.2b Measured vs. Predicted Surface Temperature at DIKE III

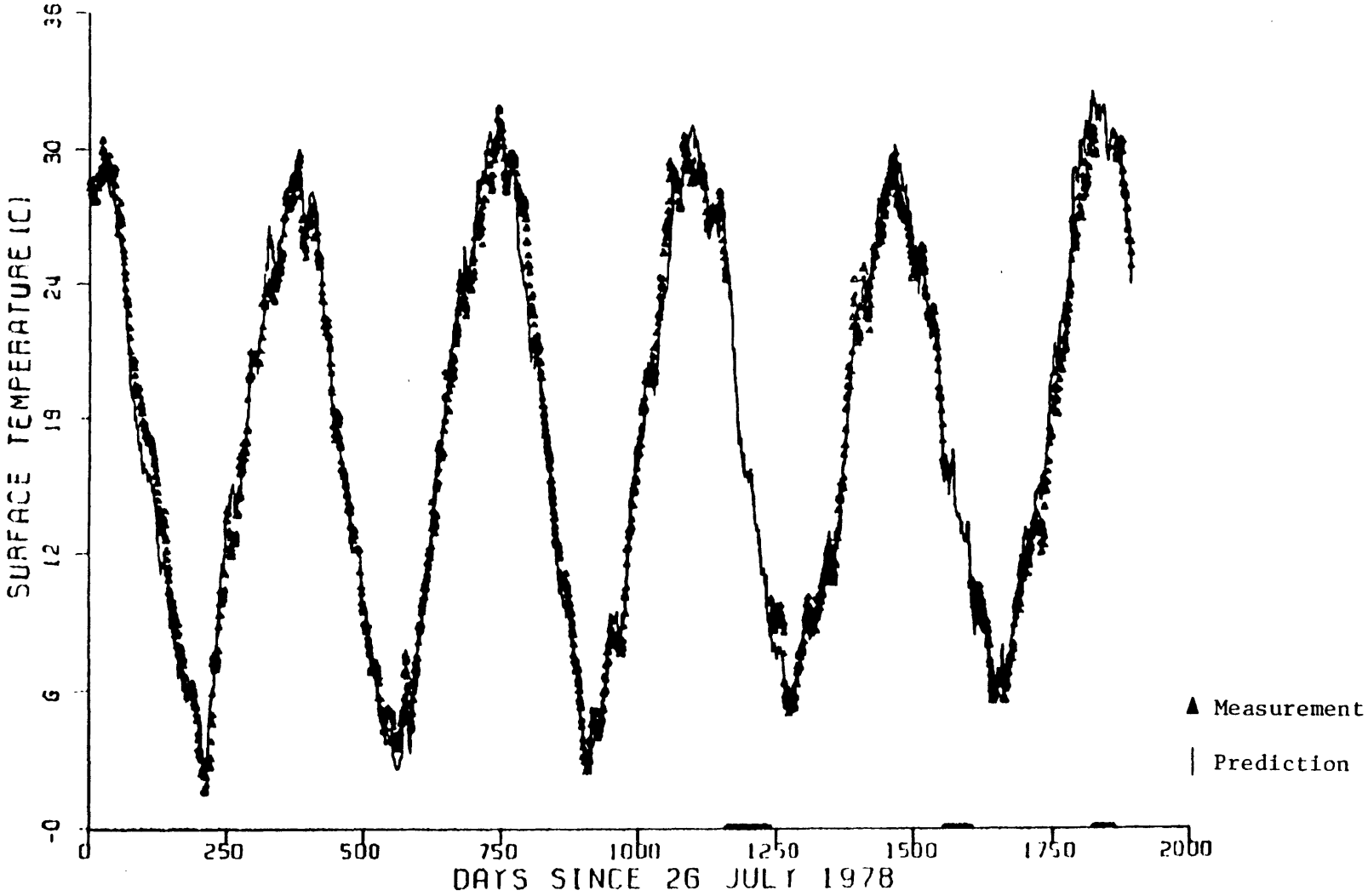

Figure 4.2c Measured vs. Predicted Surface Temperature at BR. PT.

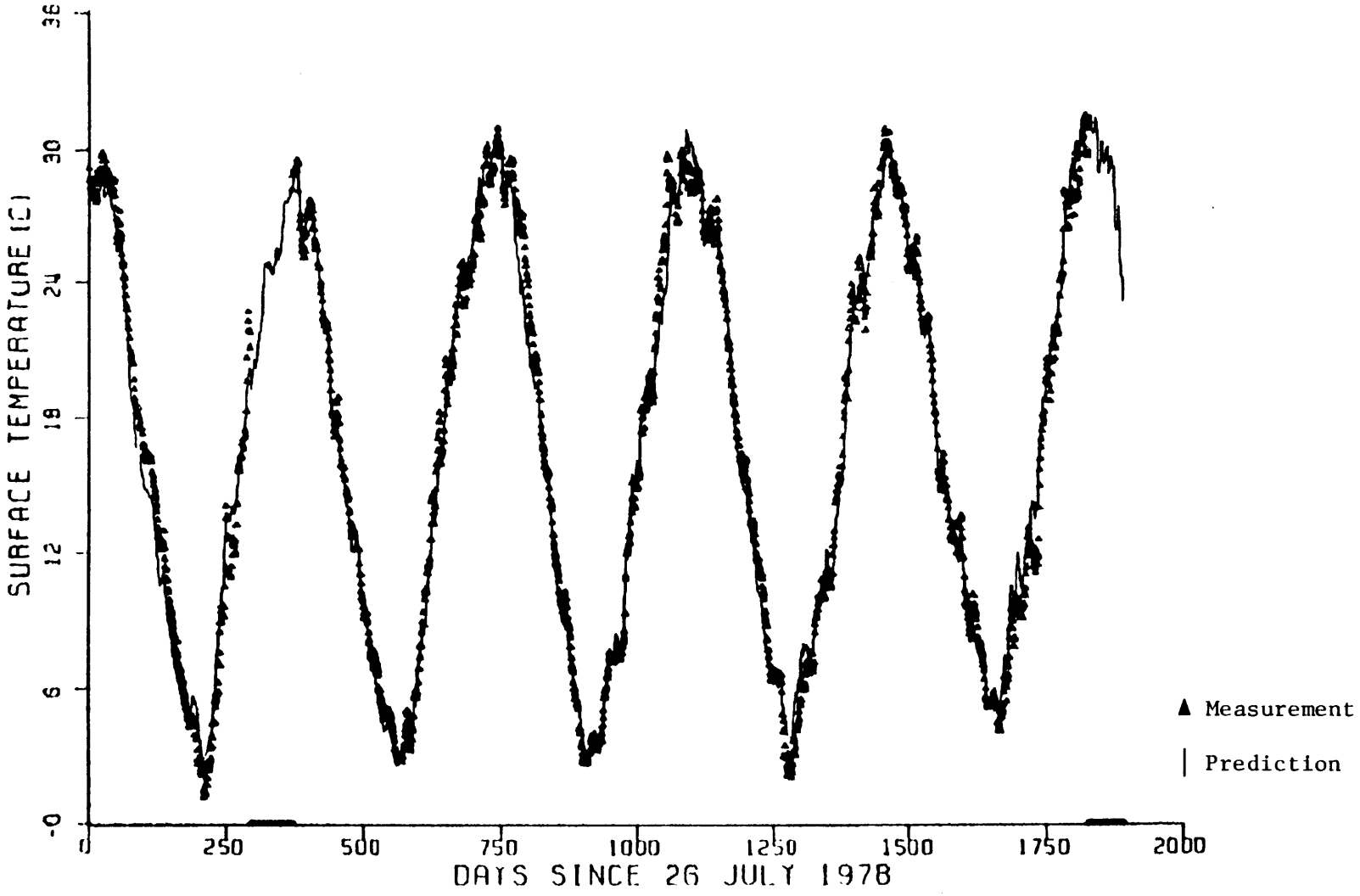

Figure 4.2d Measured vs. Predicted Surface Temperature at INTAKE

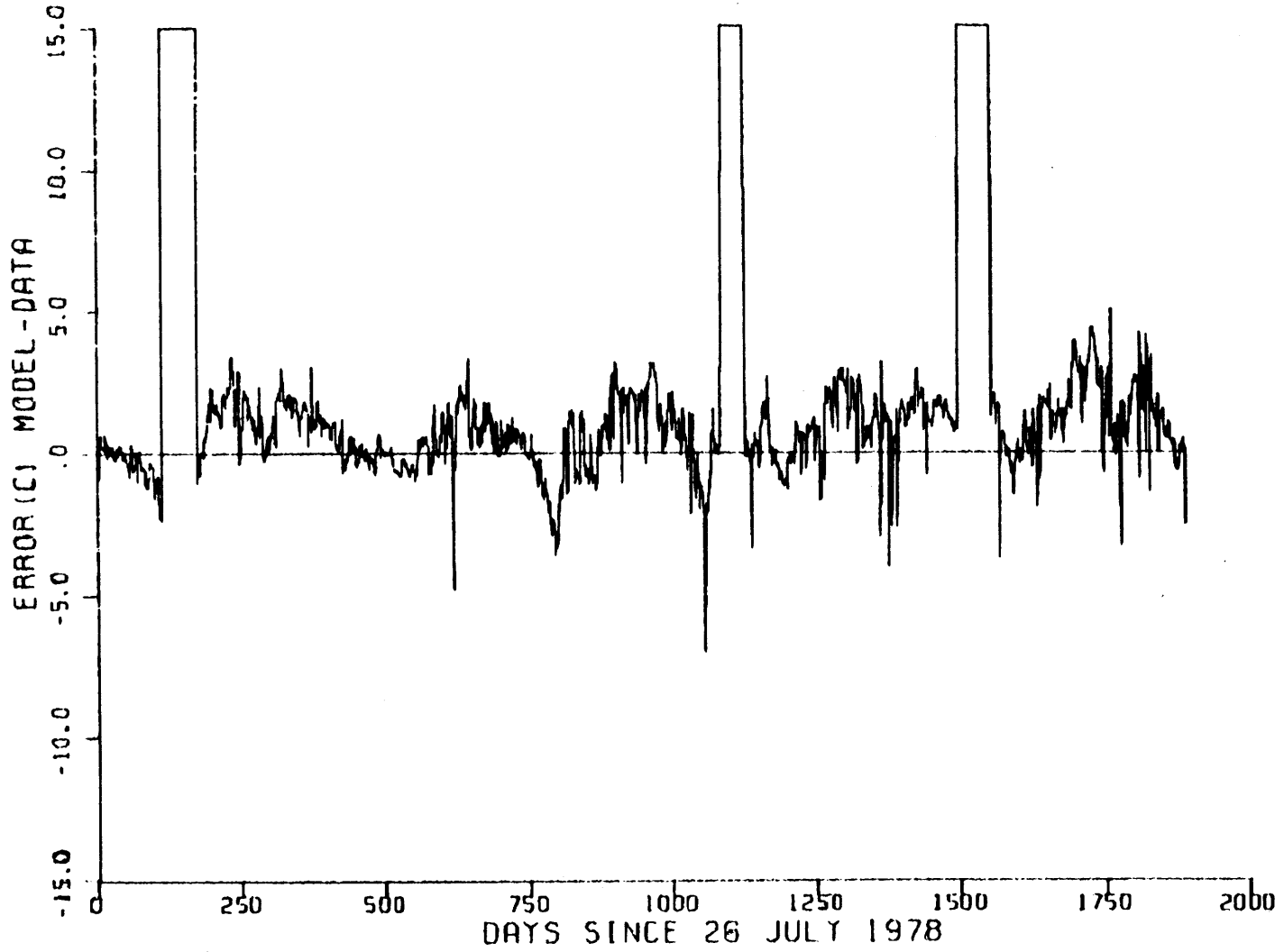

Figure 4.3a Raw Error at DISCHARGE

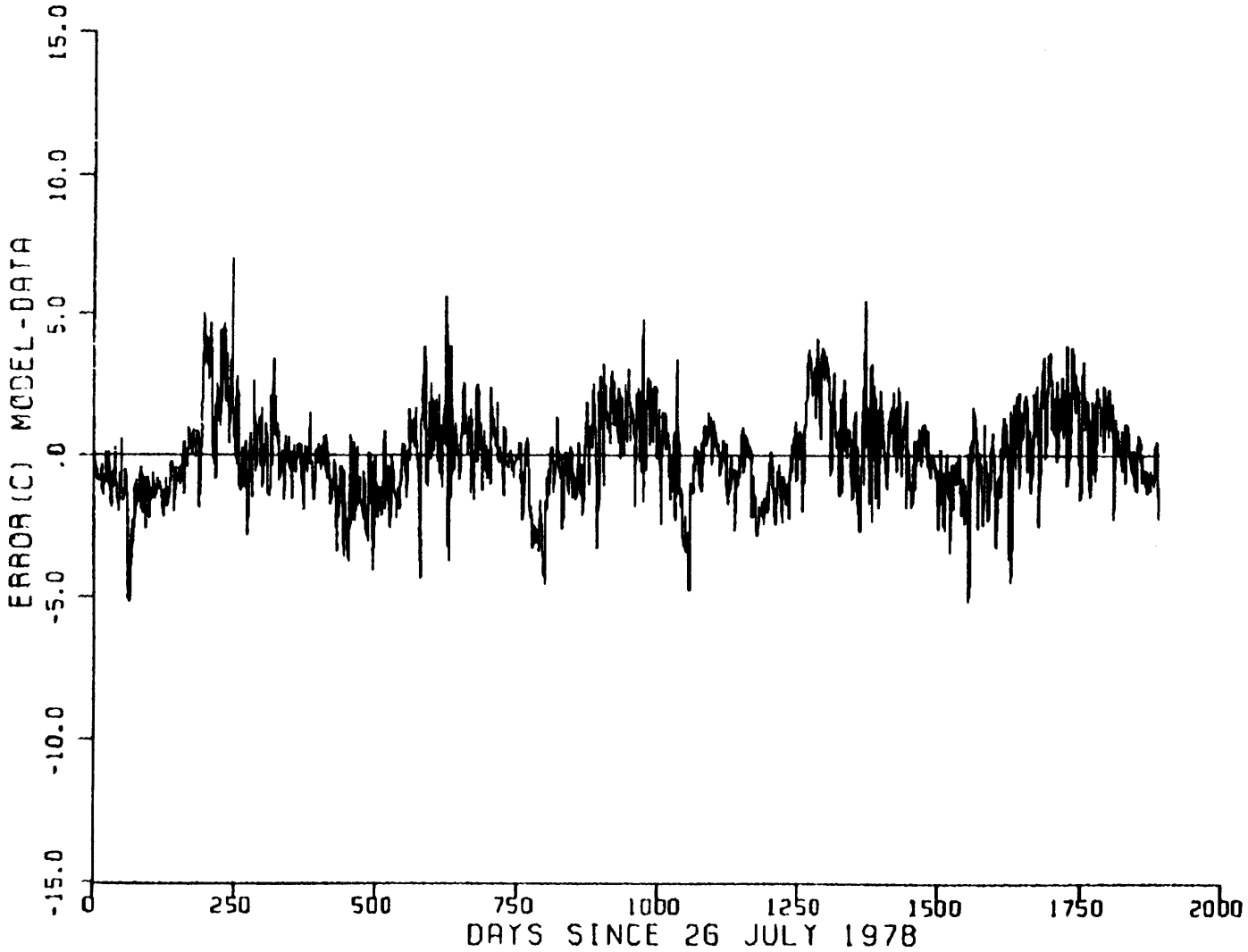

Figure 4.3b Raw Error at DIKE III

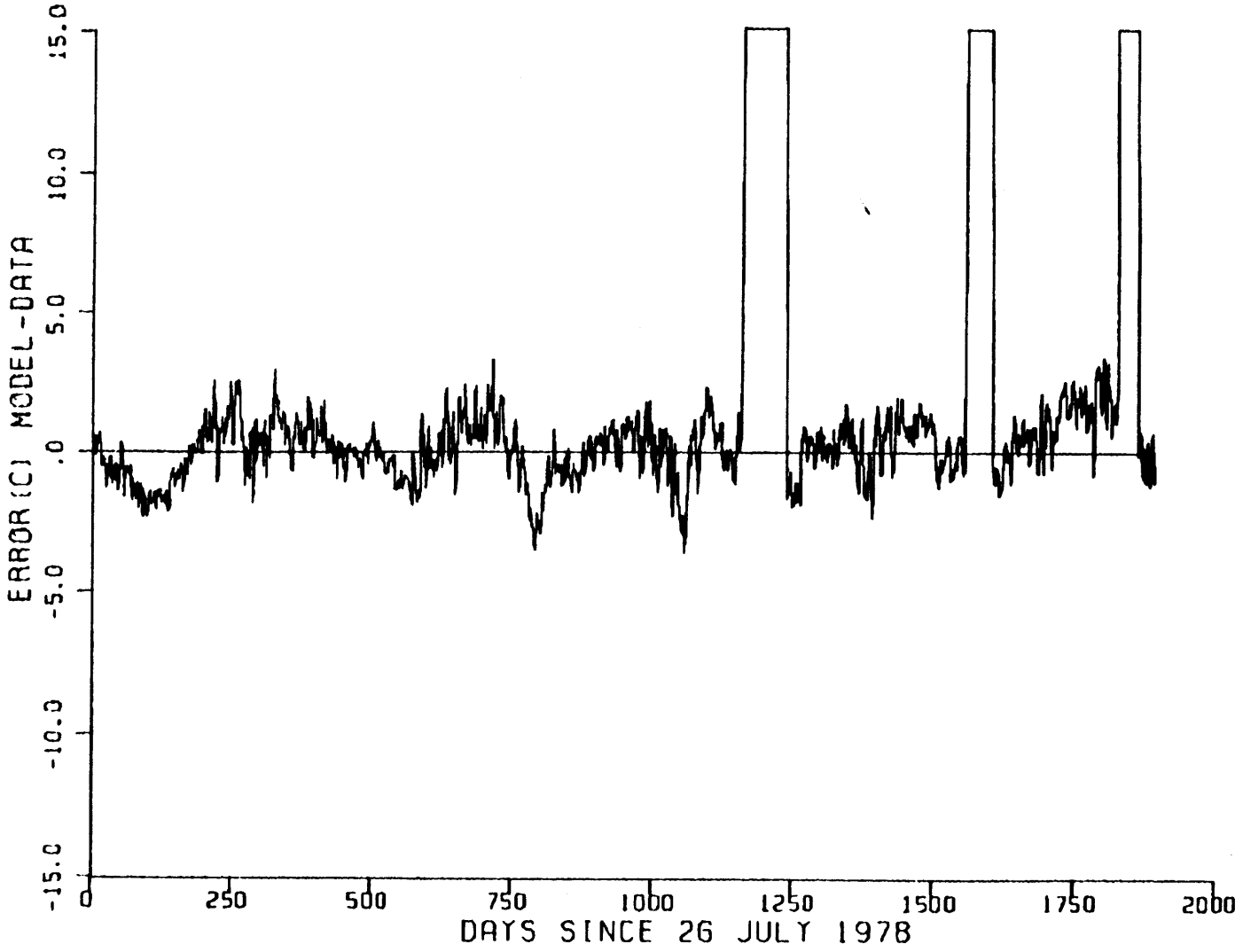

Figure 4.3c Raw Error at BR. PT.

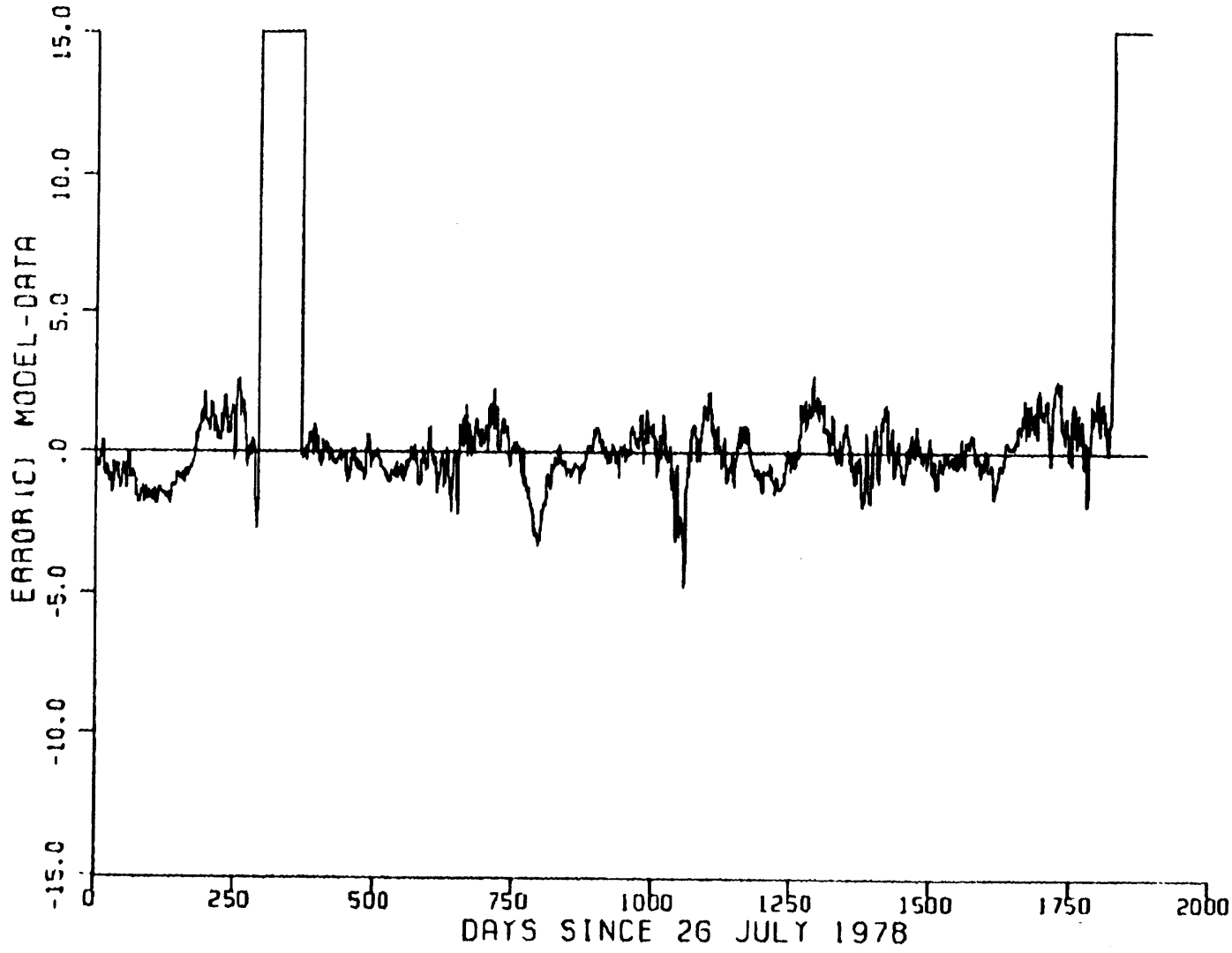

Figure 4.3d Raw Error at INTAKE

period with relatively large amplitude is observed at DIKE III, and the model is over-predicting at DISCHARGE most of the time. (Statistical data are provided in Section 4.4.)

4.3 Delta Error

Error analysis of the surface temperature can be done for individual points over the cooling lake system or for segments between the points. The former indicates how well the model is able to predict temperatures at specific locations, while the latter shows which segments of the cooling lake system are better modelled, and this information is useful for diagnosing individual model components. In the following analysis, the "delta" error over a segment is defined as the predicted temperature change over the segment minus the measured change. If the upstream control point is designated as i and the downstream point f, then the delta error for the segment is

$$\begin{aligned} \Delta T_{error} &= (T_{i_{model}} - T_{f_{model}}) - (T_{i_{data}} - T_{f_{data}}) \\ &= (T_{i_{model}} - T_{i_{data}}) - (T_{f_{model}} - T_{f_{data}}) \\ &= \text{raw error at i - raw error at f} \end{aligned} \qquad (4.1)$$

The following table is constructed to enhance clarity.

Table 4.1 Interpretation of Delta Errors

Raw Error at	-	Raw Error at	=	Delta Error across
INTAKE		DISCHARGE		Plant Condenser
DISCHARGE		DIKE III		WHTF
DIKE III		BR.PT.		Dike III Mixing
BR.PT.		INTAKE		Main Lake

Figures 4.4a to 4.4d show the "delta" errors associated with the above four segments of the cooling lake system. (Note that a positive error for all segments except across the plant condenser means that the model is cooling too much over that segment; however, a positive error for the segment across the plant condenser means that the model under-predicts the temperature rise due to waste heat rejected to the condenser cooling water.) The four "delta" error plots show that the WHTF and DIKE III Mixing are in general modelled with least accuracy, which can be inferred by the relatively poor performance of the model at DIKE III (see Figure 4.3b). It is also noticed that the model consistently over-predicts the temperature rise across the plant condenser.

4.4 Error Statistics

Statistics of the raw errors at the four diagnostic control points are given in Table 4.2. DIKE III shows the greatest variance but the least mean error, and the model is over-predicting by an average of 0.7 °C at DISCHARGE. Both BR.PT. and INTAKE show reasonably small mean raw errors and standard deviations.

Statistics for the first three years of simulation are reproduced from p. 165 of Wells et al. (1982) in Table 4.3. Comparison between the two tables shows that there is no major change in performance of the model associated with the two additional years of simulation.

In order to more effectively analyze the surface temperature prediction errors, monthly averages of the raw errors at the four diagnostic control points are compiled in addition to overall averages for the 5-year simulation period. This is done by lumping together the

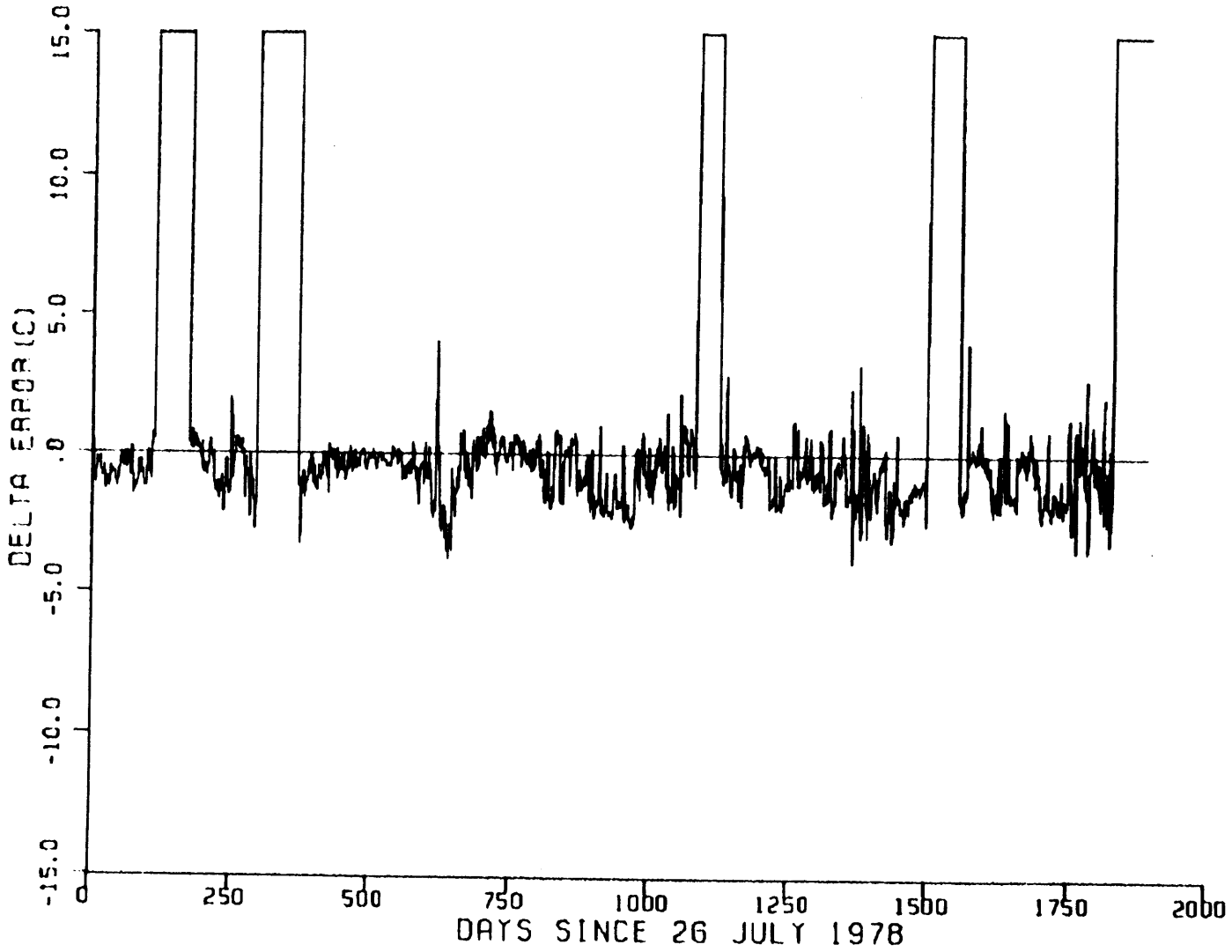

Figure 4.4a Delta Error across Plant Condenser

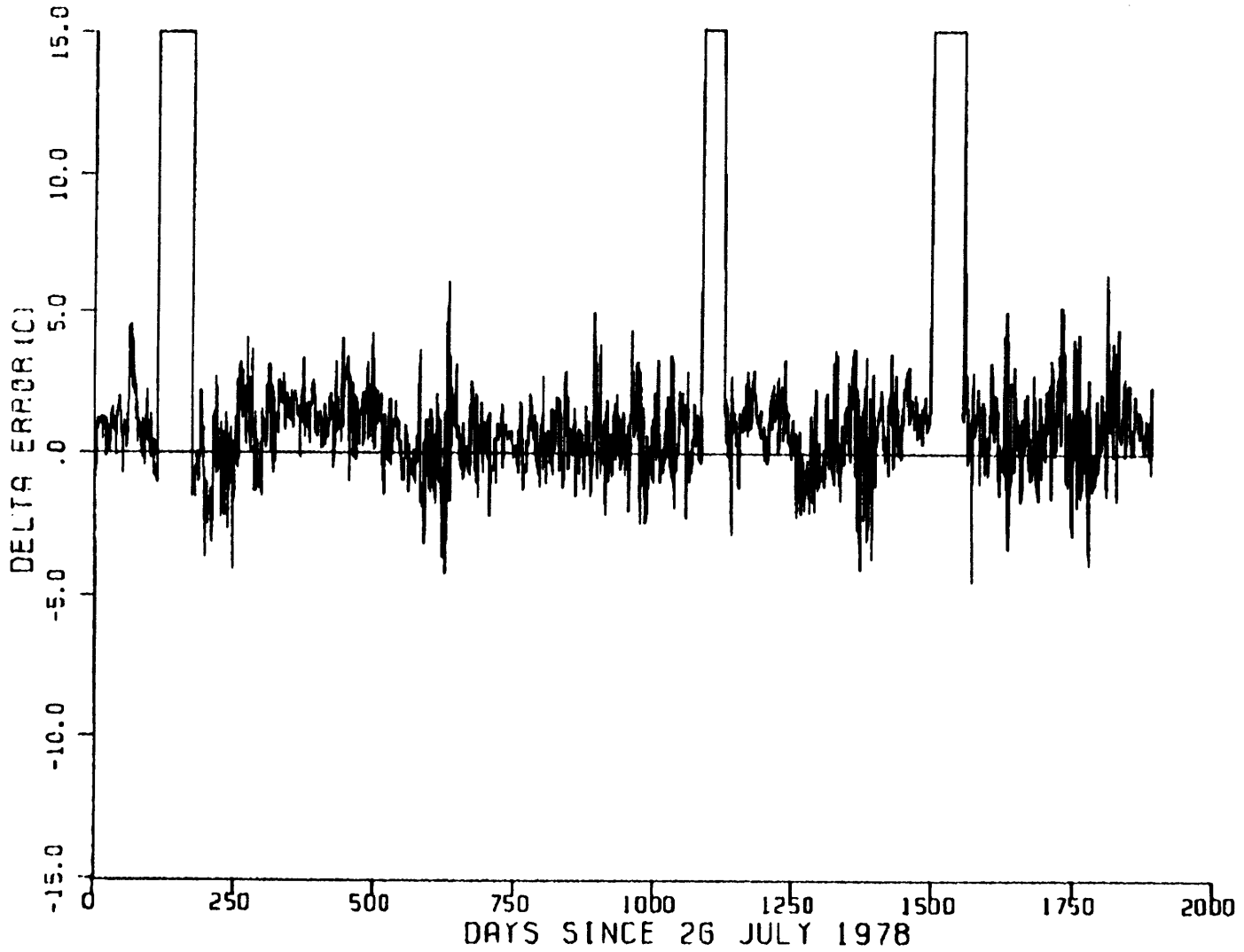

Figure 4.4b Delta Error across WMTF

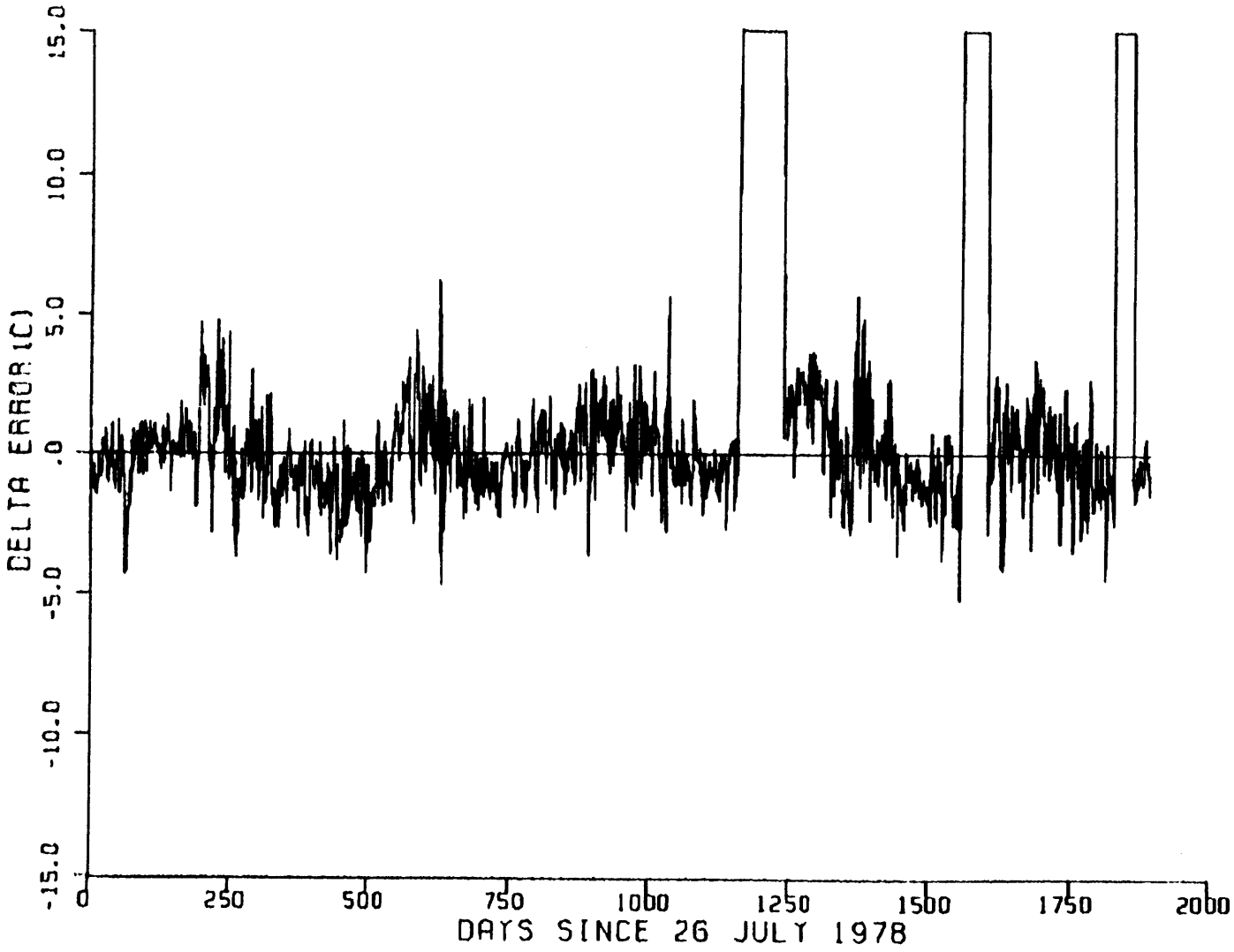

Figure 4.4c Delta Error across DIKE III Mixing

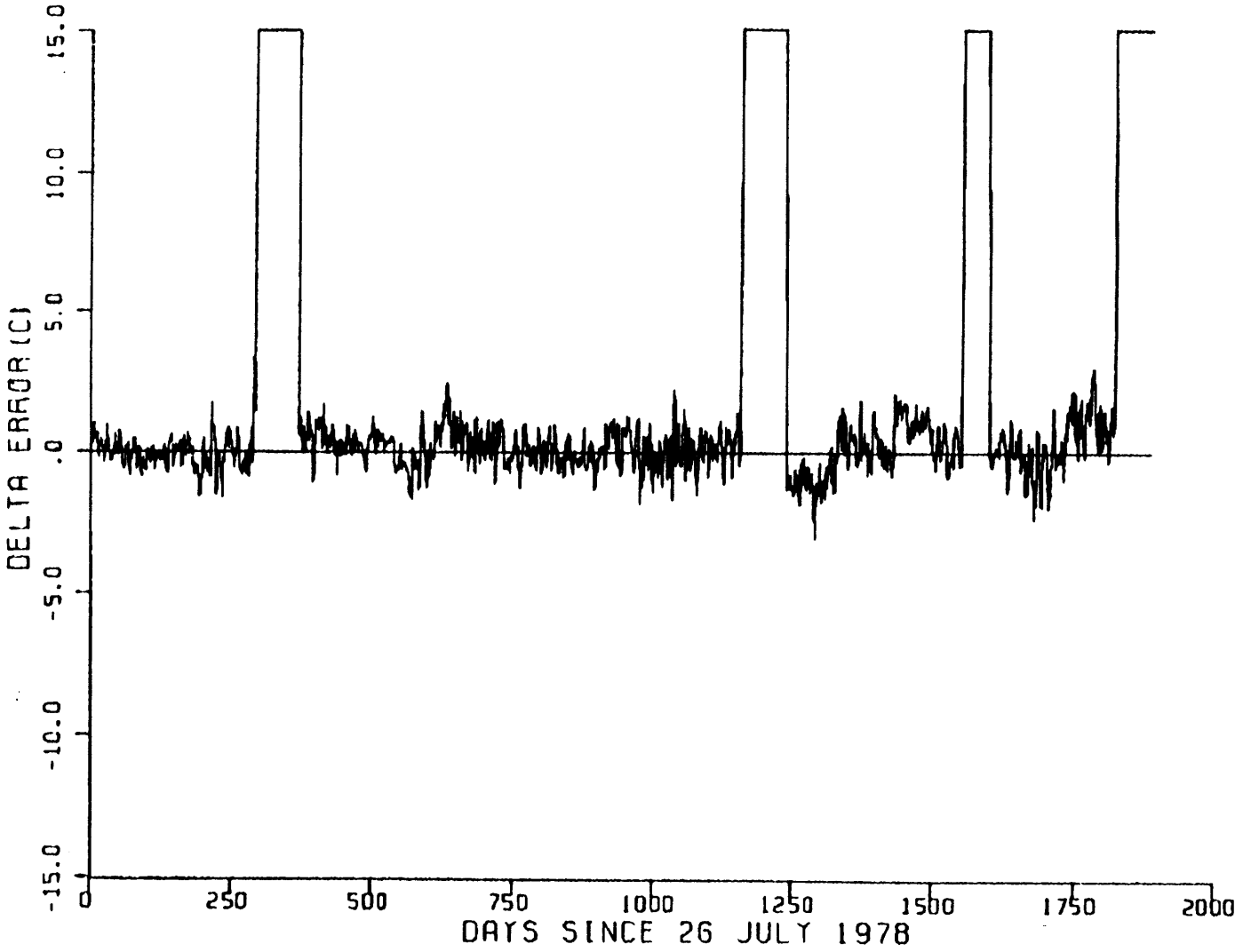

Figure 4.4d Delta Error across Main Lake

Table 4.2 Statistics of Raw Errors at Four Diagnostic Control Points (1978-1983)

	Mean (°C)	Standard Deviation (°C)	Sample Size (Day)
DISCHARGE	0.69	1.23	1633
DIKE III	-0.03	1.54	1893
BR. PT.	0.11	1.10	1733
INTAKE	-0.06	0.98	1752

Table 4.3 Statistics of Raw Errors at Four Diagnostic Control Points (1978-1981)

	Mean (°C)	Standard Deviation (°C)
DISCHARGE	0.48	1.27
DIKE III	-0.11	1.56
BR. PT.	-0.04	1.13
INTAKE	-0.22	1.02

monthly-averaged raw errors for a particular month for five years. The results are listed in Table 4.4. The number of months of data from which the average of a particular month is calculated is specified in the footnotes. The values in Table 4.4 are plotted in Figure 4.5 for each of the control points. Figure 4.5a shows that the raw error is predominantly positive (i.e., prediction > measurement) throughout the year at DISCHARGE. Figure 4.5b resembles a sine curve indicating that the raw error at DIKE III is largely periodic. It is also noted that the model over-predicts from January to July and under-predicts from August to December at that station. Figures 4.5c and d show that the model basically over-predicts from February to August and under-predicts from September to January at BR.PT. and INTAKE. Weak annual periodicity is observed and the monthly averages of the raw errors are bounded by ± 1°C at both stations.

4.5 Spectral Analysis

In many cases more insight is obtained by viewing results in the frequency domain; hence the method of spectral analysis is invoked in the surface temperature error analysis. The time series of raw errors at the four diagnostic control points are treated as stochastic processes. Stationarity of the stochastic processes is assumed, i.e., if $f(t) = \{x_{t_1}, x_{t_2}, \ldots x_{t_n}\}$ represents the raw error time series at a particular diagnostic control point, then we say that f(t) is stationary in the strict sense if the stochastic variables

$$x_{t_1}, x_{t_2}, x_{t_3}, \ldots x_{t_m}$$

Table 4.4 Monthly Averages* of Raw Errors at Four Diagnostic Control Points

Month	DISCHARGE	DIKE III	BR. PT.	INTAKE
JAN	0.81[4]	0.52	-0.21	0.00
FEB	1.37	1.41	0.15	0.61
MAR	1.67	1.32	0.46	0.59
APR	1.53	0.64	0.63	0.44
MAY	0.78	0.46	0.43	-0.02[4]
JUN	0.80	0.11	0.56	-0.04[4]
JUL	1.38[4]	0.16	0.92[4]	0.52[3]
AUG	0.59[4]	-0.28[6]	0.38	0.02
SEP	-0.24	-1.20[6]	-0.48	-0.72
OCT	-0.22[4]	-1.43	-0.96[3]	-0.65
NOV	-0.01[4]	-1.01	-0.87[3]	-0.63
DEC	-0.13[4]	-0.65	-0.54[3]	-0.64

---

* all are five-year averages except as specified

[6] six-year average

[4] four-year average

[3] three year average

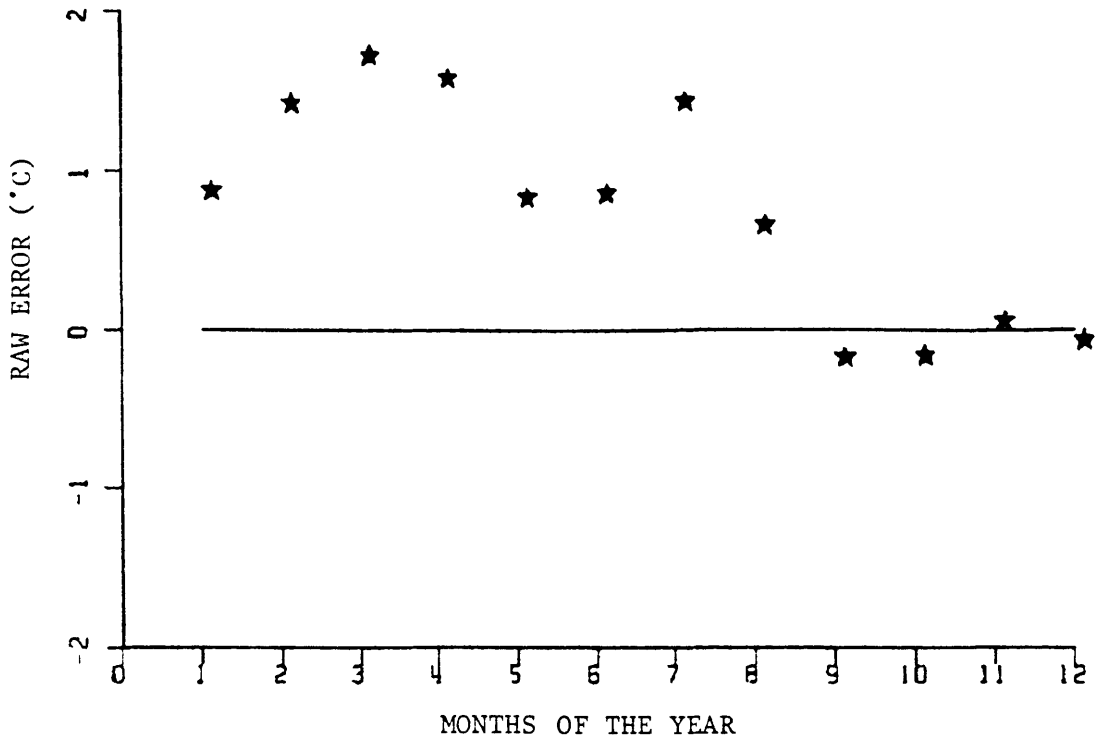

a. DISCHARGE

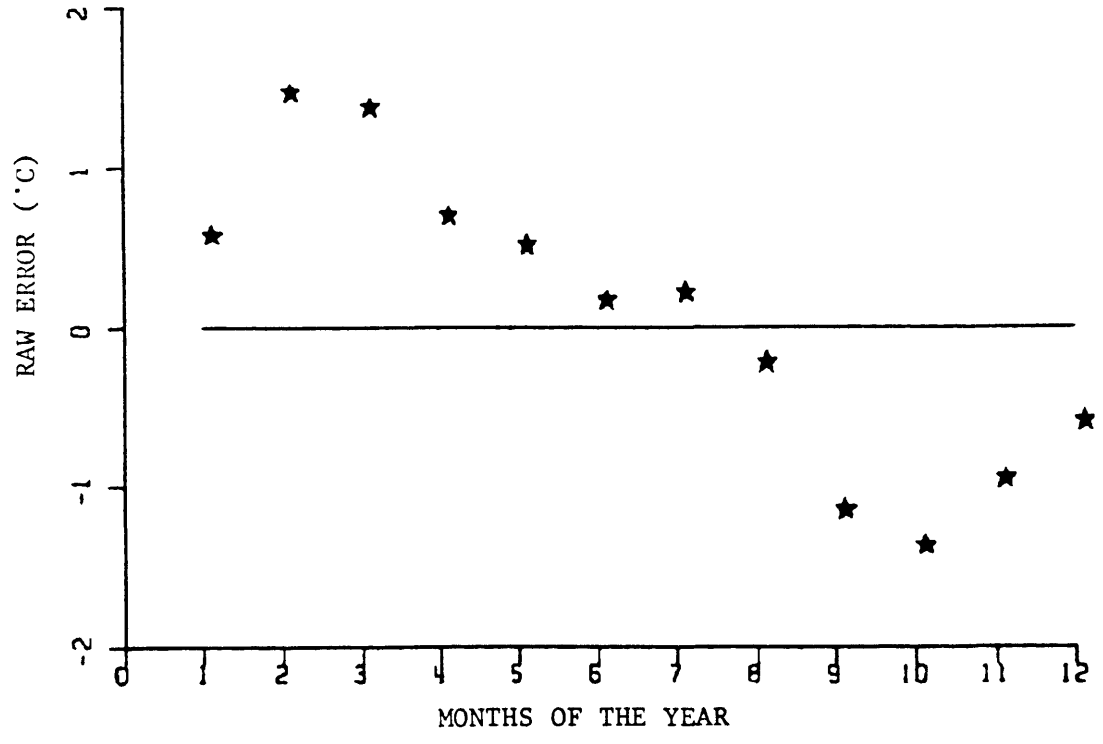

b. DIKE III

Figure 4.5 Monthly Averages of Raw Errors at Four Diagnostic Control Points

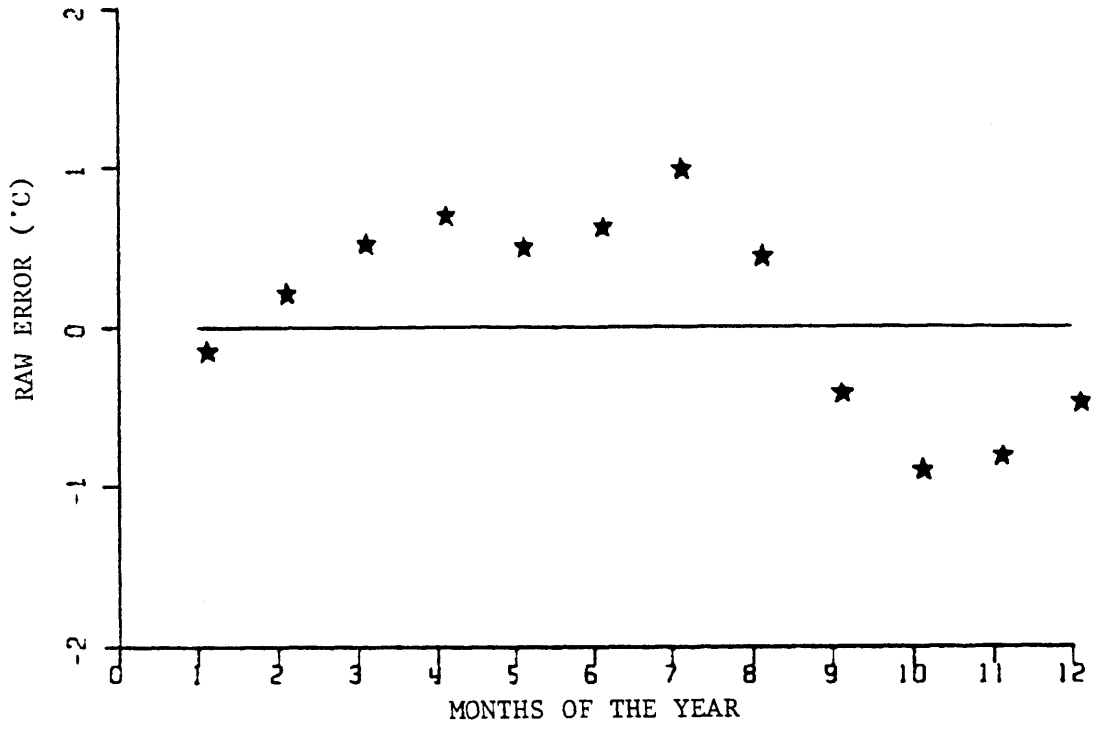

c. BURRUS POINT

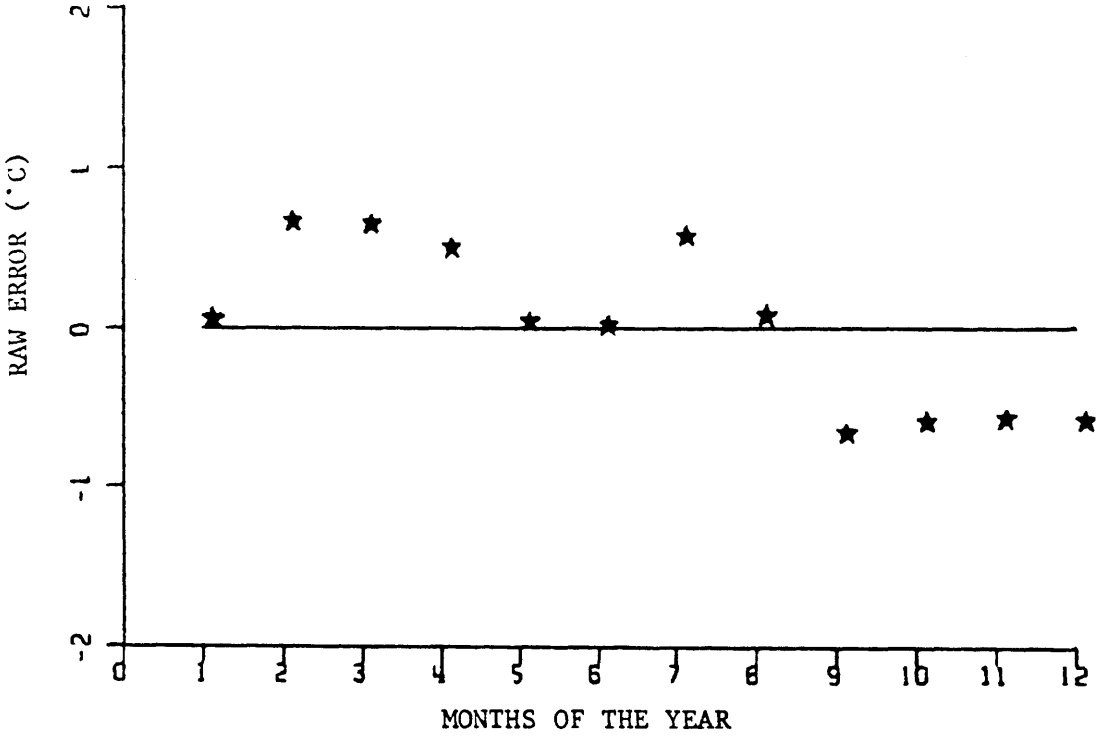

d. INTAKE

Figure 4.5 Monthly Averages of Raw Errors at Four Diagnostic Control Points (cont'd)

have the same joint probability distribution as the variables

$$x_{t_1+\tau},\ x_{t_2+\tau},\ x_{t_3+\tau} \ldots x_{t_m+\tau}$$

for all m, t_1, t_2,...t_m and every τ (Grenander, 1957). (N.B., the analogous spatial property for stationarity is homogeneity.) And if we define the autocovariance of f(t) as

$$R_{ff} \equiv \mathrm{Cov}(f(t+\tau),\ f(t))$$

$$= E[f(t+\tau)f(t)] \qquad (4.2)$$

where Cov = covariance,

E = expected value,

τ = lag time,

the assumption of stationarity in f(t) will assure that R_{ff} is a function of τ and τ alone.

The Fourier transform of R_{ff} gives the corresponding power spectral density (or power spectrum), $S(\omega)$, such that

$$S(\omega) = \frac{1}{2\pi} \int_{-\infty}^{\infty} e^{-i\omega\tau} R_{ff}(\tau)\, d\tau \qquad (4.3)$$

$$R_{ff}(\tau) = \int_{-\infty}^{\infty} e^{i\omega\tau} S(\omega)\, d\omega \qquad (4.4)$$

Fourier transforms of the autocovariances of the raw errors at the four diagnostic control points are computed and Figure 4.6 presents

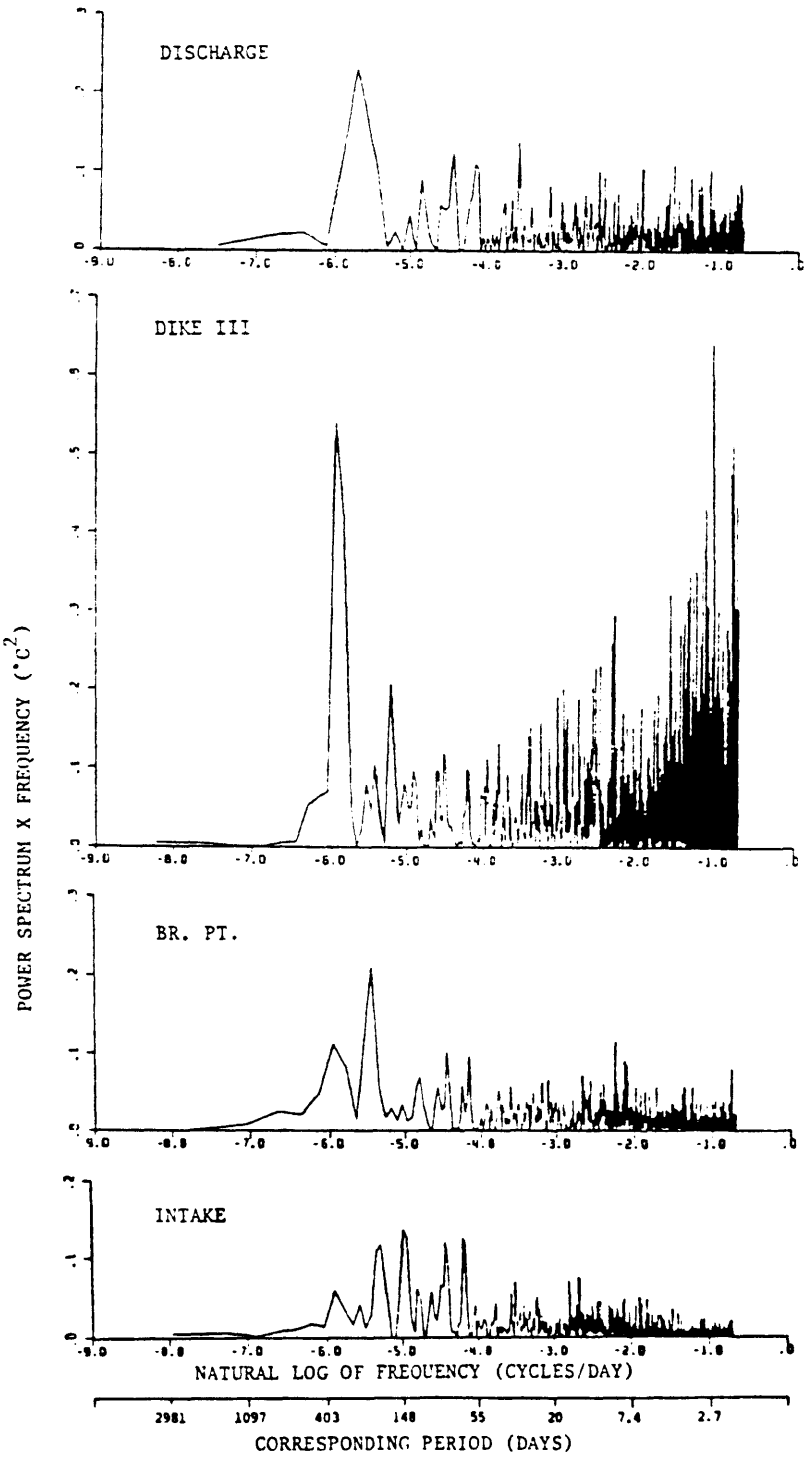

Figure 4.6 Power Spectra at Four Diagnostic Control Points

estimates of their corresponding power spectra. Note that the product between frequency and spectrum is plotted against natural log of frequency so that the "area under the curve" between two frequencies is proportional to the variance. This is because

$$\sigma^2(\Delta f) = \int_f^{f+\Delta f} S(\omega)\, d\omega$$

$$= \int_f^{f+\Delta f} \omega\, S(\omega)\, d \ln \omega \qquad (4.5)$$

where σ^2 = variance and Δf = window. In other words, variance of the raw error is represented by the total area under the curve.

Since the raw error time series are interrupted by gaps of missing measurement data, only the longest segment of continuous data is used for each control point. The lengths and starting dates of the time series used in computing the Fourier transforms are listed in Table 4.5.

Essentially a power spectrum shows how the variance or average power of the time series is distributed over frequency. Among the four control points, only DIKE III shows a strong and distinct peak at exactly the annual frequency (corresponds to ln (-5.9 cycles per day)). The rest of the diagnostic control points show a more evenly distributed variance over the frequencies ranging from about half a cycle per year to six cycles per year. This analysis confirms the observations made from Figures 4.3a through d that the raw error at DIKE III is periodic at predominantly the annual frequency whereas the

Table 4.5 Length and Starting Day of Time Series Used in Computing the Fourier Transforms

	Length of Time Series (Day)	Starting Day of Time Series (Days Since 26 July 1978)
DISCHARGE	911	174
DIKE III	1893	1
BR. PT.	1160	1
INTAKE	1458	371

rest of the control points show mild periodicities over the periods ranging from two months to two years.

4.6 Summary of Analysis

The State of Virginia experienced a hot summer in 1983. Meteorological records at Richmond showed that the monthly-averaged temperatures for June, July and August were about 0.8 °C above the long-term normals based on records for the 1941-1970 period (Local Climatological Data, Richmond, VA). North Anna Power Station operated at full capacity of two units for more than ninety days within the four-month period of June to September, providing the first experience with essentially two-unit summer operations. (Figures 4.7 and 4.8 show the number of nuclear units and number of pumps operating, respectively, during the period of model simulation.) Analysis in the previous sections indicates that the model shows a consistent performance even under "harsh" climatic and plant operation conditions.

Raw error analysis of the surface temperature shows that the model over-predicts in the months of January through July and under-predicts in August through December at DIKE III with an amplitude of about 1.5°C and a mean raw error near zero. For the rest of the diagnostic control points (INTAKE, BR.PT. and DISCHARGE), the raw error is occuring quite randomly in time with mild annual periodicity. The above observations are confirmed by error statistics and spectral analysis which show that the raw error at DIKE III is periodic at predominantly the annual frequency whereas the rest of the control points show mild periodicities over the periods ranging from two months to two years.

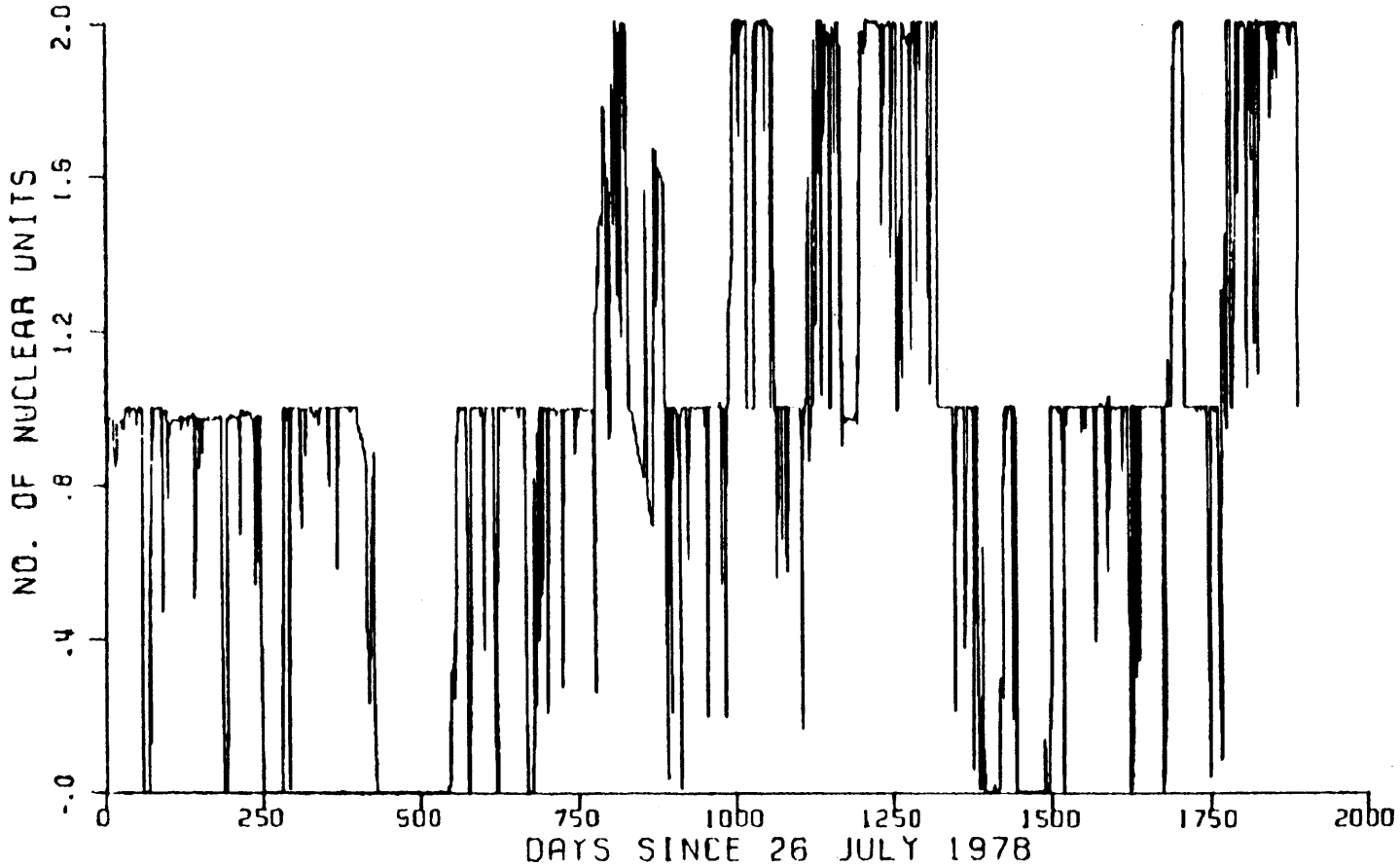

Figure 4.7 Number of Nuclear Units Operating During Simulation Period

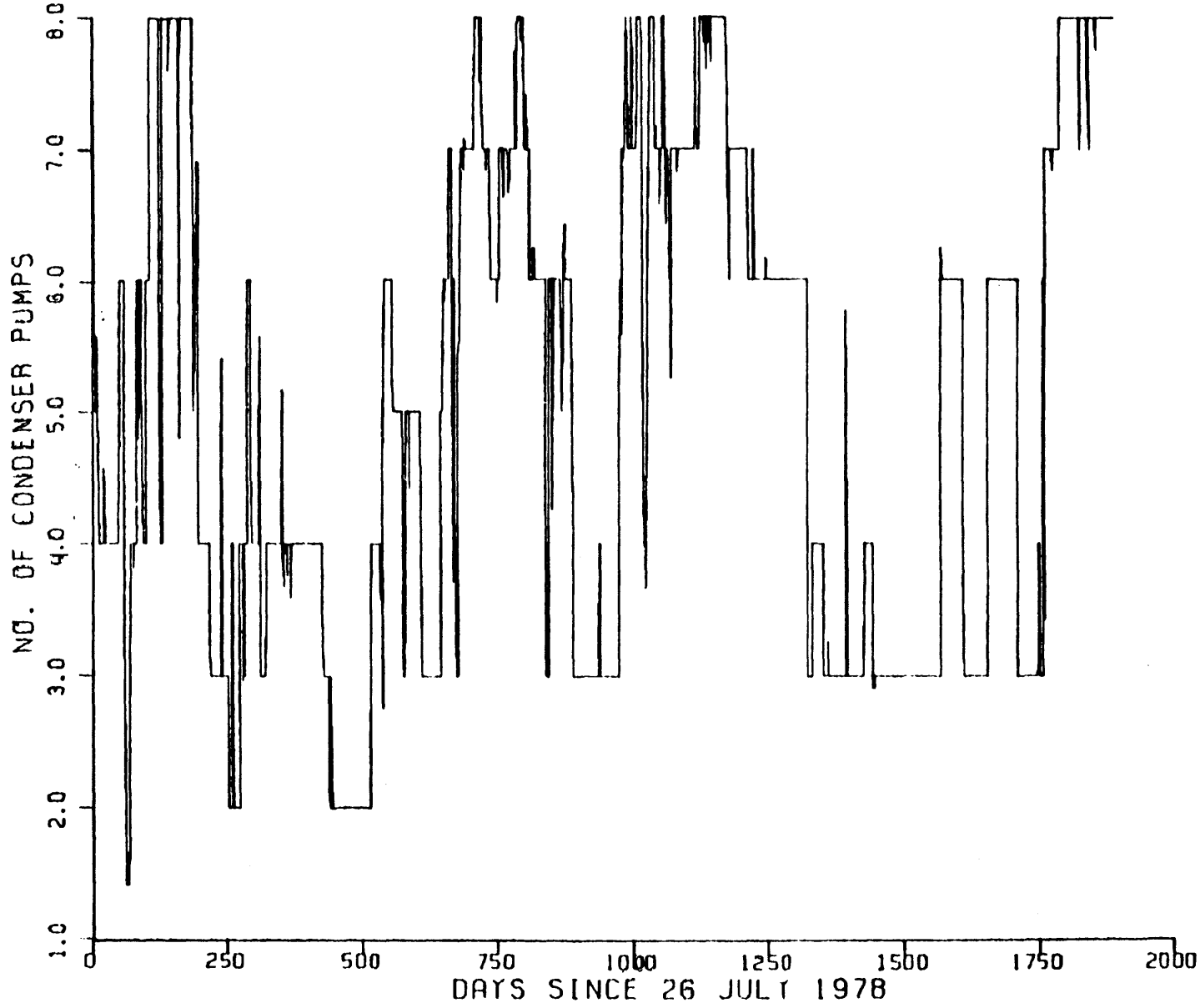

Figure 4.8 Number of Circulating Pumps Operating During Simulation Period

(Each pump corresponds to a flow rate of 15 m^3s^{-1})

"Delta" error analysis shows that the model consistently over-predicts the temperature rise across the plant condenser by about 0.7 °C.

5. MODEL RECALIBRATION

5.1 Introduction

Analysis of prediction errors in Chapter 4 shows that the model is relatively weak in predicting surface temperatures at two of the diagnostic control points, namely, DIKE III and DISCHARGE. Recalibration of the model aiming at improving the goodness-of-fit of the five years of measurement data at these two locations is presented in this chapter.

Transient error characterized by periodicity of the raw error at a distinct annual frequency is recognized at DIKE III. Section 5.2 deals with transient errors through a discussion of potential errors in (1) surface heat transfer and (2) system response of the cooling pond model.

Steady state error at DISCHARGE is characterized by an over-prediction of the surface temperature by an average of about 0.7°C. Given the fact that predictions at DISCHARGE should have minimal dependence on the hydraulics of the model or on the meteorological conditions, it is probable that the raw error is caused by uncertainty in the plant operation data. A sensitivity analysis of the raw error at DISCHARGE with respect to moderate changes in the plant operation data is given in Section 5.3.

5.2 Transient Errors at DIKE III

5.2.1 General Discussion

Periodicity of the raw error at DIKE III (see Figure 4.3b) can be looked at as the result of small differences in the highly periodic measurements and model predictions (see Figure 4.2b). Thus, if we let

$$E(t) = P(t) - M(t) \tag{5.1}$$

where E(t), P(t) and M(t) represent the raw error, prediction and measurement time series, respectivly, and if we fit a periodic function to P(t) and M(t) such that

$$P(t) = P^* \sin(\omega t + \phi_p) + \varepsilon_p(t) \tag{5.2}$$

$$M(t) = M^* \sin(\omega t + \phi_m) + \varepsilon_m(t) \tag{5.3}$$

where

P^*, M^* = amplitudes of periodic functions corresponding to P(t), M(t), respectively,

ϕ_p, ϕ_m = respective phases,

$\varepsilon_p, \varepsilon_m$ = remaining processes corresponding to P(t), M(t), respectively,

ω = $2\pi/T$; T = 365.25 days, and

t = Julian day of a year,

then, in general, the raw error can be caused by the fact that (1) $M^* \neq P^*$, or (2) $\phi_m \neq \phi_p$, or (3) some combinations of the above two. However, since the maximum raw errors do not occur during summer and winter (when both measurements and predictions are at their peaks), it is suspected that the raw error is caused more by (2) than by (1).

In order to confirm the above observation, harmonic analyses of the measurement and prediction time series are made.

Given any time series D(t), we can write

$$D(t) - C(t) = \varepsilon(t) \tag{5.4}$$

where C(t) is a periodic time series and $\varepsilon(t)$ is the remaining random process. If we let

$$C(t) = C^* \sin(\omega t + \phi) = A \sin \omega t + B \cos \omega t \tag{5.5}$$

where $\omega = 2\pi/T$ and T = period, then Eq. 5.4 becomes

$$D(t) = A \sin \omega t + B \cos \omega t + \varepsilon(t) \tag{5.6}$$

and, by direct integration,

$$\int_t^{t+nT} D(t) \sin\omega t \, dt = A \int_t^{t+nT} \sin^2\omega t \, dt + B \int_t^{t+nT} \sin\omega t \cos\omega t \, dt + \int_t^{t+nT} \varepsilon(t) \sin\omega t \, dt = \frac{Ant}{2} \tag{5.7}$$

where n = 1, 2, 3,... Similarly,

$$\int_t^{t+nT} D(t) \cos\omega t \, dt = \frac{Bnt}{2} \tag{5.8}$$

Thus, we have the following Fourier coefficients

$$A(\omega) = \frac{2}{nT} \int_t^{t+nT} D(t) \sin\omega t \, dt \tag{5.9}$$

$$B(\omega) = \frac{2}{nT} \int_{t}^{t+nT} D(t) \cos\omega t \, dt \qquad (5.10)$$

And, from Eq. 5.5, we have the following relationships among A,B and H,ϕ:

$$C^* \cos\phi = A \qquad (5.11)$$

$$C^* \sin\phi = B \qquad (5.12)$$

or

$$C^{*2} = A^2 + B^2 \qquad (5.13)$$

$$\phi = \tan^{-1}\left(\frac{B}{A}\right) \qquad (5.14)$$

where C^* and ϕ can be interpreted as the amplitude and phase, respectively, characterizing the time series D(t).

In accordance with the above discussion, the appropriate time series are decomposed by computing the Fourier coefficients A and B using Eqs. 5.9 and 5.10, where $\omega = 2\pi/T$, T = 365.25 days and n = 4. A period of exactly four years (Jan. 1, 1979 to Dec. 31, 1982) of the time series is analyzed. Notice that for purposes of this analysis, a model prediction time series, P(t), is used with α set to a constant value of 0.75. (N.B., a periodic function was previously used to adjust the evaporation formula used in the WHTF in the calibrated model (p. 74, Wells et al.) such that

$$\alpha = 0.75 + 0.15 \cos\left(\frac{2\pi t}{365.25} - 2.60\right) \qquad (5.15a)$$

or, equivalently,

$$\alpha = 0.75 + 0.15 \sin\left(\frac{2\pi t}{365.25} - 1.03\right) \qquad (5.15b)$$

where t = Julian day of the year and α = correction factor multiplying the evaporative heat flux.)

Results of the harmonic analysis for P(t), M(t) and E(t) are listed in Table 5.1 in terms of C^* and ϕ, which are computed from A and B using Eqs. 5.13 and 5.14. From Table 5.1 it is observed that the amplitudes P* and M* are almost identical, while their phases are different by $\Delta\phi = \phi_p - \phi_m = 0.0939$. Thus it can be safely concluded that periodicity of raw error at DIKE III at annual frequency is caused by the fact that the measurements are lagging behind predictions by $\Delta\phi = 0.0939$ which amounts to $\Delta\phi/2\pi \times 365.25 \simeq 5.5$ days along the time axis.

It is also observed from Table 5.1 that the raw error, E(t), is out-of-phase with the measurements and predictions by about $\pi/2$ (or 91 days), i.e., $\phi_e - (\phi_m + \phi_p)/2 \simeq 1.58 \simeq \pi/2$, which is consistent with the earlier qualitative observation that the greatest raw errors occured in spring and autumn and with the fact that the amplitudes P* and M* are almost equal. Regarding the latter point (refer to Fig. 5.1), Eq. 5.1 may be rewritten in terms of Eqs. 5.2 and 5.3 as

$$E(t) = P^* \sin(\omega t + \phi_p) - M^* \sin(\omega t + \phi_p) + \varepsilon(t) \qquad (5.16)$$

where $\varepsilon(t) = \varepsilon_p(t) - \varepsilon_m(t)$. Upon trigonometric expansion, Eq. 5.16 becomes

$$E(t) = \sin \omega t\left[P^*\cos\phi_p - M^* \cos\phi_m\right] + \cos \omega t\left[P^*\sin\phi_p - M^* \sin\phi_m\right] + \varepsilon(t) \qquad (5.17)$$

Table 5.1 Fourier Decomposition of Time Series

Description of Time Series D(t)	C^* (°C)	ϕ (radian)	ϕ (Julian Day)
Measurements at DIKE III [= M(t)]	11.687 (=M*)	-2.0793 ($=\phi_m$)	-120.9
Predictions at DIKE III with α = 0.75 [= P(t)]	11.683 (=P*)	-1.9854 ($=\phi_p$)	-115.4
Raw Errors at DIKE III with α = 0.75 [= E(t) = P(t) - M(t)]	1.096 (=E*)	-0.4576 ($=\phi_e$)	-26.6

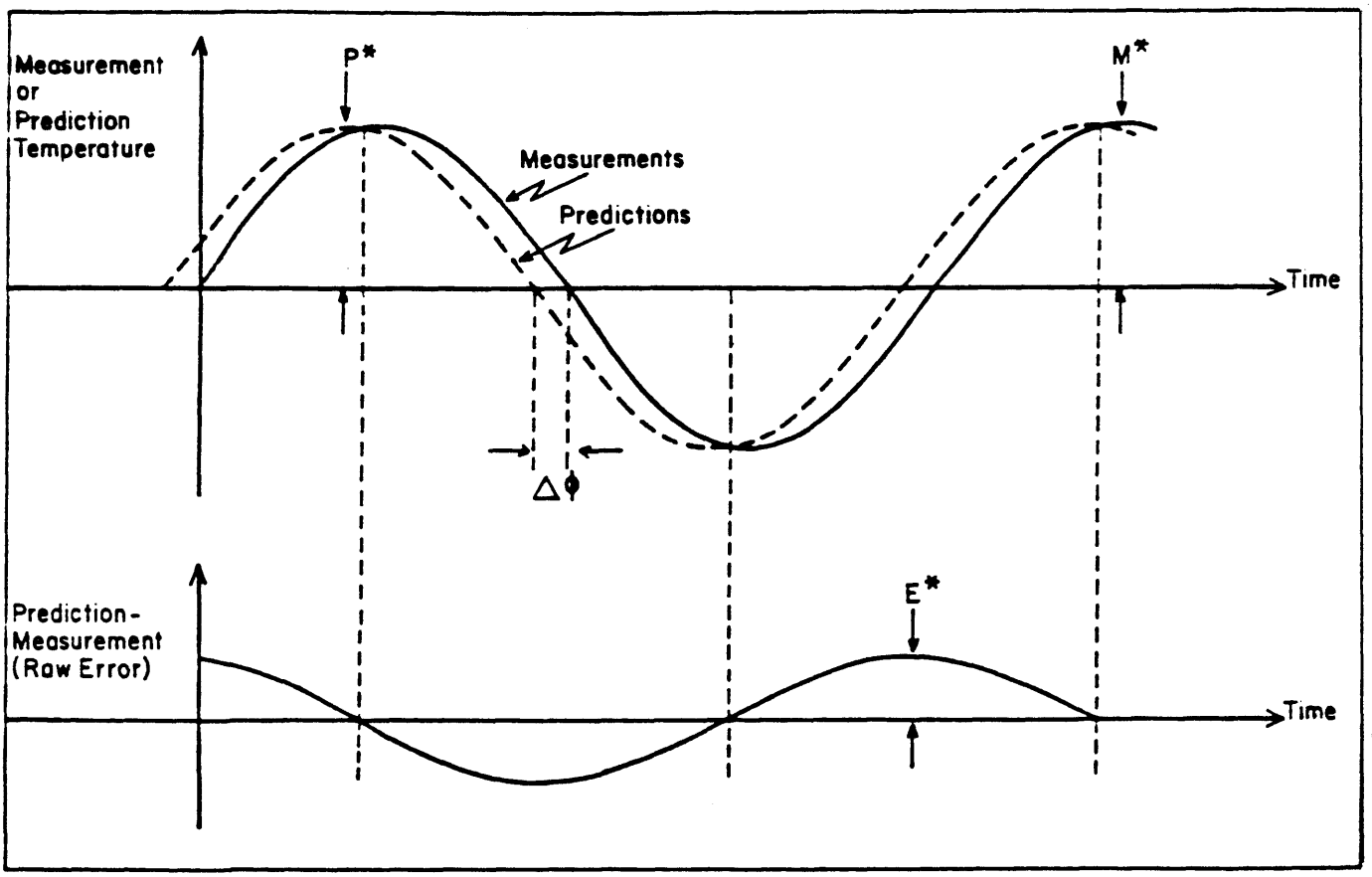

Figure 5.1 Schematic of Relationships between Measurements, Predictions and Raw Errors at DIKE III

If we let

$$A = P^* \cos\phi_p - M^* \cos\phi_m \qquad \text{and}$$

$$B = P^* \sin\phi_p - M^* \sin\phi_m \tag{5.18}$$

then Eq. 5.17 becomes

$$E(t) = A \sin\omega t + B \cos\omega t + \varepsilon(t) \tag{5.19}$$

which has the identical form as Eq. 5.6. Letting

$$E^* \sin(\omega t + \phi_e) = A \sin\omega t + B \cos\omega t \tag{5.20}$$

it follows that

$$(E^*)^2 = A^2 + B^2 \tag{5.21}$$

and

$$\phi_e = \tan^{-1}\left(\frac{B}{A}\right) \tag{5.22}$$

Now, since the harmonic analysis shows that $M^* = P^*$, putting Eq. 5.18 into Eqs. 5.21 and 5.22 will give, upon simplification,

$$(E^*)^2 = (M^*)^2[(\cos\phi_p - \cos\phi_m)^2 + (\sin\phi_p - \sin\phi_m)^2] \tag{5.23}$$

and

$$\phi_e = \tan^{-1}\left(\frac{\sin\phi_p - \sin\phi_m}{\cos\phi_p - \cos\phi_m}\right) \tag{5.24}$$

Defining $\phi_p = \phi_m + \Delta\phi$, we can rewrite Eq. 5.23 as

$$(E^*)^2 = (M^*)^2[(\cos\phi_m(\cos\Delta\phi - 1) - \sin\phi_m \sin\Delta\phi)^2 + (\sin\phi_m(\cos\Delta\phi - 1) + \cos\phi_m \sin\Delta\phi)^2] \tag{5.25}$$

which can be further simplified to give

$$(E^*)^2 \simeq (M^*)^2[(\sin\phi_m \sin\Delta\phi)^2 + (\cos\phi_m \sin\Delta\phi)^2] \tag{5.26}$$

or

$$(E^*)^2 \simeq (M^*)^2 \Delta\phi^2 \tag{5.27}$$

by recognizing that $\Delta\phi << 1$. (From Table 5.1, $\Delta\phi = \phi_p - \phi_m = 0.0939$.) Thus, we arrive at the following relationship

$$E^* \simeq M^* \Delta\phi \tag{5.28}$$

which simply says that the amplitude of raw errors is directly proportional to the phase error given that the amplitudes of prediction and measurement are equal. (This result is confirmed by the calculation: $11.687 \times 0.0939 = 1.097 \simeq 1.096$ where 11.687 and 1.096 are computed values of M* and E*, respectively. See Table 5.1.)

Eq. 5.24 can also be simplified to give

$$\phi_e \simeq \tan^{-1} (-\cot \phi_m) \tag{5.29}$$

by writing $\phi_p = \phi_m + \Delta\phi$ and realizing that $\Delta\phi << 1$; this result is equivalent to

$$\phi_e = \phi_m \pm \frac{\pi}{2} \tag{5.30}$$

which says that, as long as $\phi_p - \phi_m = \Delta\phi << 1$, and $M^* \simeq P^*$, ϕ_e will always be 90° out of phase with the measurement or prediction.

Two reasons can be postulated for the time lag between measurements and predictions: (1) the forcing function, as represented by the equilibrium temperature (T_e) is too high (thus causing maximum over-prediction) in spring and too low (causing maximum under-prediction) in autumn (Figure 5.2), or (2) the system response of the model is too quick. For each of these two general reasons, two possibilities are examined.

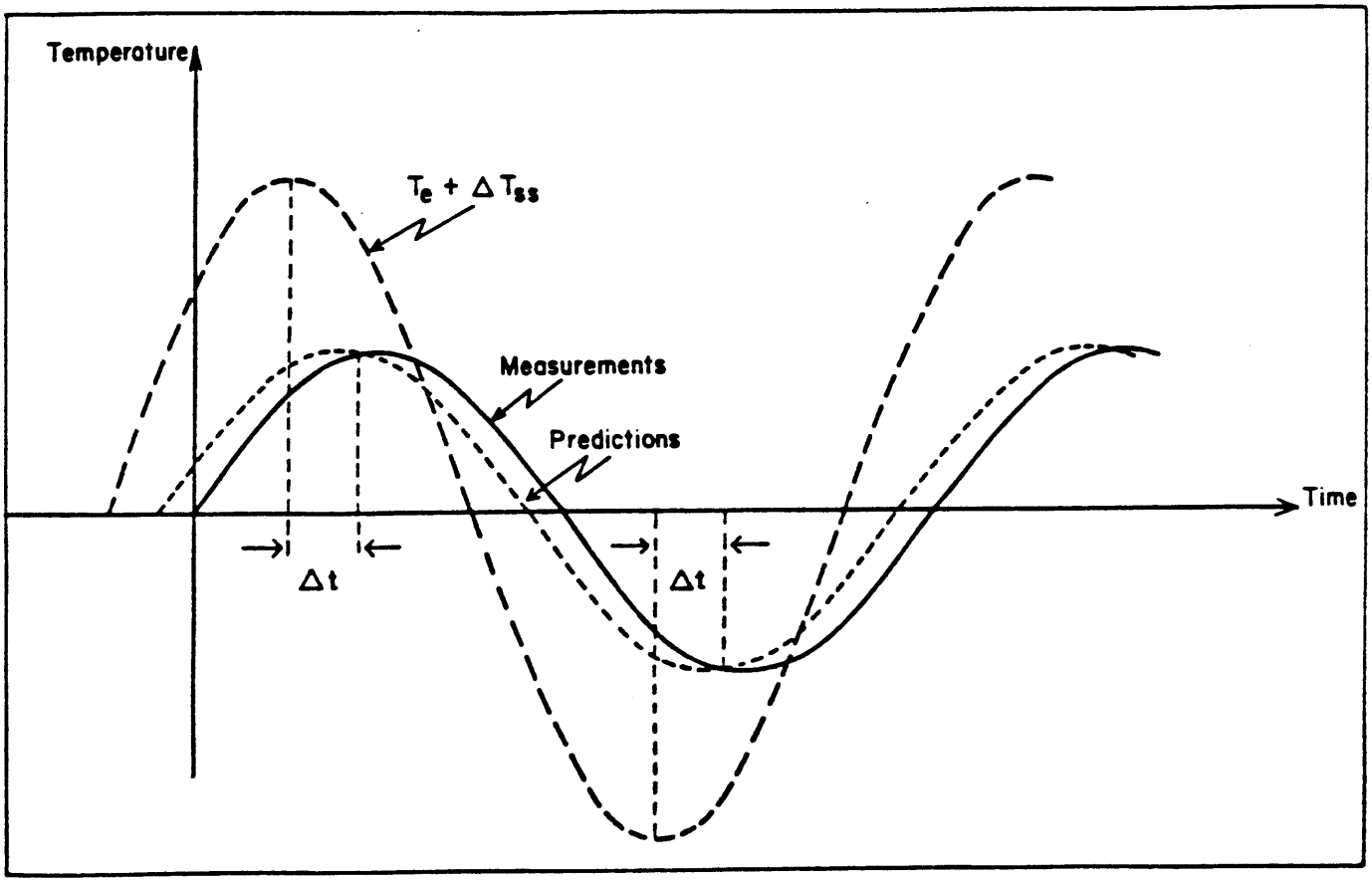

Figure 5.2 Schematic of Relationship between Raw Errors and Equilibrium Temperature at DIKE III

Regarding the meteorological forcing function, two candidates are examined: (a) long-wave radiation (discussed in Section 5.2.2.1) and (b) evaporative heat flux (discussed in Section 5.2.2.2). These two are chosen because they have the greatest uncertainties among the various surface heat transfer components.

Regarding the system response, again two candidates are examined: (a) spatially averaged response of the model to periodic warming and (b) longitudinal response based on the residence time in the WHTF. A brief discussion of each of the two candidates is given in Sections 5.2.3.1 and 5.2.3.2, respectively. Conclusion of this transient error analysis is given in Section 5.2.4.

5.2.2 Periodic Errors in Surface Heat Transfer

5.2.2.1 Long-Wave Radiation

The long-wave (atmopsheric) radiation formula proposed by Idso and Jackson (1969) replaced the formula due to Swinbank (1963) in the calibrated model as described by Wells et al. (1982) in order to improve the model's winter time performance. A comparison of several long-wave radiation calculation methods (see Table 5.2) developed over the past few decades is presented below using the air temperature and relative humidity data collected at North Anna Power Station. (N.B. Some of the formulae require water vapor pressure which can be readily obtained from air temperature and relative humidity by using the conversion formula rendered by Thackston (1974):

$$e_{sat} = 25.4 \times \exp(17.62 - \frac{9500.8}{T + 460})$$

Table 5.2 Summary of Long-Wave Radiation Calculation Methods (after Hatfield, 1983)

Method	Formulation for ε_{ac} *	Reference
Brunt	$0.51 + 0.066\ e_o^{1/2}$	Brunt (1932)
Swinbank	$0.92 \times 10^{-5}\ T_o^2$	Swinbank (1963)
Idso-Jackson	$1 - 0.261 \exp[-7.77\times10^{-4}(273-T_o)^2]$	Idso and Jackson (1969)
Brutsaert 1	$0.553\ e_o^{1/7}$	Brutsaert (1975)
Satterlund	$1.08[1 - \exp(-e_o^{T_o/2016})]$	Satterlund (1979)
Brutsaert 2	$0.575\ e_o^{1/7}$	Idso (1981)
Idso 1	$0.179\ e_o^{1/7} \exp(350/T_o)$	Idso (1981)
Idso 2	$0.7 + 5.95\times10^{-5} e_o \exp(1500/T_o)$	Idso (1981)

* ε_{ac} = atmospheric emissivity under clear sky
e_o = water vapor pressure in millibars
T_o = absolute air temperature in degrees Kelvin

where e_{sat} = saturation vapor pressure (mm Hg) and T = air temperature in degrees Fahrenheit.)

Since no real-time on-site measurements of incoming atmospheric radiation are available, little can be said regarding the performance of the various formulae. The goal of this study, however, is to compare formulae and to identify if the raw error might be partially offset by use of a different formula.

In this comparision, only the downward component of atmospheric radiation under clear sky is calculated such that

$$\phi_{ac} = \varepsilon_{ac} \sigma T_a^4 \qquad (5.31)$$

where ϕ_{ac} = downward atmospheric radiation under clear sky (watt per m^2)

ε_{ac} = atmospheric emissivity under clear sky, as given in Table 5.2,

σ = Stefan-Boltzmann constant
= 5.6697×10^{-8} W m^{-2} K^{-4}, and

T_a = absolute air temperature in degrees Kelvin.

Figure 5.3 shows the monthly-averaged values of downward long-wave radiation under clear sky for more than five years since August, 1978 as calculated by using the eight different proposed formulae. (A detailed tabulation of the values and statistics is attached as an appendix.) It is found that the ones by Idso (Idso 1 and Idso 2) give the highest all-season estimates of atmospheric radiation whereas the ones due to Brunt and Swinbank give the lowest. The remaining four formulae give results that are in general bounded by the above-mentioned four. Of these, Idso-Jackson gives the most modest range (i.e., low in the summer and high in the winter), followed by Satterland, which is

Figure 5.3 Monthly-Averaged Values of Downward Long-Wave Radiation Under Clear Sky Given by Eight Different Formulae

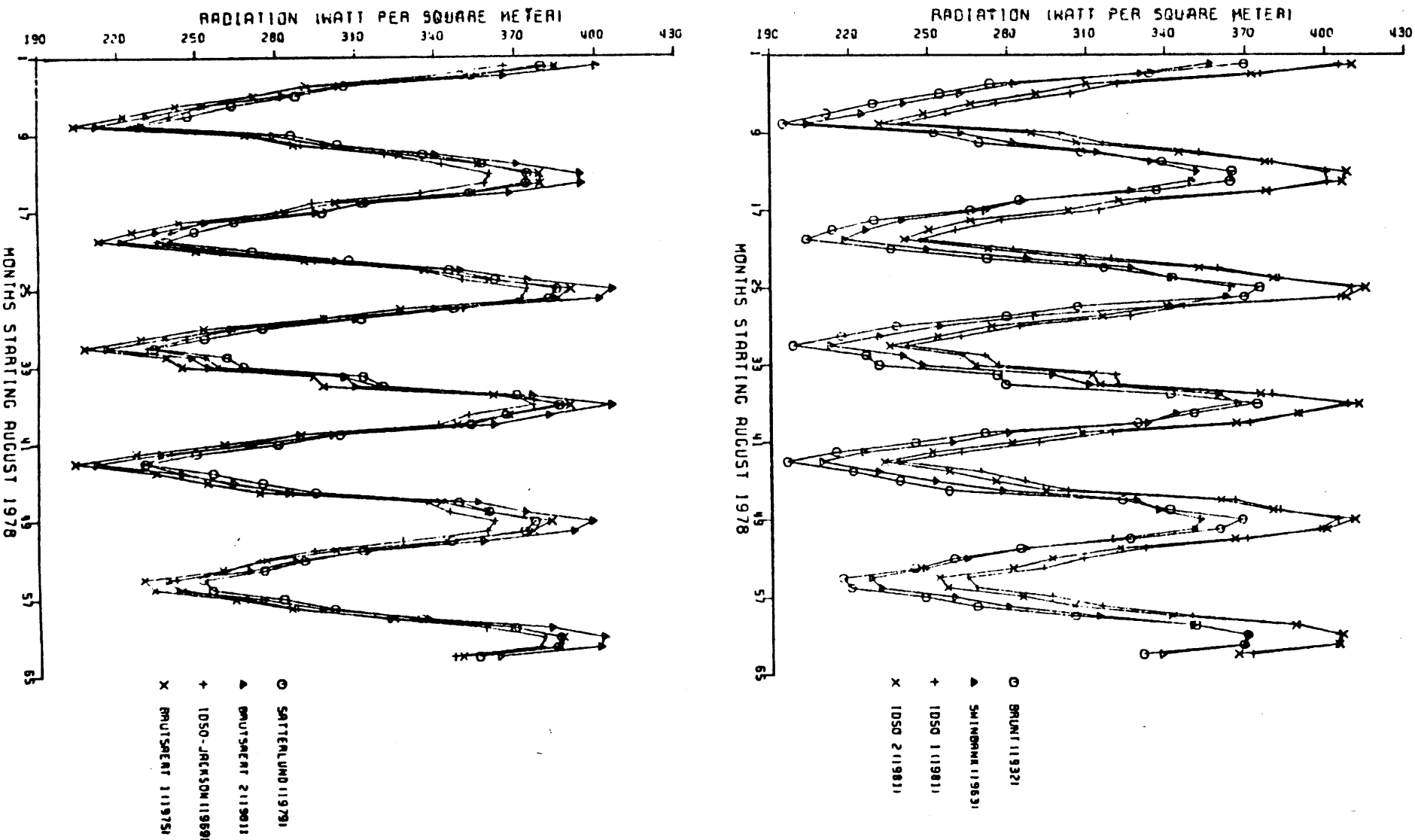

consistently higher than Idso-Jackson with a more pronounced difference during the summer. Brutsaert 2 is identical with Brutsaert 1 except the former is shifted upward by about 29 W m^{-2}. Both have a larger range than those given by Satterland and Idso-Jackson.

A closer examination of Figure 5.3 shows that there is not a single formula which gives higher values of long-wave radiation (and thus higher water temperature) than Idso-Jackson does during the months from August through December (when the model under-predicts at DIKE III) and at the same time gives lower values of long-wave radiation (and thus lower water temperature) during the months from January through July (when the model over-predicts at DIKE III). The closest candidate is Brutsaert 1 which gives higher estimates than Idso-Jackson does from May to October and lower estimates from November to April. Figure 5.4 shows daily estimates of long-wave radiation given by the two formulae in the year of 1979. However, difference between the two estimates for each day is very small in relation to the gross atmospheric radiation (usually less than 10%) such that improvement in model prediction is insignificant when the effect is translated to changes in surface water temperatures. In addition to small difference between the formulae, the fact that an error in atmospheric radiation would affect surface temperature throughout the whole cooling lake system is not consistent with the observation of a periodic error primarily at DIKE III. Thus, no recalibration of the model is made in this respect.

It is known that long-wave radiation increases when water vapor condenses into droplets in the atmosphere, and that a cloud base near the ground radiates virtually like a black body (emissivity approaches

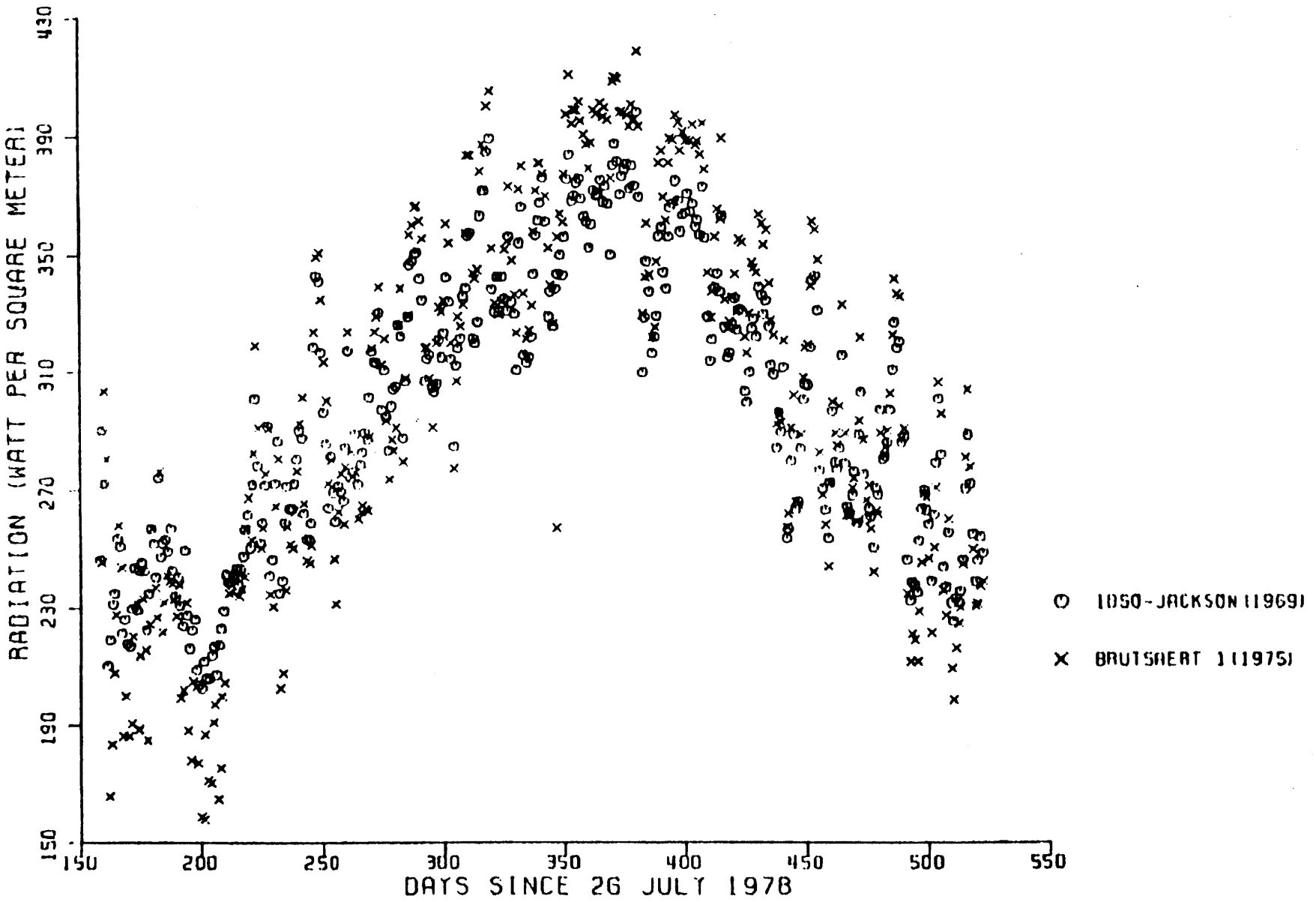

Figure 5.4 Daily Estimates of Long-Wave Radiation Given by Brutsaert 1 and Idso-Jackson

1.0). Kimball et al. (1982) concluded that the maximum increase in radiation over clear sky radiation could be about 40% with typical values of about 20%.

Several empirical approaches have been suggested for cloud cover correction. The one adopted in North Anna Cooling Pond Model uses the following relation:

$$\phi_a = \phi_{ac}(1 + k_1 C^2) \tag{5.32}$$

where

ϕ_a = downward atmospheric radiation for cloudy sky

ϕ_{ac} = clear sky downward atmopsheric radiation

C = portion of sky covered by cloud (value varies from 0 to 1)

k_1 = constant that depends on the nature and height of clouds.

Value of k_1 ranges from 0.04 for cirrus to 0.25 for nimbostratus or fog according to Bolz (1949). (See also Table 6.7 of Brutsaert, 1982). A constant value of $k_1 = 0.17$ is used in the model, as suggested by Wunderlich (1972), since no records of cloud types are available.

Another approach applies the correction to the effective outgoing radiation under clear sky, ϕ_o, according to the equation (Sellers, 1965):

$$\phi = \phi_o(1 - k_2 C^m) \tag{5.33}$$

where ϕ = effective outgoing radiation corrected for cloud cover, and k_2, m are constants to be determined from observations. In this approach, cloud effect is applied to both upward surface radiation and

downward sky radiation. However, the physical justification for applying a correction factor to the upward surface radiation is unclear and therefore the first approach is preferred to the second one (Salhotra et al., 1983).

5.2.2.2 Evaporative Heat Transfer

The fact that there is much stronger periodicity of the raw errors at DIKE III than at any other diagnostic control points suggest that the periodic error may be more associated with forced rather than with natural heat flux terms. This is suspected because the effects of forced heat fluxes decrease in the direction of flow from the plant condenser towards the plant intake, whereas effects of natural heat fluxes are relatively constant throughout the whole cooling lake system. And the fact that DIKE III is the nearest station to the condenser discharge among the diagnostic control points agrees with the hypothesis that periodicity of the raw error at the station is more related with the forced heat flux terms, namely, evaporation, conduction and back radiation; among these, evaporative transfer is most important because of its magnitude and uncertainty.

A periodic function was used to adjust the evaporation formula used in the WHTF in the calibrated model (p. 74, Wells et al.) such that

$$\alpha = 0.75 + 0.15 \sin\left(\frac{2\pi t}{365.25} - 1.03\right) \qquad (5.15b)$$

where t = Julian day of the year and α = correction factor multiplying the evaporative heat flux. This correction was intended to reduce the periodicity of the raw error. Justification for the correction was

that, owing to seasonal effects on wind direction, both air temperature and relative humidity are expected to be higher over the WHTF (relative to the meteorological tower measurements) in autumn, leading to lower evaporation than that predicted by meteorological tower data.

However, the model has also been run with a constant value of α = 0.75. (Figure 5.5 shows the corresponding raw error at DIKE III.) Comparison of Figures 4.3b and 5.5 shows that there is no significant improvement regarding the periodicity by applying the periodic function. In fact, harmonic analyses of the respective raw error time series show that amplitude of the raw error is only reduced from 1.096 °C to 1.080 °C (see Table 5.3), which is insignificant for practical purposes.

Fourier decomposition of the raw errors (with α = 0.75) gives ϕ_e = -0.4576 (i.e., $E(t) = 1.096 \sin(\omega t - 0.4576) + \varepsilon(t)$) which corresponds to a maximum over-prediction at t = 118 (or about April 28) and a maximum under-prediction at t = 301 (or about October 28). It is interesting, however, that the above phase is somewhat different from what one estimates visually from Figure 4.3b (i.e., peak on about June 1 and trough on about December 1). This deviation can be explained by the existence of "secondary" peaks to the left of the main peaks and these "secondary" peaks, though visually non-imposing, may carry considerable weight in determining the value of ϕ_e. The above discussion probably explains why Wells et al. (1982) employed a periodic function (Eq. 5.15) which gives a minimum value of evaporation over the WHTF on about December 1 and a maximum value on about June 1 in the calibrated model but was unable to reduce the periodicity of the raw error. Although there exist uncertainties associated with the

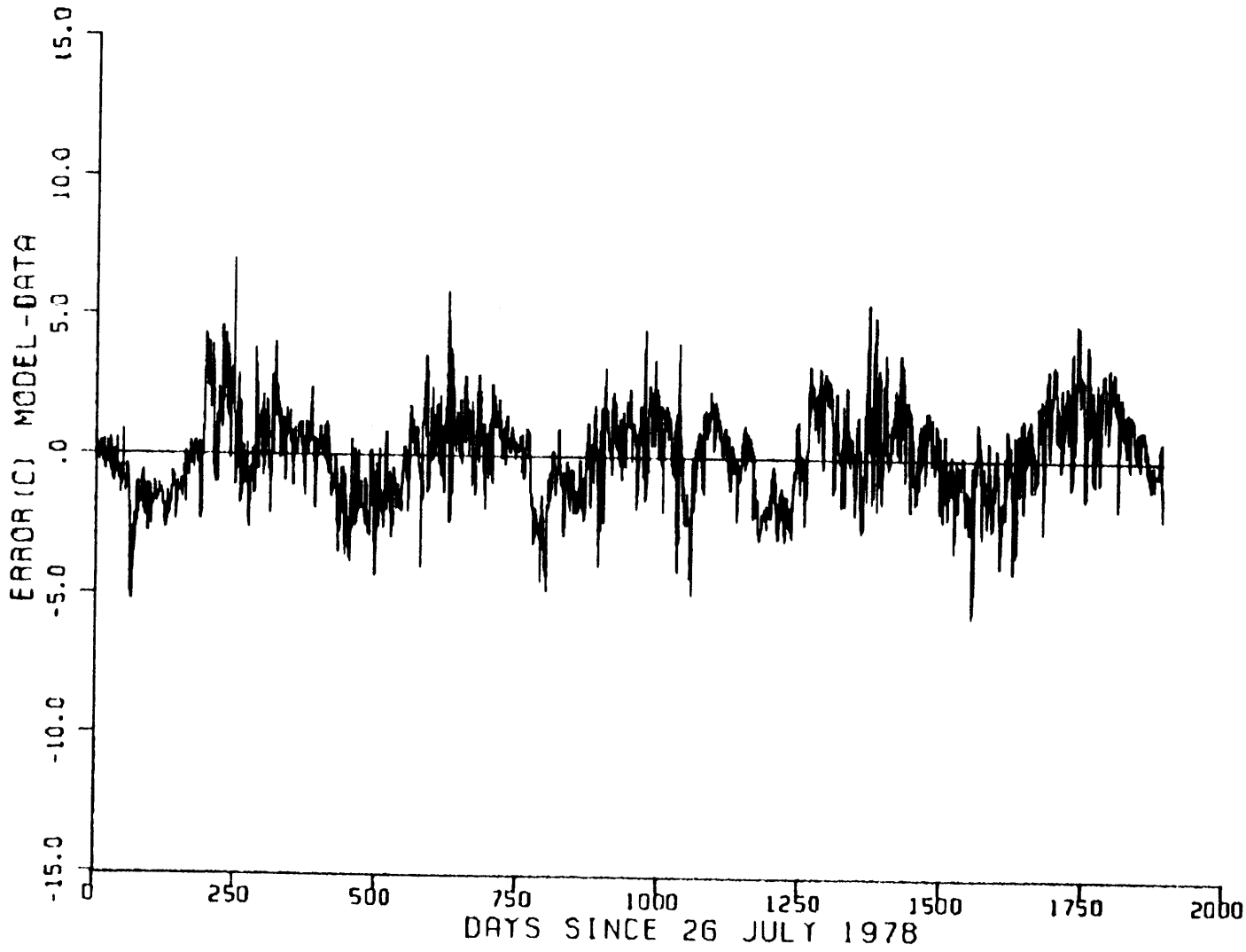

Figure 5.5 Raw Error at DIKE III (α = 0.75)

Table 5.3 Harmonic Analysis of Raw Error (DIKE III) Time Series

Description of Time Series	Raw Error Time Series		Measurements vs. Corresponing Predictions		Reference
	ϕ_e (radian)	E* (°C)	$\Delta\phi = \phi_p - \phi_m$ (radian)	$\Delta\phi$ (days)	
$\alpha = 0.75$	-0.4576	1.096	0.0939	5.46	Fig. 5.5
$\alpha = 0.75 + 0.15 \sin(\omega t - 1.0292)$	0.0769	1.080	0.0810	4.71	Fig. 4.3b
$\alpha = 0.75 + 0.15 \sin(\omega t - 0.4576)$	-0.3404	0.451	0.0383	2.23	-
$\alpha = 0.75 + 0.20 \sin(\omega t - 0.4576)$	-0.2249	0.232	0.0192	1.12	-
$\alpha = 0.75 + 0.25 \sin(\omega t - 0.4576)$	0.7276	0.045	0.0013	0.07	Fig. 5.6

annual variability in wind direction, the argument given by Wells et al. (pp. 72-74) provides the motivation for exploring a new periodic function for α so as to minimize the periodicity of the raw error.

Now that the immediate cause for the annual periodicity of the raw error at DIKE III is known (namely, measurements are lagging behind predictions by about 5.5 days), a new periodic function for α can be used so as to minimize the phase lag ($\Delta\phi = \phi_p - \phi_m$).

Knowing the value of ϕ_e for the raw error time series with α = 0.75 (see Table 5.1), we can try the following periodic function:

$$\alpha = 0.75 + 0.15 \sin(\frac{2\pi t}{365.25} - 0.4576) \qquad (5.34)$$

Table 5.3 shows that the amplitude of the resulting raw error is reduced to 0.45 °C. With a little trial and error, the following periodic function is found to be near optimal:

$$\alpha = 0.75 + 0.25 \sin(\frac{2\pi t}{365.25} - 0.4576) \qquad (5.35)$$

Eq. 5.35 gives maximum evaporation (α = 1) on about April 28 (t = 118) and minimum evaporation (α = 0.5) on about October 28 (t = 301). This new correction function of α essentially shifts predictions back in phase with the measurements (new $\Delta\phi$ = 0.0013 or 0.07 days along the time axis; see Table 5.3). Amplitude of the resulting raw error (Figure 5.6) is further reduced to 0.045 °C, less then 5% of the original value.

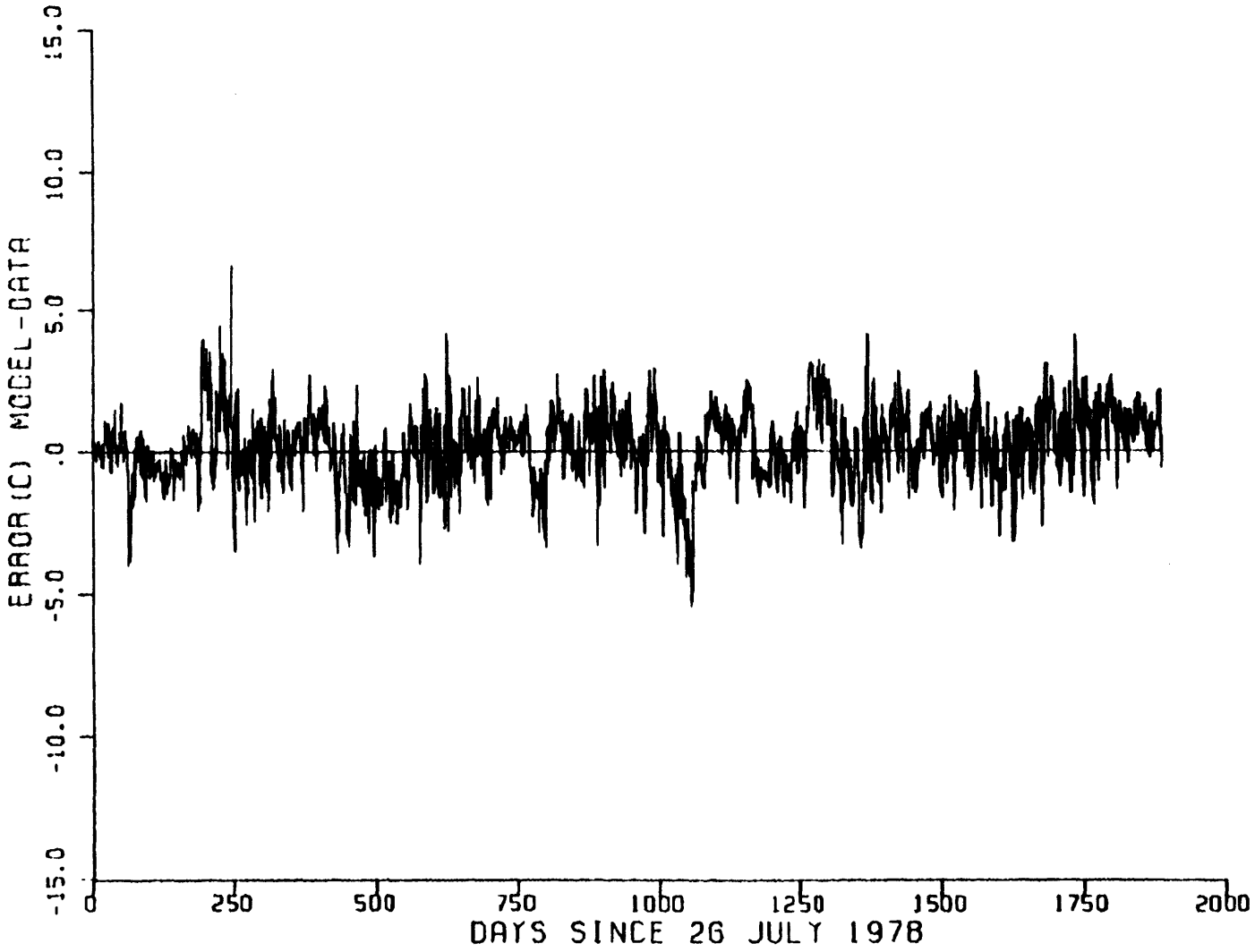

Figure 5.6 Raw Error at DIKE III ($\alpha = 0.75+0.25 \sin(\omega t-0.4576)$)

5.2.3 Errors in System Reponse

5.2.3.1 Spatially Averaged Response

A possible reason for the observed annual periodicity of the raw error at DIKE III is that the spatially averaged response of the model to periodic warming is too quick. In order to examine this possibility, a simple fully-mixed water body is considered with transient heat budget given by

$$\frac{dT}{dt} = - \frac{K}{\rho c \bar{h}} (T - T_e) \tag{5.36}$$

where T is the transient temperature of the water body, c is the specific heat capacity of water, $\bar{h}$ is the average pond depth (volume/surface area), and surface heat exchange has been linearized using the equilibrium temperature T_e and a constant surface heat exchange coefficient K. Furthermore, let the equilibrium temperature be represented by a periodic function such that

$$T_e(t) = T_e^* \sin(\omega t + \phi_{T_e}) \tag{5.37}$$

Where T_e^* and ϕ_{T_e} are the corresponding amplitude and phase, respectively.

If we assume that the true temperature T = T(t) is accurately represented by the measurements, M(t) (refer to Eq. 5.1), then it follows that we can write

$$T(t) = M^* \sin(\omega t + \phi_m) \tag{5.38}$$

Differentiating Eq. 5.38, we have

$$\frac{dT}{dt} = \omega M^* \cos(\omega t + \phi_m) \tag{5.39}$$

Equating Eqs. 5.36 and 5.39, one can arrive at a simple relationship between the amplitudes of the two time series and also an expression for the phase shift, $\phi_{T_e} - \phi_m$ (Adams, 1982):

$$M^* = T_e^* \frac{1}{\sqrt{1 + (\omega\tau)^2}} \tag{5.40}$$

and

$$\phi_{T_e} - \phi_m = \tan^{-1}(\omega\tau) \tag{5.41}$$

where $\tau = \rho ch/K$ is the time constant for surface warming (or cooling), $\omega = 2\pi/T$ and $T = 365.25$ days.

Resorting to the Imperial Units for a quick check, we have $\rho c \simeq 62$ Btu ft^{-3} $°F^{-1}$; if we assume the values of $h = \bar{2}5$ ft and $K = 150$ Btu ft^{-2} $°F^{-1}$ day^{-1} for the North Anna cooling lake system, then $\tau \simeq$ 10 days, $\omega\tau \simeq 0.178$ and Eq. 5.41 will give $\phi_{T_e} - \phi_m \simeq 0.176$ radians or $\simeq$ 10 days when translated to the time axis. However, it is known from Section 5.2.1 that $\Delta\phi = \phi_p - \phi_m = 0.0939$ or about 5.5 days between predictions and measurements (see Table 5.1); thus it is doubtful that τ is off by a factor of 2 (N.B. $\tau = \rho ch/K$). Clearly, the values of depth used in the models are reasonably accurate and, if K were that far off, then the average error at DIKE III would not have been near zero. In addition, error in τ would have been manifest throughout the cooling lake system, not primarily at DIKE III. Based on the above argument, we can rule out the possibility of major errors associated with spatially averaged system response.

5.2.3.2 Longitudinal System Response

In order to account for transients in the WHTF a lag-time correction is incorporated in the model. This procedure was utilized, rather than a forward stepping transient simulation, because of the absence of transient analysis for the side arm flows. A residence time (t_r) is computed dynamically (i.e., once each day) for each pond within the WHTF based on flow rate and pond size. The temperature at the end of the pond on day t is determined from the upstream temperature at the entrance of the same pond on day $t - t_r$ and the degree of warming or cooling during the time span of t_r. In other words,

$$T(t) = f(Q(t - t_r), K(t), T_e(t), T_o(t - t_r)) \tag{5.42}$$

where T_o is the upstream temperature of the pond, K is the surface heat exchange coefficient, T_e is the equilibrium temperature, Q is the condenser flow rate, and T refers to the temperature at the end of the pond.

Since meteorological variables act over the entire period of t_r days, rather than on one day, t, Wells et al. (1982) implemented an exponential filtering scheme, as described by Adams and Koussis (1980), for T_e and K in order to approximate the correct time response. The equation describing the exponential filter for T_e (and similar for K) was

$$\langle T_e(t) \rangle = \frac{\sum_{n=1}^{t_r/\Delta t} T_e(t - n\Delta t) \exp(-(n-1)\, k'\, \Delta t)}{\sum_{n=1}^{t_r/\Delta t} \exp(-(n-1)\, k'\, \Delta t)} \tag{5.43}$$

where $k' = K'/\rho C_p h$ is the kinematic surface exchange coefficient, h is the averge depth of pond, < > denotes the filtered variable, Δt is the time step (one day), and K' represents the filtered surface heat exchange coefficient. The filtered value of T_e is then used in a steady state analysis of heat loss within the ponds. Thus for a pond m with no side arm,

$$T_m(t) = \langle T_e(t) \rangle + [T_{m-1}(t-t_{r_m}) - \langle T_e(t) \rangle] e^{-kt_{r_m}} \qquad (5.44)$$

In general, the lagging and filtering combination resulted in a much smoother and accurate prediction of transient temperatures throughout the WHTF (Wells et al., 1982). However, it is possible that the computed residence times may be off by several days, thus causing the phase lag between measurements and predictions of the surface temperature at DIKE III.

Typical values of the residence times (as computed by the North Anna Cooling Lake Model) for Ponds 1, 2, 3 of the WHTF for one-unit operation are 0.5, 3 and 2 days, respectively, with correspondingly lower values for 2-unit operation. In order to see how sensitive model predicitions are to different residence times, the model was run with various sets of fixed residence times for the three ponds of the WHTF. Statistical data were compiled and harmonic analyses made for the raw error at DIKE III. Results are given in Table 5.4. (Notice that these runs are made with a constant factor for evaporation (α = 0.75).) The results show that predictions are generally improved by an increase of total residence time (t_r) of the WHTF as indicated by the decrease of

Table 5.4 Sensitivity Test of Raw Errors at DIKE III with Respect to Different Residence Times (Runs 1 - 7)

Run No.	Fixed Residence Times Used for Ponds 1, 2, 3 (Day)	Total Residence Time for WHTF (Day)	Mean (°C)	Standard Deviation (°C)	ϕ (radian)	E* (°C)
1	0, 0, 0	0	0.13	1.98	-0.4716	1.63
2	1, 1, 1	3	0.05	1.63	-0.4815	1.27
3	1, 2, 2	5	0.03	1.52	-0.4408	1.03
4	2, 3, 3	8	0.03	1.43	-0.4719	0.78
5	4, 5, 5	13	0.04	1.41	0.0842	0.33
6	5, 6, 6	17	0.04	1.43	1.2078	0.26
7	10,10,10	30	0.00	1.87	-4.2065	1.27
8	residence times computed dynamically for each day	based on whole volume	0.27	1.60	-4.3033	0.52
9		based on 75% of whole volume	0.31	1.44	0.9827	0.22
10		original computation	0.04	1.59	-0.4576	1.10

N.B. ϕ and E* denote the phase and amplitude of a sine curve fitted to the raw error time series (see Section 5.2.1).

E*. The above findings provide a motivation for re-examining the residence time calculation as employed by Wells et al. (1982).

It is noticed that in Wells et al. (1982) and previous versions of the cooling lake model, residence times of the WHTF were computed such that

$$\text{RESTIM} = \frac{\text{ULD}_1 \times A_1}{Q} + \frac{\text{ULD}_2 \times A_2}{Q - \text{QSA}_1} + \frac{\text{ULD}_3 \times A_3}{Q - \text{QSA}_1 - \text{QSA}_2} \qquad (5.45)$$

where RESTIM is the residence time of each reach of the WHTF, ULD_i represents the upper layer depth of section i within that reach, A_i is the surface area of section i, Q is the rate of flow entering the reach, and QSA_j denotes the side arm flow rate of the jth side arm. This routine is repeated for all three of the reaches within the WHTF.

Eq. 5.45 gives only the residence times of the upper layers of the main WHTF ponds while ignorning the volume of the lower layers and that of the side arms. Physically, this represents a lower limit on the true residence time. An upper limit (and perhaps more physically realistic estimate) would be based on the entire volume. Accordingly, Eq. 5.45 is replaced by

$$\text{RESTIM} = \frac{(A_1 + A_2 + A_3) \times D + H_1 \times \text{SA}_1 + H_2 \times \text{SA}_2}{Q_p} \qquad (5.46)$$

where SA_j and H_j represent the surface area and average depth, respectively, of side arm j, Q_p is the condenser flow rate, and D is the average depth of the main ponds within the WHTF.

The model was run using Eq. 5.46 (and $\alpha = 0.75$) to compute residence times dynamically. Statistics of the raw error are included

in Table 5.4 (Run 8). It is noticed that periodicity of the raw error at DIKE III is reduced substantially, as indicated by the reduction of the amplitude to less than half (E* = 0.52 °C, Table 5.4) of its original value (E* = 1.10 °C, Table 5.1). Typical values of the computed residence times in this run are around 1, 8 and 3 days (or a total of about 12 days), with maximum values reaching 3, 24, and 9 days for Ponds 1, 2 and 3, respectively. However, the value of $\Delta\phi$ ($= \phi_p - \phi_m$, see Section 5.2.1) in this run is about -2 days, whereas $\Delta\phi \simeq 5.5$ days with Eq. 5.45. In other words, on average, predictions lag behind the measurements, indicating that the computed residence time may have been too large.

A final sensitivity run was made using a dynamic residence time based on 75% of the entire volume (i.e., the right-hand side of Eq. 5.46 was multiplied by 0.75). A re-run of the model shows that periodicity of the raw error at DIKE III (Figure 5.7) is further reduced to give an amplitude of about 0.22 °C (refer to Run 9 of Table 5.4). (N.B. Phase lag between measurements and predictions in this case is almost reduced to zero ($\Delta\phi \simeq 0.1$ day) whereas P* = 11.463 °C and M* = 11.687 °C (refer to Eqs. 5.2 and 5.3).) This suggests that the finite raw error, although with greatly reduced amplitude, is largely caused by the fact that $M^* \neq P^*$ (see also Section 5.2.1). Notice that applying the correction factor to reduce the computed residence times is physically justified since some pockets of water in the WHTF (and particularly in the side arms) are stagnant and do not circulate very much (Adams and Wells, 1984). Still, the value of 75% is approximate, and though the computed residence times look reasonable, ideally they should be confirmed with a dye study. Such a study would elucidate not

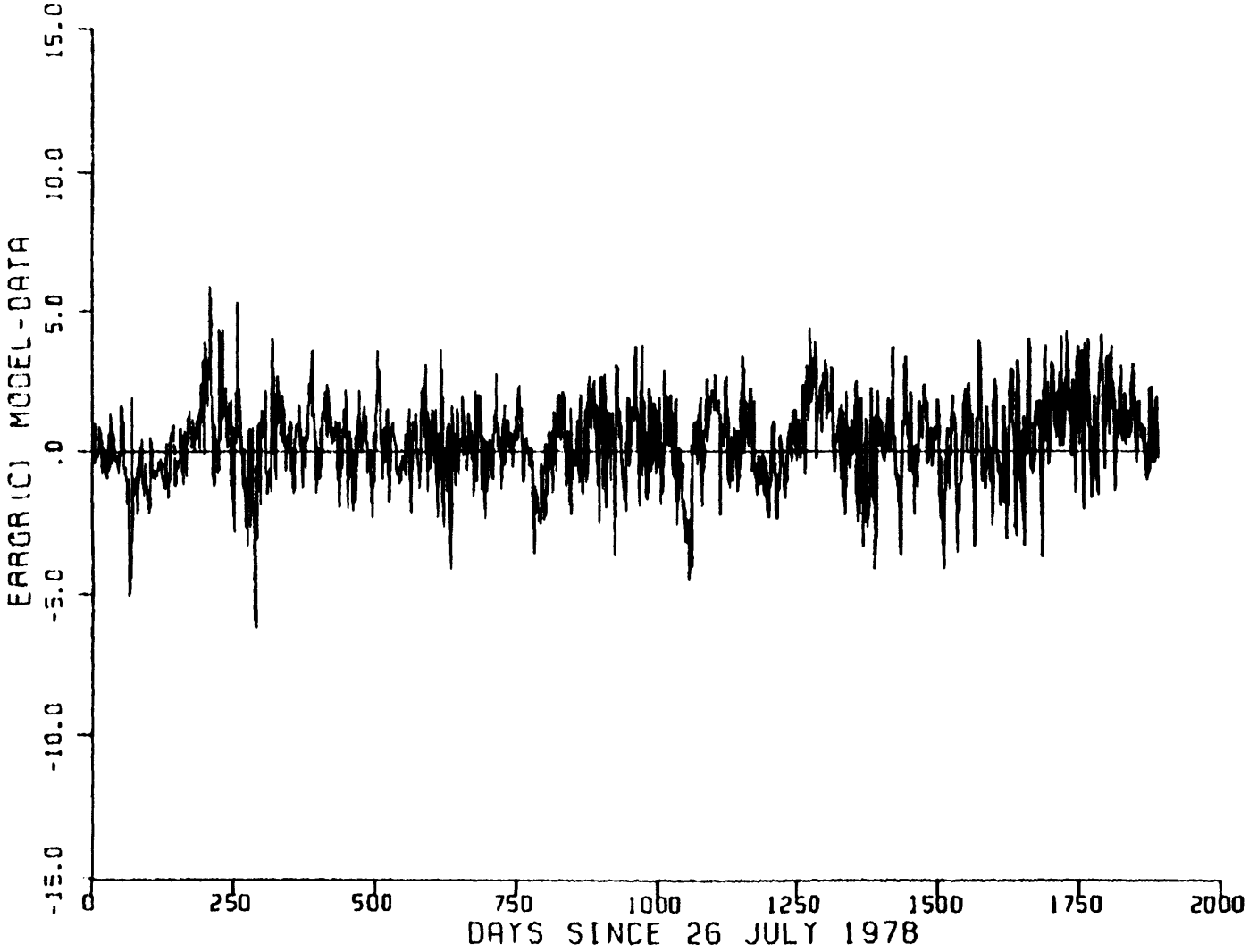

Figure 5.7 Raw Error at DIKE III (α = 0.75; lag time over WHTF based on 75% of whole volume)

only the effective residence time but also the complete residence time distribution which is needed if a more complete transient analysis is desired. In the absence of such confirmation, Eq. 5.46 with a 75% correction factor is used because it appears more reasonable than Eq. 5.45 and significantly reduces the observed phase lag between measurements and predictions at DIKE III.

5.2.4 Conclusion of Transient Error Analysis

Two possible reasons for the annual periodicity of the raw errors observed primarily at DIKE III have been identified, namely, errors associated with (1) the forcing function and (2) the system response. Two candidates for each of the possible reasons have been considered: (1a) atmospheric radiation, (1b) evaporation, (2a) spatially-averaged system response, and (2b) longitudinal system response. Among the four candidates, both (1a) and (2a) are ruled out. (1b) is possible since a moderate annual adjustment in the rate of evaporation over the WHTF ($\alpha = 0.75 \pm 0.25$) essentially eliminates the periodicity of the raw error. Some seasonal adjustment of evaporation rate can be justified by seasonal differences in wind direction. However, there is no way of verifying the exact magnitude because of insufficient meteorological measurements. (2b) seems to be most plausible because of the strong sensitivity of the periodicity to residence time and because of the uncertainties in the actual residence time. The adopted approach wherein residence time is based on a fraction (75%) of the entire volume seems more rational than that used previously and also results in a substantial reduction of the periodicity (reduced to less than a quarter of the original value in terms of amplitude of the raw error

and to near zero in terms of phase difference between measurement and prediction). However, we emphasize that there is still some uncertainties concerning the actual residence time distribution which would require a dye study for further confirmation.

5.3 Steady State Errors at DISCHARGE

Error analysis in Chapter 4 shows that the surface temperature at DISCHARGE is consistently over-predicted by the model by an average of about 0.7 °C while the mean error at INTAKE is 0°C. Predictions between INTAKE and DISCHARGE depend primarily on the condenser temperature rise which, in turn, depends on the rate of waste heat rejected to the WHTF and the circulating flow rate. These two variables are computed from daily-averaged values of electrical power production and the number of circulating water pumps using formulae suggested by VEPCO and reported by Wells et al. (1982).

To test model sensitivity to a small decrease in condenser temperature rise, three different runs of the model were made:

(0) no adjustment applied,

(1) $Q_1 = Q_0 \times 1.1$, $\Delta T_1 = \Delta T_0/1.1$; i.e., total heat load remains unchanged while temperature rise is reduced by about 9%;

(2) $Q_1 = Q_0$, $\Delta T_1 = \Delta T_0/1.1$; i.e., both total heat rejected and temperature rise are reduced by about 9%.

In the above, Q_1 and ΔT_1 represent the adjusted flow rate and temperature rise across the plant condenser, respectively, and Q_0, ΔT_0 are the reported values. (N.B., these runs are independent of the recalibration effort mentioned in Section 5.2, i.e., a value of α =

0.75 was used as the correction factor for evaporation over the WHTF, and the original residence time calculation was used.)

Mean raw errors at the four diagnostic control points for the three runs are listed in Table 5.5. It is noticed that the delta error across the plant (mean error at DISCHARGE minus mean error at INTAKE) is reduced from 0.74°C in Run 0 to about 0.20°C in Runs 1 and 2. This suggests that the optimal decrease in temperature rise should be about 13% (9%*0.74/(0.74-0.20)) and that both total heat load and condenser flow rate should be adjusted. Subsequent discussion with VEPCO confirmed that the average rate of waste heat rejection into the WHTF was about 8% less than what had previously been assumed, and that the condenser flow rate was quite sensitive to the pumping head. Another run (Run 3) was thus made based on the new heat rejection data from VEPCO and the objective of minimizing the delta error between INTAKE and DISCHARGE. Parameters were:

(3) $Q_1 = Q_0 \times 1.054$, $\Delta T_1 = \Delta T_0 \times 0.874$; i.e., total heat rejection is reduced by about 8% and temperature rise is reduced by about 13%.

Mean raw errors at the four diagnostic control points for Run 3 are also listed in Table 5.5. It is noticed that the delta error between DISCHARGE and INTAKE is greatly reduced, and that the raw error at DIKE III and BR. PT. are both acceptably small. The correction as employed in Run 3 is hence incorporated as part of the recalibration effort to serve as a basis for the final run.

Table 5.5 Mean Raw Errors for Runs 0, 1, 2 and 3

Mean Raw Error (°C)	Run 0	Run 1	Run 2	Run 3
DISCHARGE	0.74	0.29	0.11	0.00
DIKE III	0.29	0.25	0.01	0.05
BR. PT.	0.25	0.31	0.10	0.16
INTAKE	0.00	0.08	-0.09	-0.03

6. MODEL VALIDATION

6.1 Introduction

Chapter 5 described the efforts of model recalibration which were motivated by the results of surface temperature analysis in Chapter 4. Two changes of the model were made: computation of residence times in the WHTF (with a 75% correction factor applied) and adjustment of plant operation data (with reduced heat load and increased flow rate); both changes were implemented as options which could be switched off by changing an input data file to the model.

In this chapter continuous predictions given by the recalibrated model are compared with measurement data over the five-year simulation period (1978 - 1983). Section 6.2 will discuss the results of surface temperature analysis. Vertical temperature profiles in Lake Anna will be shown and discussed in Section 6.3.

6.2 Surface Temperature Error Analysis

Surface temperature error analysis is made for the four representative diagnostic control points over the cooling lake system (refer to Figure 4.1). Figures 6.1a to d show the raw errors and their statistical information is given in Table 6.1. Comparison with statistics given by the model described in Wells et al. (1982) shows that the mean raw error at DISCHARGE is reduced substantially without additional under-prediction at INTAKE, which has already been negligible. The model is also seen to have improved at other stations in terms of reduced standard deviations and/or magnitudes of means.

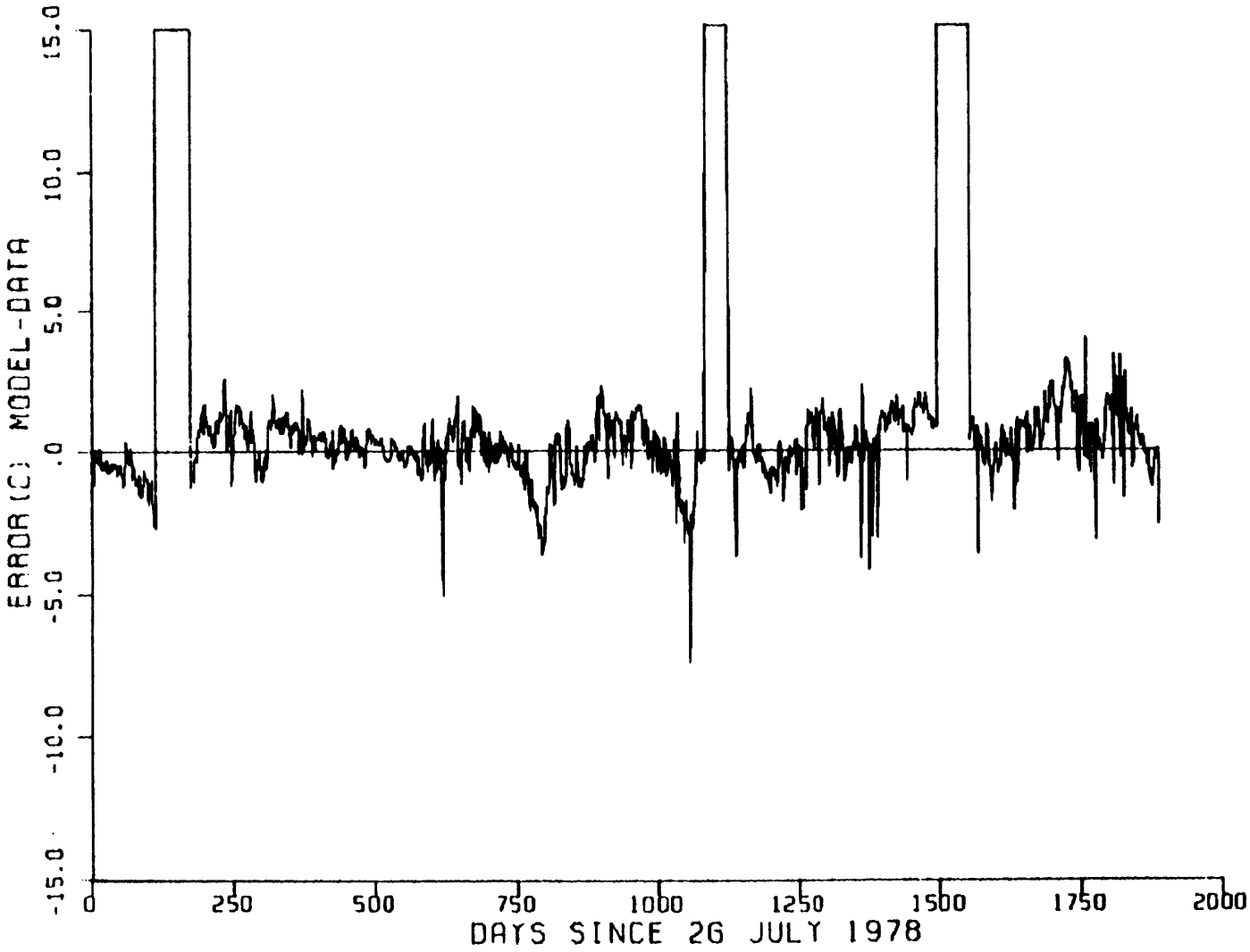

Figure 6.1a Raw Error at DISCHARGE (Recalibrated Model)

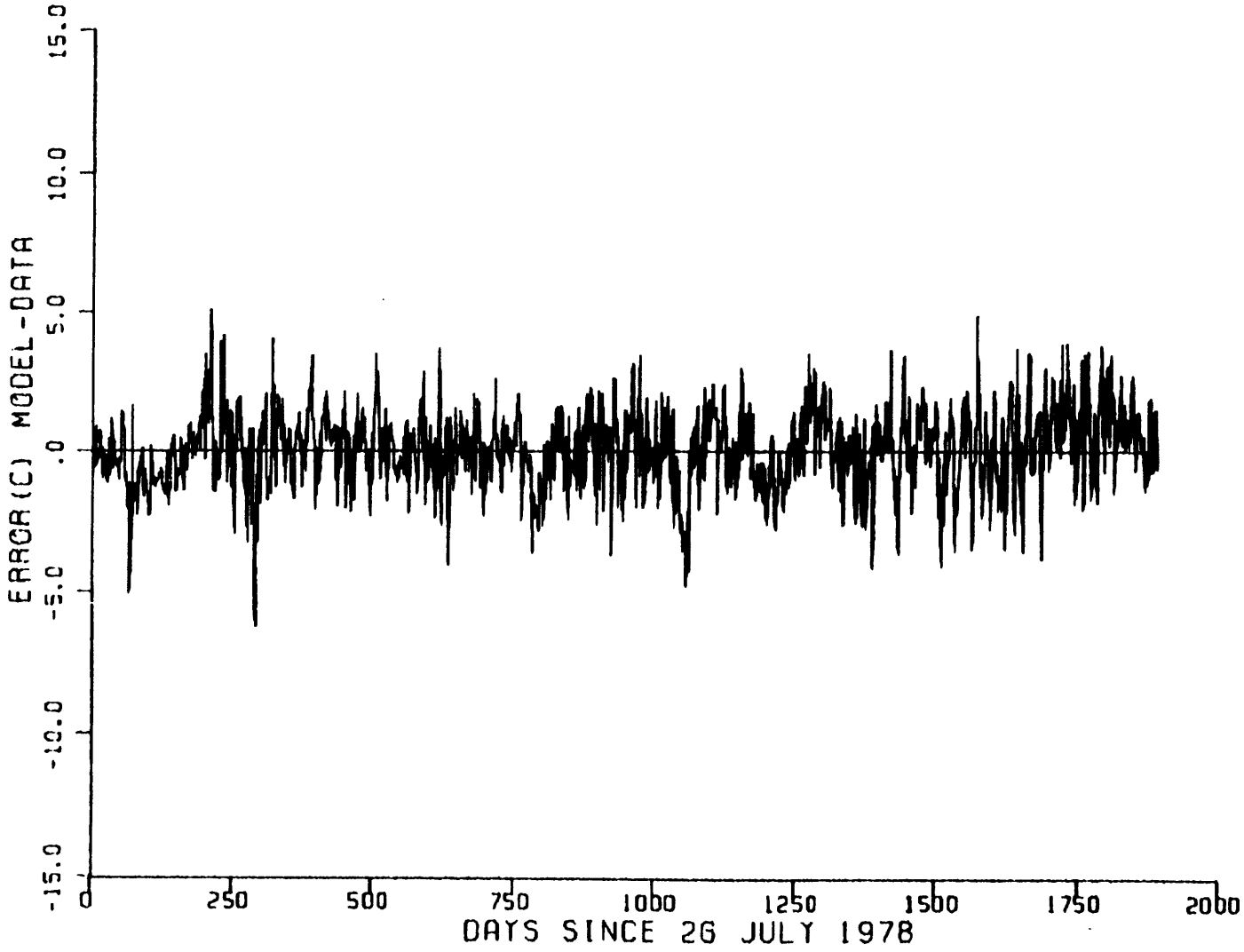

Figure 6.1b Raw Error at DIKE III (Recalibrated Model)

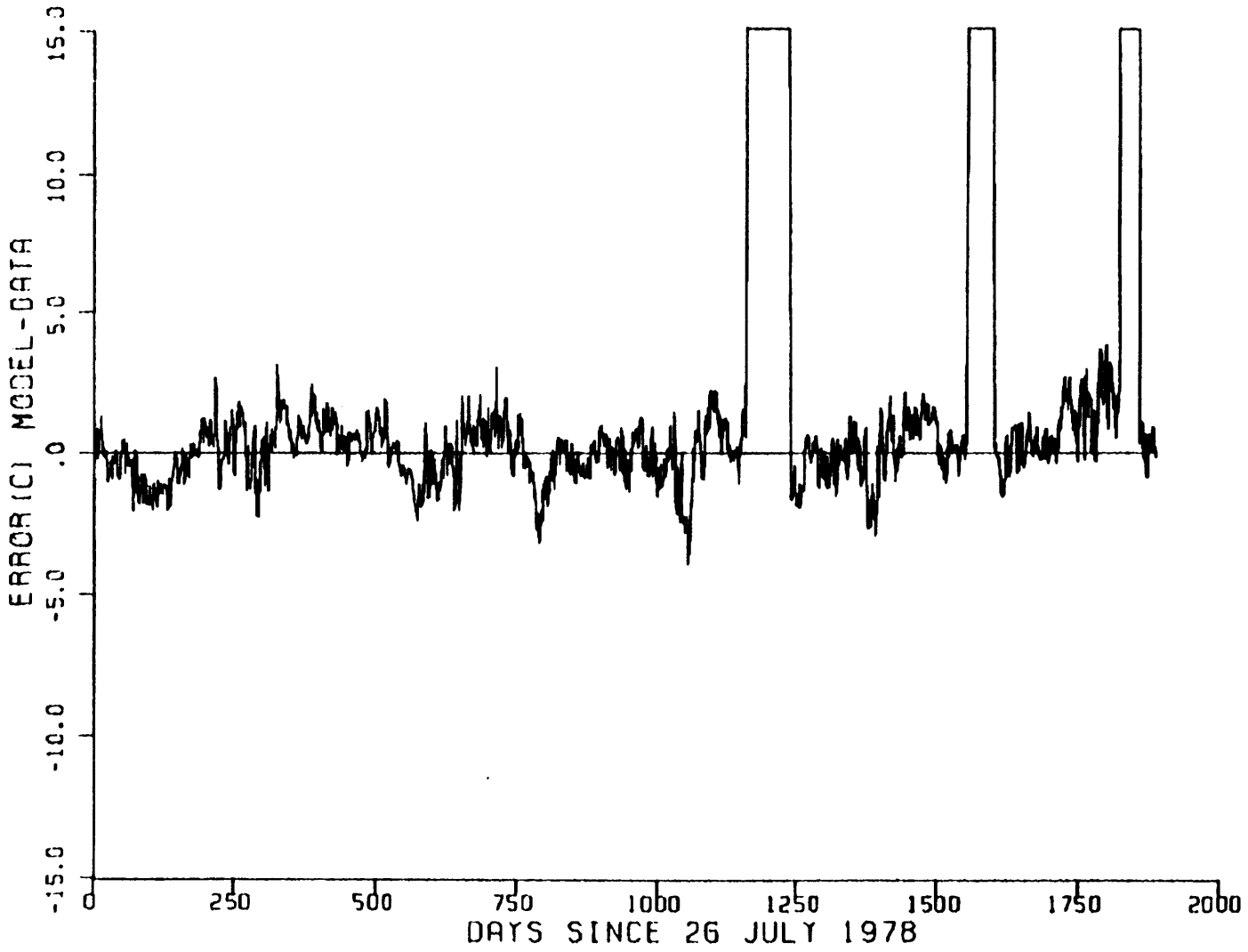

Figure 6.1c Raw Error at BR. PT. (Recalibrated Model)

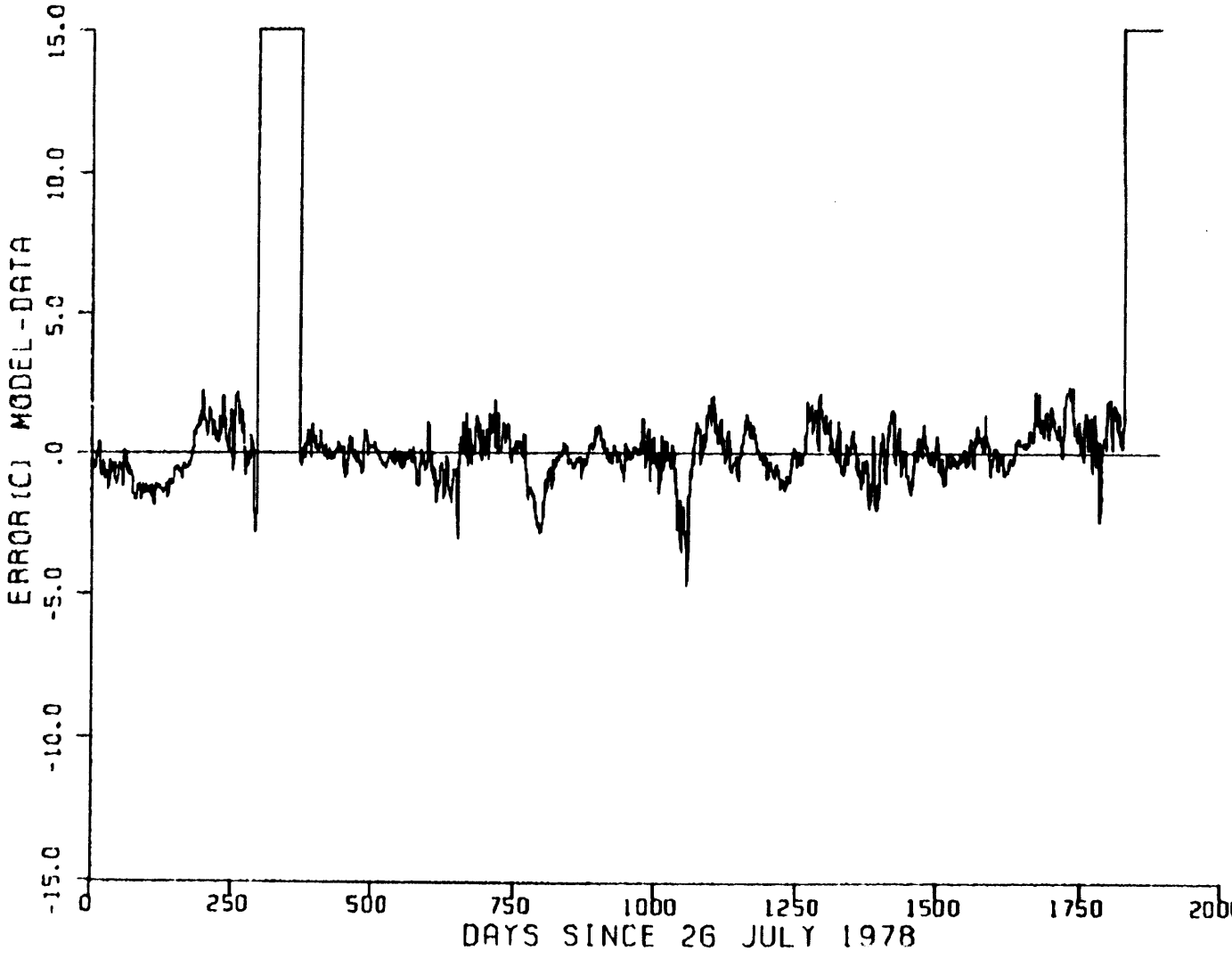

Figure 6.1d Raw Error at INTAKE (Recalibrated Model)

Table 6.1 Comparison of Statistics of Raw Errors at Four Diagnostic Control Points between Recalibrated Model and Model in Wells et al. (Five-Year Simulation for Both Cases).

Station	Mean (°C)		Standard Deviation (°C)		Sample Size
	Recalibrated Model	Wells et al.	Recalibrated Model	Wells et al.	(Day)
DISCHARGE	-0.02	0.69	1.11	1.23	1633
DIKE III	0.07	-0.03	1.37	1.54	1893
BR. PT.	0.16	0.11	1.04	1.10	1733
INTAKE	0.01	-0.06	0.80	0.98	1752

Comparison between Figures 4.3 b and 6.1 b shows that the annual periodicity at DIKE III is greatly reduced. Harmonic analysis gives an amplitude of E* = 0.12 °C, about 10% of the value (E* = 1.08°C, see Table 5.3) before recalibration. This remaining amplitude seems tolerable since in general we would expect to see some error at the annual period for all four stations because temperature changes with season and the model representation of heat fluxes is not perfect; as an example, we would probably see some differences due to the use of different atmospheric radiation formulae.

In addition to overall averages for the whole simulation period, monthly averages of the raw errors (see Section 4.4) at the four diagnostic control points are also compiled and shown in Table 6.2. When compared with Table 4.4, the former shows that magnitudes of the monthly averages of raw errors are in general reduced and also have become more random especially for DIKE III.

6.3 Vertical Temperature Profiles in Lake Anna

Figures 6.2a-6.2h show the measured and predicted vertical temperature profiles in the main lake for different seasons in 1982 and 1983 at two locations: (1) near the condenser intake and (2) near the dam at the downstream end of Lake Anna. (They correspond to Stations LA9 and LA13, respectively. See Figure 3.2 of Wells et al., 1982.) Comparisons between measurements and predictions indicate that the dynamic nature of the data both in space and time is satisfactorily represented by the model's characterization of the mixed layer and the vertical heat diffusivity in the hypolimnion. In addition, it is worth commenting that, firstly, recalibration of model did not change the

Table 6.2 Monthly Averages* of Raw Errors at Four Diagnostic Control Points (Recalibrated Model)

Month	DISCHARGE	DIKE III	BR. PT.	INTAKE
JAN	0.21[4]	0.42	0.01	0.22
FEB	0.36	0.63	-0.12	0.54
MAR	0.43	0.25	0.00	0.39
APR	0.40	-0.05	0.22	0.17
MAY	-0.06	0.04	0.02	-0.17[4]
JUN	-0.02	-0.16	0.40	-0.14[4]
JUL	0.74[4]	0.53	0.89[4]	0.43[3]
AUG	-0.10[4]	0.51[6]	0.73	0.17
SEP	-0.69	-0.22[6]	0.01	-0.46
OCT	-0.51[4]	-0.44	-0.46[3]	-0.36
NOV	-0.36[4]	-0.45	-0.35[3]	-0.31
DEC	-0.30[4]	-0.19	-0.15[3]	-0.34

---

* all are five-year averages except as specified

[6] six-year average

[4] four-year average

[3] three year average

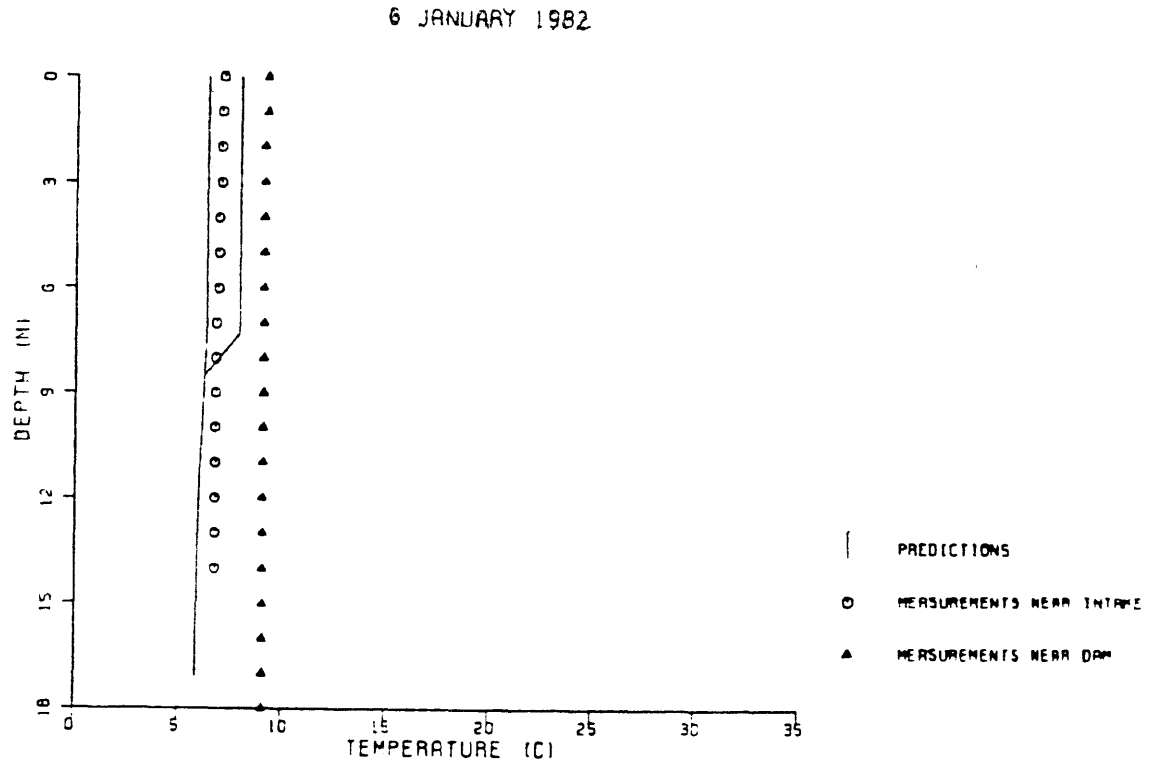

Figure 6.2a

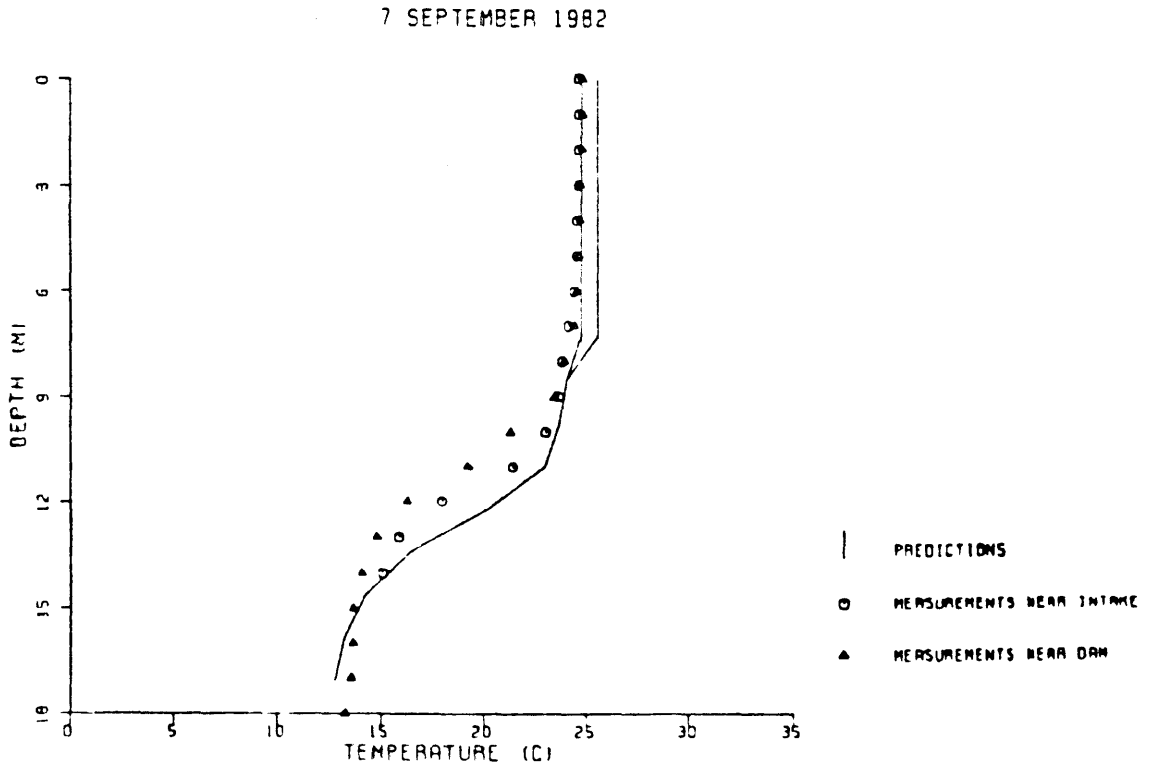

Figure 6.2b

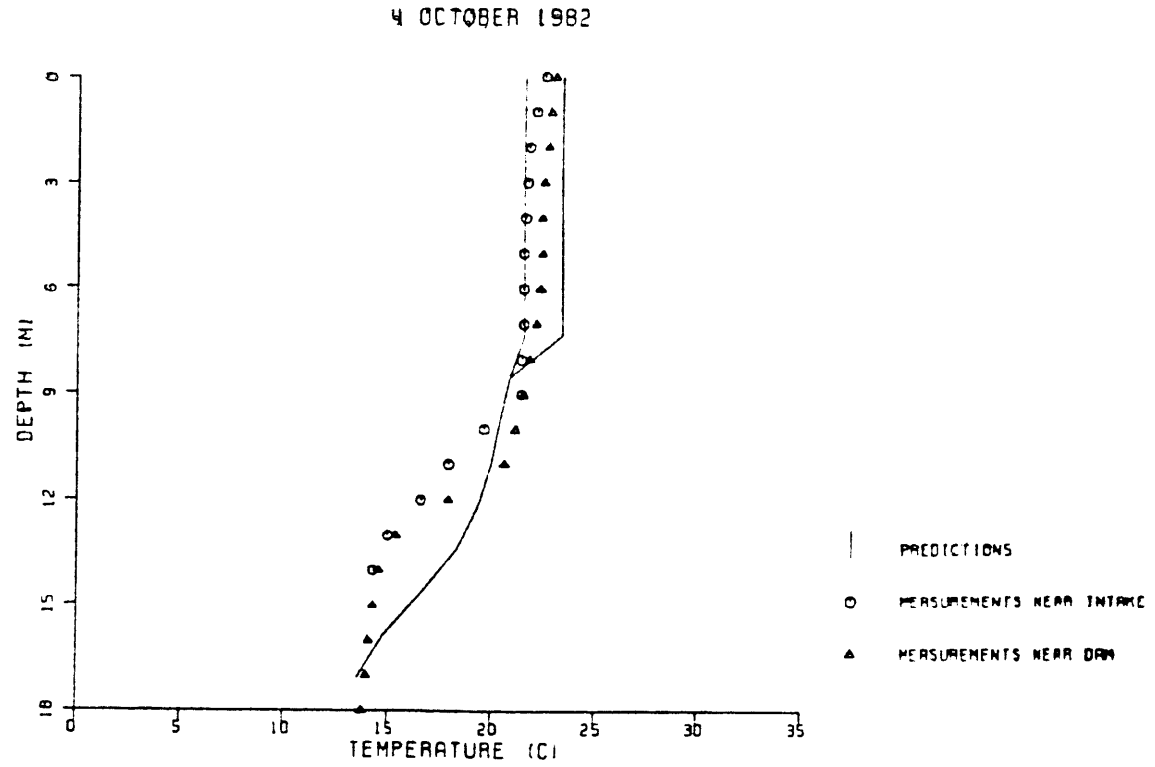

Figure 6.2c

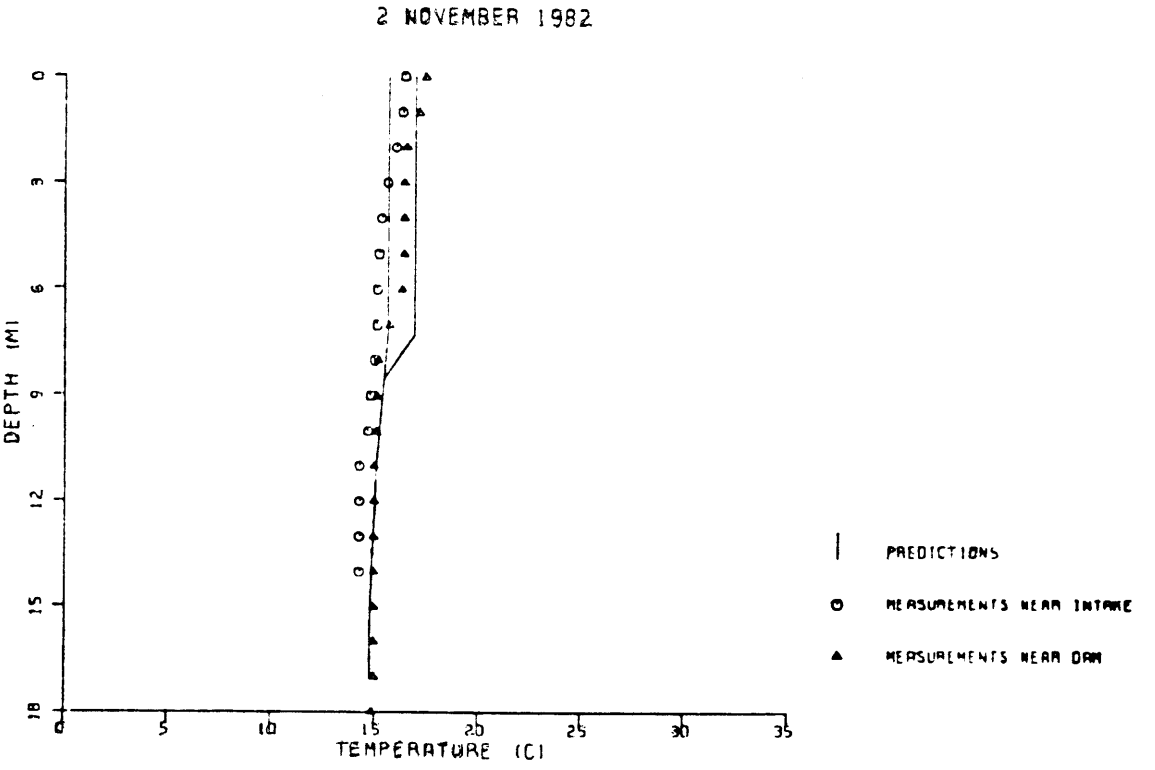

Figure 6.2d

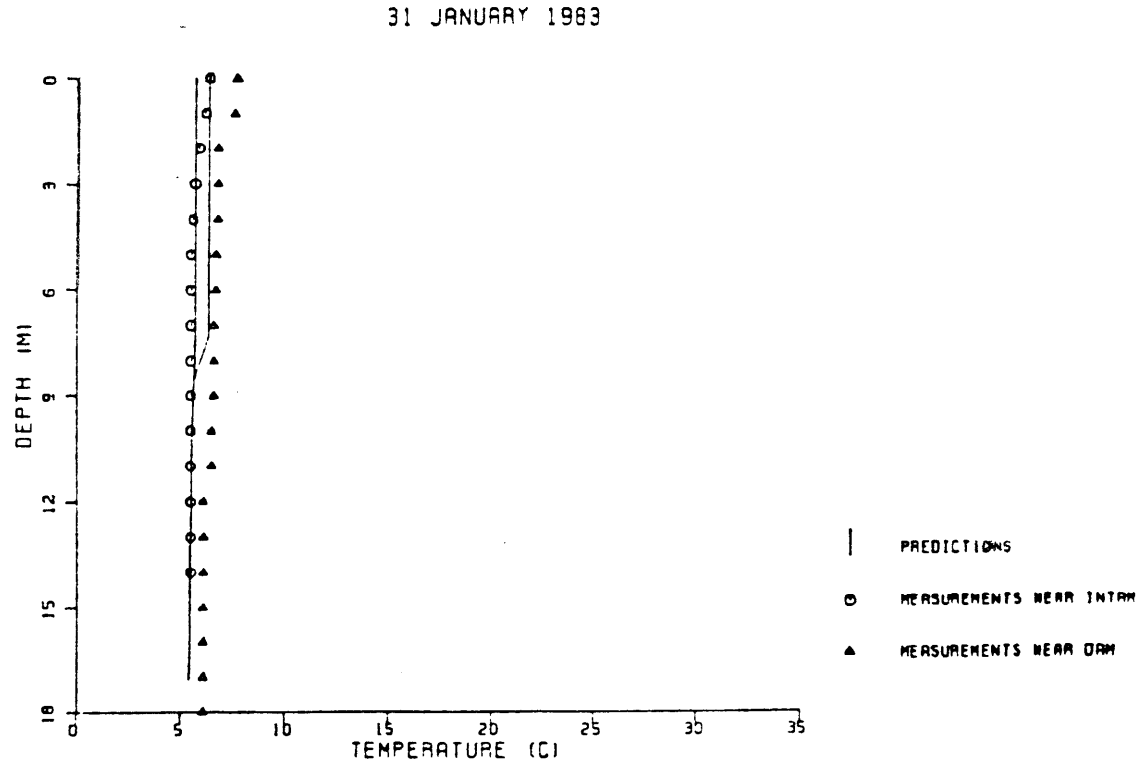

Figure 6.2e

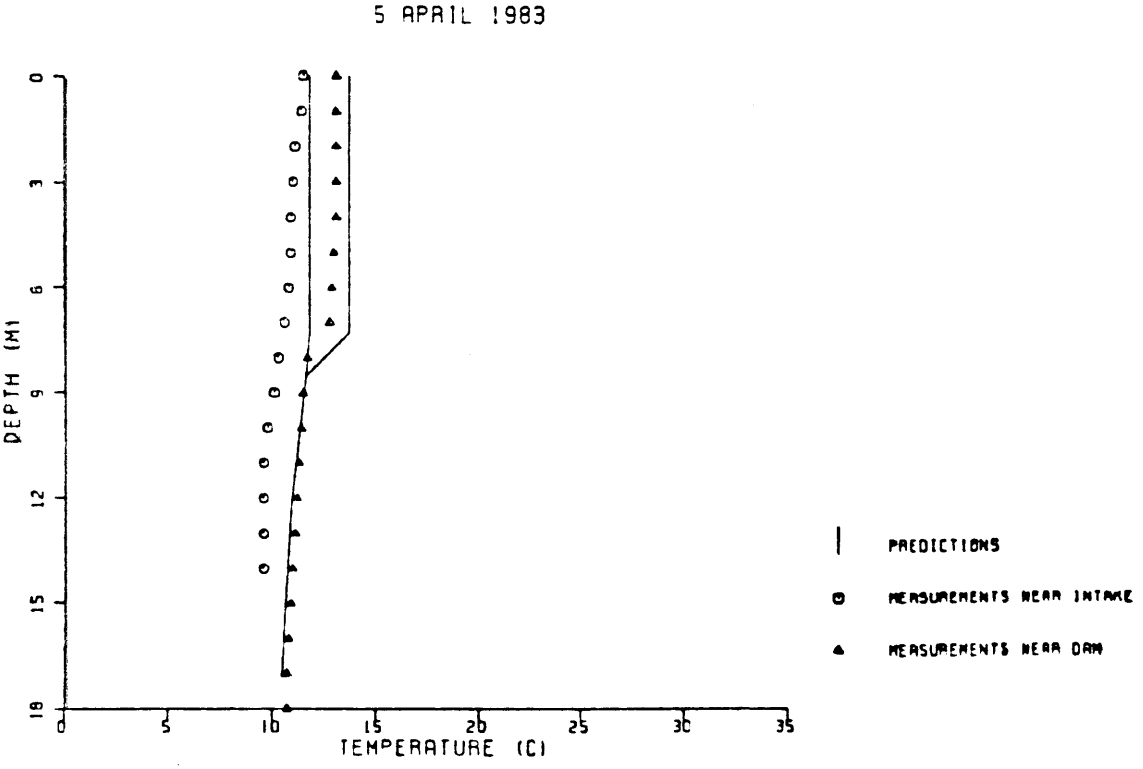

Figure 6.2f

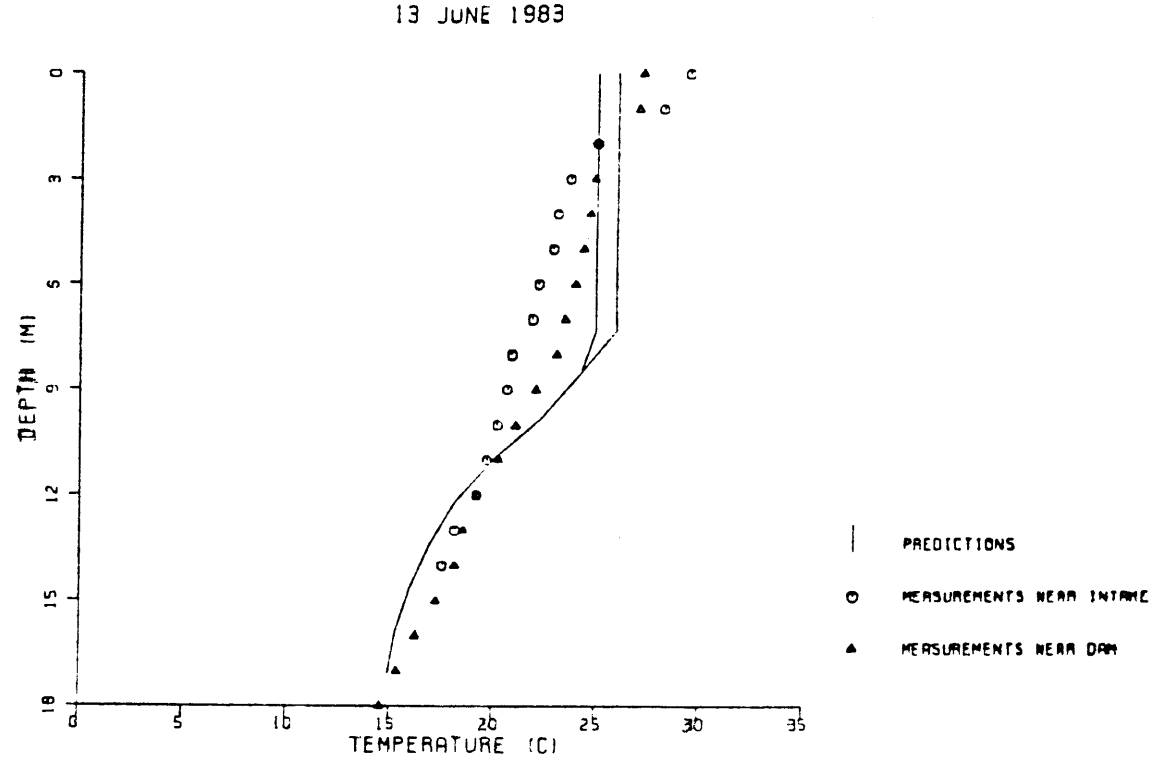

Figure 6.2g

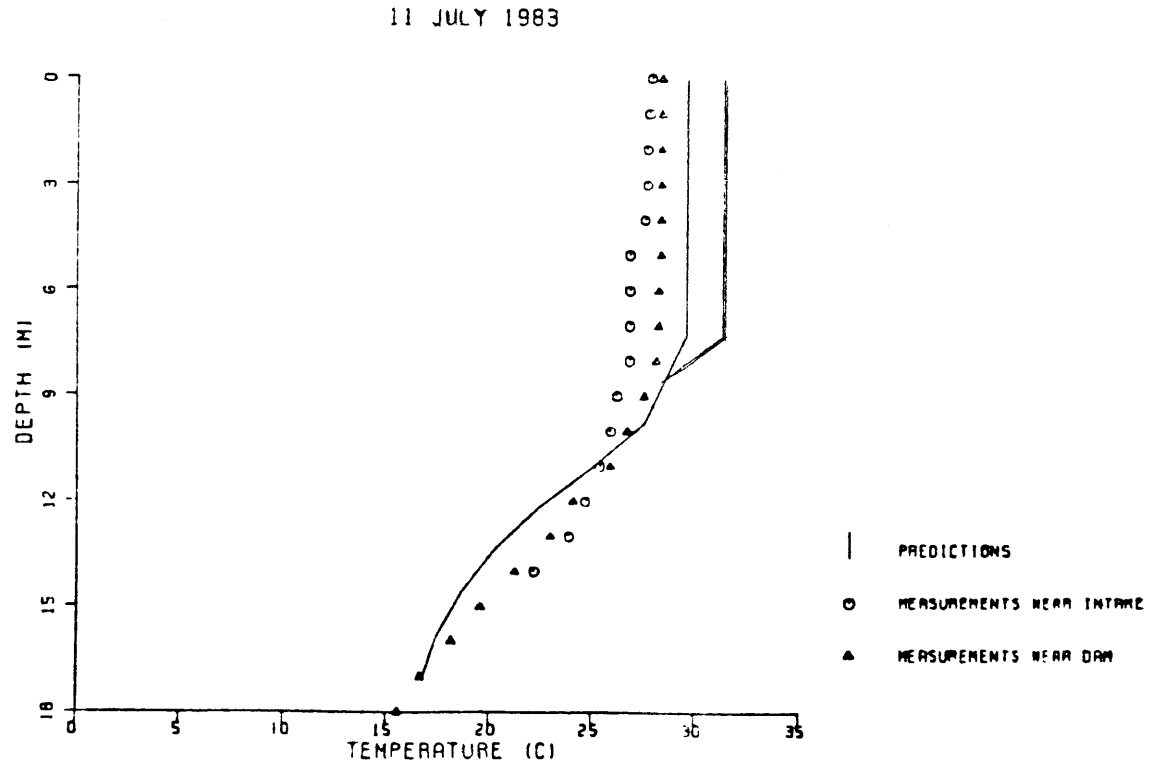

Figure 6.2h Predicted vs. Measured Vertical Temperature Profiles in Lake Anna

predicted vertical temperature profiles significantly, when compared with those shown in Wells et al. (1982). Secondly, calibration of Wells et al., although based on three years of data with primarily one-unit operation, holds up reasonably well for the fourth and fifth years with more two-unit operation.

Measured vertical temperature profiles and isotherms at five longitudinal locations (approximately equal-spaced) along the main lake are shown in Figure 6.3 for four days representing the four seasons in 1983. Slight horizontal variation is observed in the hypolimnion and some stratification occurs near the surface in winter (probably a transient daytime phenomenon caused by direct solar radiation). In general, however, the four plots collectively support the basic model assumptions of (1) a vertically well-mixed surface layer of constant thickness and horizontally-varying temperature distribution and (2) a vertically stratified subsurface layer of uniform horizontal temperature distribution.

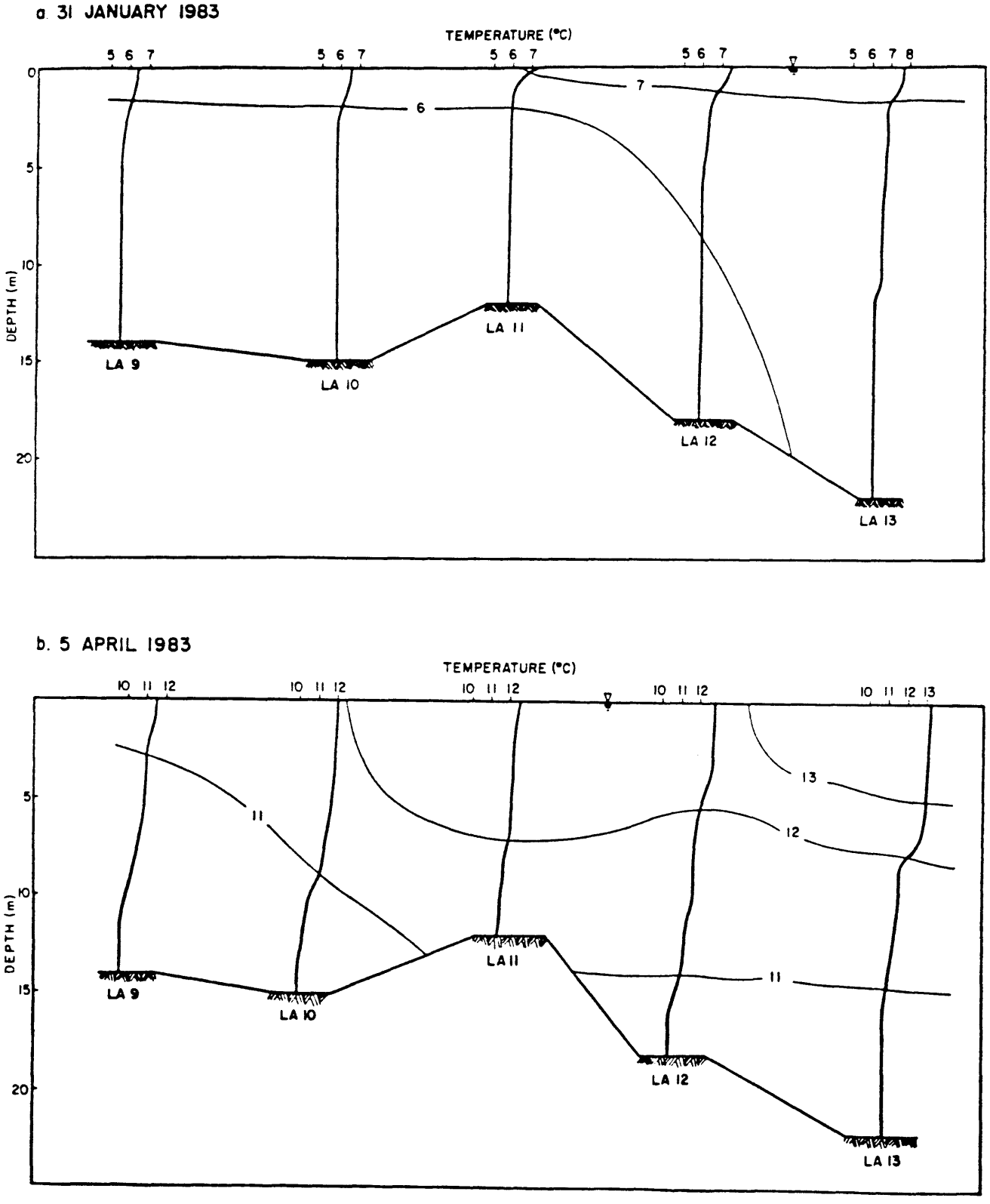

Figure 6.3 Measured Vertical Temperature Profiles and Isotherms in Lake Anna

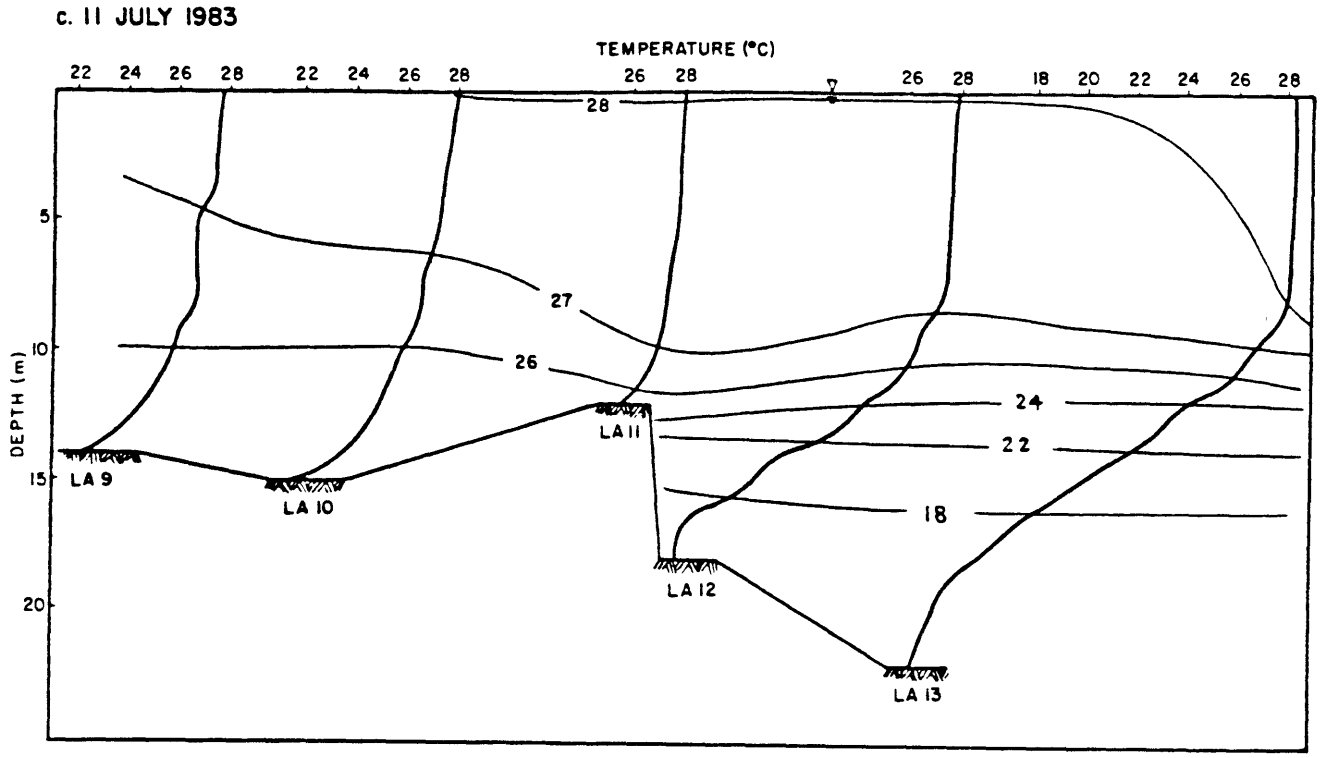

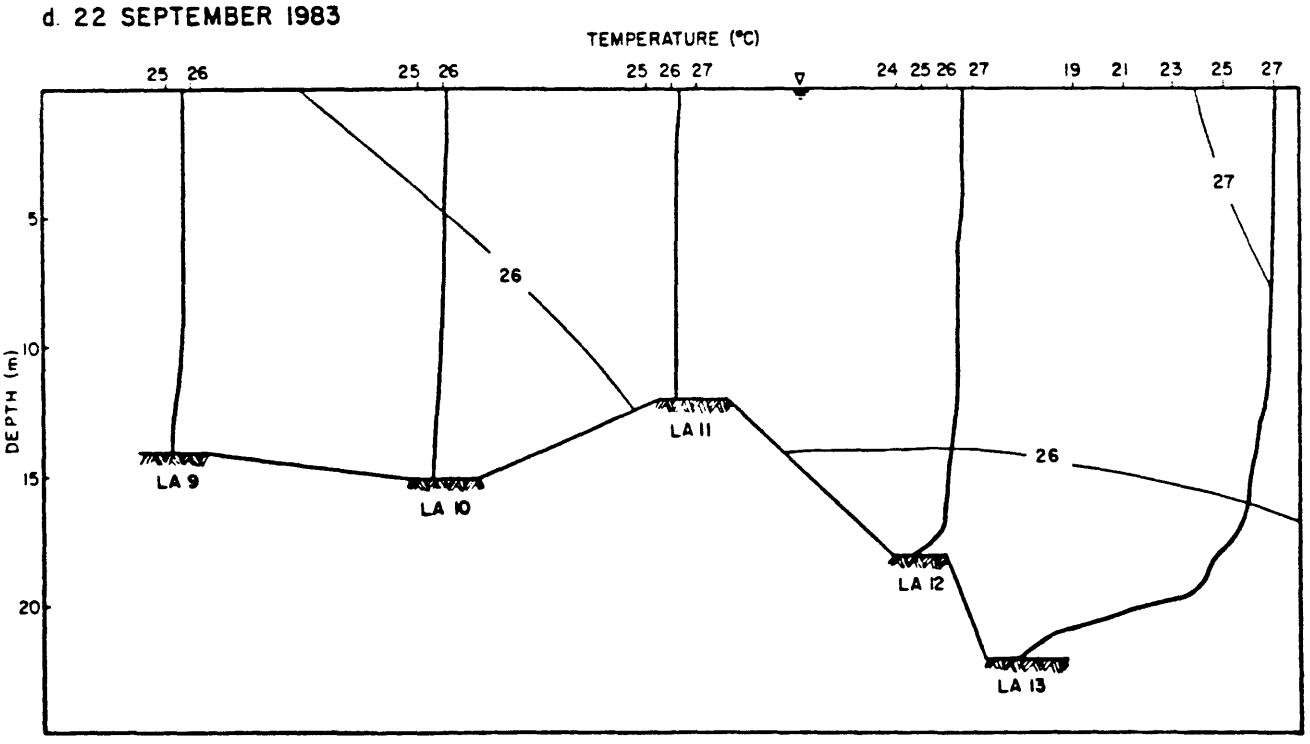

Figure 6.3 Measured Vertical Temperature Profiles and Isotherms in Lake Anna (cont'd)

7. SUMMARY

The North Anna Power Station is a two-unit power plant operated by Virginia Electric and Power Company (VEPCO). A complex cooling lake system was designed to dissipate the waste heat rejected by the plant. In order to monitor the impacts that the waste heat discharge has on the natural environment and also to assess the efficiency of the cooling lake system, a segmented mathematical model was previously developed to simulate the thermal structure of the North Anna lake system.

Since Unit 1 of North Anna Power Station came on line in summer of 1978 (follwed by Unit 2 in autumn of 1980), an extensive data collection network was established by VEPCO. Wells et al. (1982) calibrated the model using data from the first three years of operational data (1978 to 1981, primarily one-unit operation). Since then more measurements were available and an independent validation was conducted by comparing model predictions with data for the following two years (1981 to 1983, with more two-unit operation) using the same model calibrations. Continuous model input is now available for 62 months (26 July 1978 to 30 September 1983 inclusive, a total of 1893 days).

Surface temperature error analysis was made for four representative diagnostic control points over the cooling lake system. They are (1) at the discharge of Channel 1 into Pond 1 of the WHTF (designated DISCHARGE), (2) just upstream of DIKE III in the WHTF (DIKE III), (3) in the main lake near Burrus Point (BR. PT.), and (4) in the

main lake near plant intake (INTAKE). It was noticed that the model results for five years were similar to those for the first three years, as indicated by error statistics and observed periodicities of the raw errors. Moreover, error analysis indicated that the model showed a consistent performance even under "harsh" climatic and plant operation conditions, as provided by the experience of essentially two-unit operation and above-normal air temperatures during the summer of 1983. However, it was noticed that temperature rise across the plant condenser was consistently over-predicted by an average of about 0.7 °C over all five years. In addition, results of spectral analysis showed that the raw error at DIKE III was periodic at predominantly the annual frequency whereas the rest of the control points showed mild periodicities over a relatively wide range of frequencies.

Model recalibration aiming at improving the goodness-of-fit of the five years of measurement data at DISCHARGE and DIKE III was motivated by the results of the surface temperature error analysis. Two possible reasons for the transient errors characterized by annual periodicity of the raw error at DIKE III were identified, namely, errors associated with (1) the forcing function (surface heat transfer) and (2) system response of the model. Two candidates for each of the possible reasons were considered: (1a) atmospheric radiation, (1b) evaporation, (2a) spatially-averaged system response, and (2b) longitudinal system response. Among the four candidates, both (1a) and (2a) were ruled out. (1b) was considered possible since a moderate annual adjustment in the rate of evaporation over the WHTF virtually eliminated the periodicity of the raw error, but (2b) was found to be most plausible because of the strong sensitivity of the periodicity to input residence

time and because of the uncertainties in the actual residence time. The adopted approach wherein residence time was based on a fraction (75%) of the entire volume seemed more rational than that used previously and also resulted in a substantial reduction of the periodicity. However, it should be emphasized that there is still some uncertainty concerning the actual residence times which would require a dye study for further confirmation. Such a dye study would elucidate not only the effective residence time but also the residence time distribution within the WHTF which is needed if a more complete transient analysis is desired.

Steady state errors at DISCHARGE was characterized by an over-prediction of the surface temperature. Since predictions at DISCHARGE should have minimal dependence on the hydraulics of the model or on meteorological conditions, it seemed probable that the raw error was caused by uncertainty in the plant operation data. A sensitivity analysis of the raw error at DISCHARGE with respect to changes in the plant operation data was made, and it was noticed that the mean raw error was reduced substantially by a moderate (about 8%) reduction of the waste heat discharged into the WHTF. This adjustment of the plant operation data was confirmed by new data from VEPCO.

In all, two changes of the model were made as a result of recalibration: computation of residence times in the WHTF and adjustment of plant operation data. The recalibrated model was validated by comparing predictions with five years (1978 - 1983) of measurement data in terms of both surface temperatures and vertical temperature profiles. Overall mean errors for the four diagnostic control points ranged (in terms of magnitude) from a minimum of 0.01 °C

at INTAKE to a maximum of 0.16 °C at BR. PT. Standard deviations ranged from 0.80°C at INTAKE to 1.37°C at DIKE III. These values are in general less than those presented by Wells et al. (1982). In comparison with the large peak-to-peak annual variation in water surface temperature of about 23 °C, the mean errors and standard deviations are both acceptably small. Comparisons between measured and predicted vertical temperature profiles in the main lake indicated that the dynamic nature of the data both in space and time was also modelled satisfactorily.

In addition to overall averages, monthly averages of the surface temperature raw errors were also computed for each of the diagnostic control points. They ranged from a minimum of -0.69 °C for the month of September at DISCHARGE to a maximum of 0.89 °C for July at BR. PT. These monthly error statistics can be applied by VEPCO to increase the accuracy of future model predictions.

In conclusion, the recalibrated model was shown to be highly accurate in describing the thermal structure of the cooling lake system with one or two-unit operation of the power plant, and also under a wide range of meteorological conditions, thus providing confidence for its use in a predictive mode.

APPENDIX

MONTHLY-AVERAGED CALCULATIONS OF DOWNWARD LONG-WAVE RADIATION UNDER CLEAR SKY GIVEN BY EIGHT DIFFERENT EMPIRICAL FORMULAE

MONTHLY AVERAGED CALCULATIONS OF DOWNWARD LONGWAVE RADIATION UNDER CLEAR SKY GIVEN BY EIGHT DIFFERENT EMPIRICAL FORMULAE *

MONTH	AIR TEMP.	REL. HUM.	LONGWAVE RADIATION GIVEN BY VARIOUS FORMULAE 1	2	3	4	5	6	7	8	MAX	MIN	MEAN	STAND DEV
8	23.8	0.85	369.6	356.7	366.2	385.2	379.8	400.6	405.4	410.6	410.6	356.7	384.3	18.5
9	19.9	0.81	334.0	330.4	338.6	352.0	353.9	366.0	375.9	372.5	375.9	330.4	352.9	16.4
10	12.4	0.74	273.6	282.3	289.9	291.8	305.9	303.4	321.8	310.0	321.8	273.6	297.3	14.8
11	8.9	0.80	254.5	262.2	271.1	271.7	287.7	282.5	304.2	291.1	304.2	254.5	278.1	15.3
12	4.7	0.71	229.1	240.5	253.1	242.2	263.6	251.8	275.7	266.3	275.7	229.1	252.8	14.4
1	1.6	0.67	211.5	224.7	240.1	222.3	246.9	231.1	256.9	248.3	256.9	211.5	235.2	14.4
2	-2.8	0.79	194.9	203.9	225.5	203.5	228.4	211.6	240.1	231.3	240.1	194.9	217.4	15.0
3	8.8	0.74	252.3	262.4	271.9	268.4	286.0	279.0	300.2	289.1	300.2	252.3	276.1	14.5
4	12.3	0.68	269.5	282.0	289.6	286.9	303.3	298.3	316.4	306.4	316.4	269.5	294.0	14.0
5	17.5	0.72	308.1	313.8	321.2	326.9	335.6	339.9	352.8	345.2	352.8	308.1	330.4	14.6
6	20.6	0.82	338.6	334.3	342.5	356.5	357.6	370.7	380.0	377.5	380.0	334.3	357.2	16.6
7	23.1	0.88	364.9	351.6	360.7	379.2	374.5	394.3	400.2	408.1	408.1	351.6	379.2	18.8
8	22.8	0.89	364.3	349.7	358.8	379.5	374.2	394.6	400.9	406.4	406.4	349.7	378.5	19.3
9	19.4	0.92	336.8	326.6	334.5	353.7	353.1	367.8	378.8	377.8	378.8	326.6	353.6	18.7
10	12.9	0.86	284.5	285.9	293.8	302.4	312.3	314.5	332.5	322.3	332.5	284.5	306.0	16.2
11	10.5	0.81	266.2	271.7	280.3	283.6	297.4	294.9	315.0	303.3	315.0	266.2	289.1	15.5
12	4.7	0.75	229.6	240.0	252.2	243.6	264.4	253.3	277.7	266.2	277.7	229.6	253.4	14.7
1	2.0	0.70	213.9	226.3	240.9	225.7	249.5	234.7	260.6	250.4	260.6	213.9	237.8	14.5
2	0.3	0.61	203.9	218.3	235.5	212.9	239.3	221.4	247.5	240.9	247.5	203.9	227.5	14.4
3	6.4	0.67	236.0	249.4	260.8	249.9	271.2	259.9	282.4	272.7	282.4	236.0	260.3	14.0
4	13.3	0.64	272.5	287.4	294.7	290.8	307.5	302.4	319.5	308.6	319.5	272.5	297.9	13.7
5	19.4	0.65	316.6	326.7	334.6	336.0	345.2	349.3	359.7	352.5	359.7	316.6	340.1	13.4
6	21.6	0.74	342.4	341.6	350.3	360.3	362.4	374.6	382.3	380.3	382.3	341.6	361.8	15.2
7	24.8	0.80	375.0	364.4	374.3	390.8	385.5	406.4	409.6	414.9	414.9	364.4	390.1	17.4
8	24.6	0.76	369.3	362.4	372.3	386.0	382.6	401.4	405.0	407.8	407.8	362.4	385.8	16.2
9	21.6	0.38	306.6	341.7	350.5	326.9	346.9	339.9	346.8	340.7	350.5	306.6	337.5	13.4
10	13.6	0.69	279.8	290.2	298.0	298.0	312.0	309.8	326.5	316.2	326.5	279.8	303.8	14.1
11	7.4	0.63	237.8	254.3	264.4	252.7	274.9	262.8	284.7	274.2	284.7	237.8	263.2	14.0
12	2.8	0.66	217.1	231.3	246.2	228.9	253.0	238.0	262.8	253.6	262.8	217.1	241.4	14.3
1	-0.9	0.63	198.6	212.6	231.6	207.2	234.0	215.5	242.3	235.1	242.3	198.6	222.1	14.7
2	4.6	0.64	226.4	240.1	253.3	238.6	261.5	248.1	271.6	263.4	271.6	226.4	250.4	14.0
3	6.1	0.61	231.3	247.7	258.9	244.6	267.9	254.4	277.0	268.1	277.0	231.3	256.2	13.9
4	14.8	0.54	276.3	296.9	304.5	294.2	312.9	305.9	320.9	312.2	320.9	276.3	303.0	12.9
5	17.0	0.42	279.5	310.8	318.4	297.9	320.3	309.7	322.1	315.1	322.1	279.5	309.2	13.3
6	24.2	0.52	341.8	359.7	369.4	361.8	370.7	376.2	380.1	375.6	380.1	341.8	366.9	11.5
7	25.1	0.76	374.2	366.8	376.9	390.6	386.4	406.1	408.8	412.8	412.8	366.8	390.3	16.2
8	22.0	0.81	350.6	343.8	352.5	367.9	366.7	382.5	389.9	390.0	390.0	343.8	368.0	17.0
9	20.3	0.71	329.4	332.8	341.1	348.2	353.3	362.1	371.4	366.3	371.4	329.4	350.6	14.5
10	12.0	0.75	271.6	280.3	288.1	289.6	303.9	301.1	319.7	308.3	319.7	271.6	295.3	14.8

11	8.2	0.66	245.1	259.2	269.0	260.5	280.7	270.8	292.1	281.7	292.1	245.1	269.9	14.0
12	1.8	0.76	215.0	225.3	240.3	227.2	249.9	236.3	262.5	251.6	262.5	215.0	238.5	14.7
1	-1.7	0.64	196.3	209.4	229.7	203.8	230.6	211.9	238.9	233.1	238.9	196.3	219.2	14.7
2	3.0	0.79	221.4	230.9	244.7	234.8	256.2	244.2	269.9	257.9	269.9	221.4	245.0	14.9
3	7.0	0.69	239.1	252.6	263.1	254.1	274.8	264.2	286.6	275.6	286.6	239.1	263.8	14.2
4	11.6	0.55	257.8	277.9	286.2	273.7	294.9	284.6	302.6	294.5	302.6	257.8	284.0	13.3
5	19.7	0.70	323.5	328.7	336.6	342.1	348.7	355.7	365.8	360.6	365.8	323.5	345.2	14.2
6	21.0	0.81	341.5	337.0	345.4	359.5	360.2	373.8	382.6	380.2	382.6	337.0	360.0	16.6
7	23.3	0.89	368.6	353.0	362.2	383.6	377.4	398.9	404.5	411.0	411.0	353.0	382.4	19.6
8	22.9	0.83	360.3	350.4	359.6	376.7	373.4	391.7	397.7	400.3	400.3	350.4	376.3	17.6
9	18.4	0.89	326.3	320.1	327.7	344.3	346.1	358.0	370.1	365.8	370.1	320.1	344.8	17.7
10	13.0	0.84	284.6	286.6	294.5	302.4	312.6	314.5	332.3	322.5	332.3	284.6	306.3	16.0
11	9.2	0.83	259.6	264.5	273.9	276.3	290.8	287.3	308.6	296.8	308.6	259.6	282.2	15.6
12	6.0	0.88	244.5	248.2	260.5	259.5	275.5	269.9	293.4	281.8	293.4	244.5	266.6	15.6
1	2.3	0.75	217.2	227.6	242.0	229.7	252.1	238.9	264.8	253.8	264.8	217.2	240.8	14.7
2	3.0	0.75	220.5	231.4	245.2	233.5	255.7	242.8	268.3	257.0	268.3	220.5	244.3	14.7
3	8.4	0.73	248.4	259.5	268.9	264.4	282.9	274.9	296.5	285.3	296.5	248.4	272.6	14.5
4	11.9	0.71	268.3	279.9	288.1	285.8	301.9	297.2	315.6	304.9	315.6	268.3	292.7	14.2
5	17.5	0.68	305.4	314.3	321.8	324.1	334.4	337.0	349.6	342.1	349.6	305.4	328.6	13.9
6	22.8	0.73	350.9	349.7	358.9	368.9	369.7	383.6	389.7	388.3	389.7	349.7	370.0	15.0
7	25.7	0.67	370.0	370.5	380.9	387.9	386.9	403.3	405.2	406.1	406.1	370.0	388.9	13.8
8	25.5	0.67	368.6	369.1	379.4	386.6	385.8	402.0	404.1	404.6	404.6	368.6	387.5	13.9
9	21.0	0.66	331.1	338.3	347.1	350.2	356.4	364.1	372.2	366.7	372.2	331.1	353.3	13.4

* TEMPERATURE IN DEGREES CELCIUS
RADIATION IN WATTS PER SQUARE METER
DATA START AUGUST 1978
FORMULAE USED TO CALCULATE LONG-WAVE RADIATION:

BRUNT(1932) 1
SWINBANK(1963) 2
IDSO-JACKSON(1969) 3
BRUTSAERT 1(1975) 4
SATTERLUND(1979) 5
BRUTSAERT 2(1981) 6
IDSO 1(1981) 7
IDSO 2(1981) 8

LIST OF REFERENCES

Adams, E.E., The Transient Response of Cooling Ponds, Water Resources Research, Vol. 18, No. 5, pp. 1469-1478, Oct., 1982.

Adams, E.E. and Koussis, A.D., Transient Analysis for Shallow Cooling Ponds, J. of the Energy Division, ASCE, Vol. 106, No. EY2, pp. 141-153, Oct., 1980.

Adams, E.E. and Wells, S., Field Measurements on Side Arms of Lake Anna, VA., J. of Hydraulic Engineering, ASCE, Vol. 110, No. HY6, June, 1984.

Bolz, H.M., Die Abhängigkeit der infraroten Gegenstrahlung von der Bewölkung, Z. Meteorol. 3, pp. 201-203, 1949.

Brocard, D., Jirka, G. and Harleman, D., A Model for the Convective Circulatio in Side Arms of Cooling Lakes, T.R. No. 223, R.M. Parsons Laboratory, Department of Civil Enginering, M.I.T., 1977.

Brutsaert, W., Evaporation into the Atmosphere: Theory, History and Applications, Reidel Publishing Co., Dordrecht, Holland, 1982.

Grenander, U. and Rosenblatt, M., Statistical Analysis of Stationary Time Series, Wiley & Sons, Inc., New York, 1957.

Hatfield, J.L., Reginato, R.J. and Idso, S.B., Comparison of Long-Wave Radiation Calculation Methods Over the United States, Water Resources Research, Vol. 19, No. 1, pp. 285-288, Feb., 1983.

Idso, S.B. and Jackson, R.D., Thermal Radiation from the Atmopshere, J. of Geophysical Research, Vol. 74, No. 23, Oct., 1969.

Jirka, G.H., Abraham, G. and Harleman, D.R.F., An Assessment of Techniques for Hydrothermal Predictions, T.R. No. 203, R.M. Parsons Laboratory, Department of Civil Engineering, M.I.T., 1975.

Jirka, G.H., Adams, E.E., and Stolzenbach, K.D., Buoyant Surface Jets, J. of Hydraulics Div., ASCE, Vol. 107, No. HY11, Nov., 1981.

Jirka, G.H., Brocard, D., Octavio, K., Watanabe, M. and Harleman, D., Analysis of Cooling Effectiveness and Transient Long-Term Simulations of a Cooling Lake with Application to the North Anna Power Station, T.R. No. 232, R.M. Parsons Laboratory, Department of Civil Engineering, M.I.T., 1977.

Kimball, Idso and Aase, A Model of Thermal Radiation from Partly Cloudy and Overcast Skies, Water Resources Research, Vol. 18, No. 4, pp. 931-936, 1982.

Local Climatological Data, Richmond, VA, publication of the NOAA, U.S. Department of Commerce, by the National Climatic Center, Asheville, North Carolina.

Octavio, K., Jirka, G. and Harleman, D., Vertical Heat Transport Mechanisms in Lakes and Reservoirs, T.R. No. 227, R.M. Parsons Laboratory, Department of Civil Engineering, M.I.T., 1977.

Ryan, P. and Harleman, D., An Analytical and Experimental Study of Transient Cooling Pond Behavior, T.R. No. 161, R.M. Parsons Laboratory, Department of Civil Engineering, M.I.T., 1973.

Salhotra, A., Adams, E. and Harleman, D., Evaporation and Stratification Studies for the Dead Sea, Progress Report No. 2, R.M. Parsons Laboratory, Department of Civil Engineering, M.I.T., 1983.

Sellers, W., Physical Climatology, U. of Chicago Press, Chicago and London, 1965.

Stolzenbach, K. and Harleman, D., An Analytical and Experimental Investigation of Surface Discharges of Heated Water, T.R. No. 135, R.M. Parsons Laboratory, Department of Civil Engineering, M.I.T., 1971.

Swinbank, W., Longwave Radiation from Clear Skies, Quarterly J. of the Royal Meteorological Society of London, Vol. 89, July 1963.

Thackston, E., Effect of Geophysical Location on Performance of Recirculating Cooling Ponds, EPA Report No. 660/2-74-085, Nov., 1974.

Watanabe, M., Harleman, D. and Connor, J., Finite Element Model for Transient Two-Layer Cooling Pond Behavior, T.R. No. 202, R.M. Parsons Laboratory, Department of Civil Engineering, M.I.T., 1975.

Wells, S., Adams, E. and Harleman, D., Calibration and Verification of the Cooling Lake Model for North Anna Power Station, T.R. No. 272, R.M. Parsons Laboratory, Department of Civil Engineering, M.I.T., 1982.

Wunderlich, W., Heat and Mass Transfer Between a Water Surface and the Atmosphere, Lab. Report No. 14, T.V.A. Engineering Laboratory, Norris, Tennessee.

LIST OF FIGURES

LIST OF TABLES